Quantum Two Dimensional Materials Explored via Advanced Electron Microscopy

by

Suk Hyun Sung

A dissertation submitted in partial fulfillment
of the requirements for the degree of
Doctor of Philosophy
(Materials Science and Engineering)
in the University of Michigan
2023

Doctoral Committee:

Assistant Professor Robert Hovden, Chair
Associate Professor John T. Heron
Professor Kai Sun
Associate Professor Liuyan Zhao

Suk Hyun Sung

sukhsung@umich.edu

ORCID iD: 0000-0002-7491-1988

To my family and friends.

ACKNOWLEDGEMENTS

First and foremost, I would like to thank my advisor, Robert Hovden. I could not have asked for a better advisor. His scientific intuition and knowledge has always been inspiring. He introduced me to the wonderful world of 2D quantum materials and gave me many opportunities to work with the leaders of the field. He always made sure I remain productive while I secretly invest time in (often foolish) side projects. I will always miss endless discussions we had—be they about Fourier transform, be they about quantum mechanics, be they about graphics design.

Through out my Ph. D, I was very fortunate to work with many great collaborators: Ismail El Baggari, Rebecca Engelke, Xiaoyu Gu, John T. Heron, Philip Kim, Xiangpeng Luo, Andrew J. Mannix, Peter Meisenheimer, Steve Novakov, Jiwoong Park, Kai Sun, Zeliang Sun, Hongchao Xie, Andrew Ye, Hyobin Yoo and Liuyan Zhao. I also have to thank staffs at University of Michigan Center for Materials Characterization—Bobby Kerns, Tao Ma, Allen Hunter, Haiping Sun, and Kai Sun—for maintaining the electron microscopes at their peak performances and all the training I received from them.

Of course, I need to thank Hovden group members for making this journey much more interesting—Nishkarsh Agarwal, Maya Gates, Jiseok Gim, Yin Min Goh, Yu-Ho Lin, Jason Manassa, Jacob Pietryga, EmJ Rennich, Jonathan Schwartz, Noah Schnitzer and Reed Yalisove. Special thanks to Noah Schnitzer for preparing numerous samples and for pursing silly side projects together and Jonathan Schwartz for all the fun conversations and making annual microscopy conferences more of a fun vacation.

Thanks to Lena F. Kourkoutis and David J. Baek, along with all other KEM group members, for introducing me to electron microscopy and scientific research. I loved it so much back then, and I am still doing it.

Lastly and most importantly, thanks to my parents and my sister An Na who have supported me entire my life.

PREFACE

New materials are needed to unlock next generation computational capabilities that will fuel solutions spanning all areas of science—from medicine to clean-energy. Harnessing exotic quantum materials is among the most promising areas for progress.

The field of two dimensional (2D) materials has exploded since the discovery that graphene—a single layer of carbon atoms—can be exfoliated to its existence. Since then, a plethora of 2D materials has been exfoliated or synthesized, each with an exciting properties and opportunities.

In this thesis, we will explore the exotic quantum behaviors of 2D materials in using various advanced electron microscopy techniques.

Suk Hyun Sung was born in Seoul, Republic of Korea to Ki Tae Sung and Eun Young Lee. He was raised in the Korea until he crossed the Pacific to attend boarding schools in the United States at the age of 13. He received Bachelor's degree in Engineering Physics at Cornell University. At Cornell, he joined Prof. Lena Fitting Kourkoutis's group where he was first introduced and became passionate to scientific research and electron microscopy. He continued his passion and entered Ph. D program at the University of Michigan under guidance of Prof. Robert Hovden. In Hovden lab, Suk Hyun was able to study materials science and electron microscopy in theoretical, experimental and computational aspects. Suk Hyun Sung completed his Ph. D in summer of 2023.

CONTENTS

Contents

DEDICATIONS . . . . . **ii**

ACKNOWLEDGEMENTS . . . . . **iii**

PREFACE . . . . . **iv**

LIST OF FIGURES . . . . . **vii**

LIST OF APPENDICIES . . . . . **ix**

ABSTRACT . . . . . **x**

CHAPTER

I. Introduction to Electron Diffraction **1**
- Electron Diffraction 2
- References 5

II. Reciprocal Structures of 2D Materials **7**
- Background to Diffraction of 2D Materials 8
- Bilayer Graphene 10
- Beam Energy & the Ewald Sphere 12
- Twisted, Moiré Layers 13

2D Transition Metal Dichalcogenides . . . 14
Multilayer 2D Materials . . . 17
Summary & Conclusion . . . 19
References . . . 19

III. Torsional Periodic Lattice Distortions and Diffraction of Twisted 2D Materials 23
Periodic Restructuring in Twisted Bilayer Graphene . . . 24
Diffraction of Moiré Materials . . . 27
Critical Twist Angles and the Low-twist Regime . . . 28
Sharp PLD Boundaries at Extreme Low-Twist Angles . . . 30
Torsional PLDs Across Many Twisted 2D Materials . . . 34
Discussions . . . 36
References . . . 36

IV. Two-dimensional Charge Order Stabilized in Clean Polytype Heterostructures 40
Introduction . . . 40
Twinned Commensurate Charge Density Waves . . . 42
Clean Polytype Heterostructures . . . 43
Isolation of 2D Charge Density Waves . . . 45
Optical and Electrical Characteristics of tC-CDW . . . 47
Discussion . . . 47
References . . . 48

V. Enhancement and Melting of Charge Density Waves with 2D Endotaxy . . . 53
Introduction . . . 53
The Ordered Incommensurate Charge Density Wave . . . 55
Endotaxial Polytype Heterostructure of TaS_2 . . . 56
Hexatic Melting of IC-CDW . . . 58
The CDW Phase Diagram for Octahedral TaS_2 . . . 59
Conclusion . . . 61
References . . . 61

VI. Conclusion . . . 66
Summary . . . 66
Future Works . . . 67

APPENDICIES . . . 68

LIST OF FIGURES

I.1 Overview of Transmission Electron Microscopy and Electron Diffraction . . . 2
I.2 Ewald's sphere and specimen tilt . . . 4

II.1 3D reciprocal structure of Single and Bilayer Graphene . . . 9
II.2 Diffraction tilt-patterns of BLG . . . 11
II.3 Twisted Bilayer Graphene . . . 13
II.4 3D reciprocal structure of 2D transition metal dichalcogenides and polytypes. 15
II.5 K-structure of monolayer 2H-MoS_2 . . . 16
II.6 Diffraction tilt-patterns of multilayer Bernal and rhombohedral graphene . . . 18

III.1 Periodic Restructuring of Twisted Bilayer Graphene (TBG) . . . 24
III.2 Relative Phases of torsional PLD . . . 26
III.3 Transversity of PLD . . . 27
III.4 Quantification of Torsional PLD Amplitude A_1 . . . 28
III.5 Torsional Periodic Lattice Distortion (PLD) Model . . . 29
III.6 Energy and Amplitude of PLDs in Twisted Bilayer Graphene (TBG) . . . 30
III.7 PLDs as a Fourier Series in 2D Moiré Materials . . . 31
III.8 Contribution of PLD Harmonics across Twist Angles . . . 32
III.9 Exponential Decay of PLD Harmonics . . . 33
III.10 Universal Torsional PLD Relaxation of Twisted 2D Materials . . . 34
III.11 Periodic relaxations in lattice mismatched twisted bilayer systems . . . 35

IV.1 Unit cells of previously synthesized TaS_2 polytypes . . . 41
IV.2 Twinned, commensurate CDW at room temperature in ultrathin TaS_2 . . . 42
IV.3 Polytype isolation forms 2D CDW layers . . . 44
IV.4 Phenomenological model illustrates formation of commensurate CDWs with out-of-plane twin degeneracy . . . 46
IV.5 Electronic transport of tC-CDW phase transition and reversibility . . . 48

V.1 Long-range Ordered Incommensurace Charge Density Waves . . . 54
V.2 Endotaxial Polytype Heterostructure of TaS_2 . . . 57

V.3 Hexatic Melting of IC-CDWS 58
V.4 Phase Diagram of Octahedrally Coordinated TaS_2 60

VI.1 Evolution of Bragg Rods with Thickness 73
VI.2 3D Reciprocal Structure of Multilayer Graphene 74
VI.3 3D Reciprocal Structure of mono- and bi-layer TMDs 75
VI.4 Simulated diffraction tilt-pattern of multilayer graphene 76
VI.5 Simulated diffraction tilt-patterns of single and bilayer MoS_2 and polytypes thereof 77
VI.6 Simulated diffraction tilt-patterns of various MoS_2, WSe_2, TaS_2 and polytypes thereof 78

LIST OF APPENDICIES

A Appendix for Chapter II 69
B Appendix for Chapter III 79
C Appendix for Chapter IV 86
D On Infinite Series of Bessel functions of the First Kind 88

ABSTRACT

Two dimensional (2D) materials often exhibit unexpected, emergent physical properties—often due to their confined dimensionalities and unique symmetry breaking. However, 2D materials still exist in the 3D world. They often consist of multiple atomic layers, not perfectly flat, and interact with environment above and below. Therefore, understanding of full 3D structure of 2D materials is paramount to harnessing the true potential of 2D materials. In this dissertation, we will discuss advanced electron microscopy techniques to probe various 2D materials and heterostructures thereof. We engineer periodically modulated out-of-plane interaction by forming moiré patterns of 2D materials. Furthermore, this work demonstrates 2D endotaxy of tantalum disulfides (TaS_2) and endotaxial polytype heterostructure as a new platform to stabilize latent CDW states.

Chapter I and II motivates electron microscopy and electron diffraction for probing atomic structure of 2D materials in real spaces. It also discusses rich information hidden in 3D reciprocal structures of 2D materials and introduces 3D electron diffraction as a platform for probing 3D reciprocal structures. We use 3D electron diffraction to measure and identify various out-of-plane information of multiple 2D materials. We measure inter- and intra-layer spacings in 2-layer graphene, 1-layer molybdenum disulfide (MoS_2), identify exact stacking sequence of 6 and 12-layer graphenes and measure small lattice distortions.

In Chapter III, periodic lattice distortions (PLDs) in twisted 2D materials are discussed. Moiré pattern emerges when two layers of 2D materials are stacked with a mismatch in crystal orientation. This results in periodically modulated out-of-plane interactions which periodically distorts constituent 2D crystals. Here, we introduce torsional PLD to describe the periodic restructuring in twisted 2D materials and extract a single coefficient that describes the full restructuring scheme by matching experimental data to computationally simulated data. With torsional PLD, we describe positions of >10,000 atoms in 1.1° twisted bilayer graphene using a single order parameter. Lastly, we showcase various twisted 2D materials that exhibits torsional PLD.

In Chapter IV and V, we discuss charge density waves (CDWs) in 2D materials. We introduce the novel method of endotaxial engineering that manipulates CDW phases. Specifically, in Chapter IV, we show endotaxial polytype engineering stabilizes low temperature long-range ordered CDW phase at room temperatures and enables out-of-plane twinning in octahedrally coordinated TaS_2. We provide a theoretical model explaining twinning of CDWs as well as a computational validation. In Chapter V, we investigate the nature of incommensurate CDWs in TaS_2. We show endotaxial polytype engineering crystallizes IC-CDWs into more long-range ordered and amplitude enhanced version. We also reveal the hexatic nature of the IC-CDWs in TaS_2 by doing controlled heating experiments.

Lastly, Chapter VI summarizes result and concludes this thesis.

Chapter I

Introduction to Electron Diffraction

"For his discovery of the diffraction of X-rays by crystals": Max von Laue received the Nobel Prize in 1914 [1]. This was one of the earliest confirmation of atomic theory. Since then, diffraction has always been at the forefront of structural characterization and discoveries. In 1915, William Henry Bragg and William Lawrence Bragg was awarded for setting the foundation for X-ray crystallography [2]. The key experimental evidence which solved the structure of DNA was an X-ray diffraction pattern [3].

To resolve smaller features scientists turned to electrons. The wave behavior of matter was first hypothesized by de Broglie in 1924 [4], and three years later validated by Thomson, Davisson, Germer with the experimental demonstration of electron diffraction [5, 6]. In 1986, Ernst Ruska received Nobel Prize "for his fundamental work in electron optics, and for the design of the first electron microscope" [7]. More recently, Dan Shechtman was awarded Nobel Prize in chemistry for discovery of quasicrystal [8].

With invention of aberration corrected electron microscopes [9], the popularity of real space characterizations like high-angle annular dark-field scanning transmission electron microscopy (HAADF-STEM) is growing rapidly. Achieving atomic resolution is not only possible but becoming a commonplace. However, real space characterization have its own limitations and traditional diffraction techniques, such as selected area electron diffraction (SAED), still remains powerful and sometimes is the only option. The following section provides a light introduction to electron diffraction.

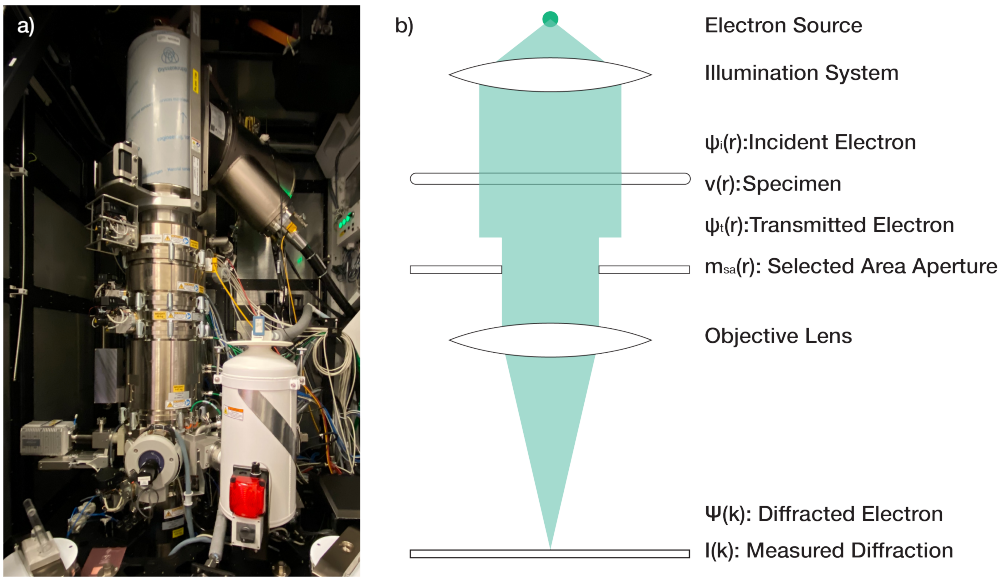

Figure I.1: Overview of Transmission Electron Microscopy and Electron Diffraction. a) Thermofisher Spectra 300 Probe Corrected S/TEM. b) Schematic ray diagram for selected area electron diffraction

Electron Diffraction

$$\lambda = \frac{h}{p} \tag{I.1}$$

Matters are also waves and electrons diffract. de Broglie's wave-particle duality (Eq. I.1) is a fundamental concept of quantum mechanics and the tenet electron microscopy is built upon. The equation relates the wavelength of matter (λ) to Planck's constant (h) and the momentum (p). In transmission electron microscopy (TEM), electrons are accelerated to high momentum to achieve small wavelength—critical for resolving small atomic features. At electron energy (E) of 100 keV, a typical operating energy for TEM, electrons have relativistic wavelength of 3.7 pm. It is worth nothing that the equation for wavelength of matter at relativistic speed is slightly modified version of de Broglie's original hypothesis which results in a wavelength about 10% shorter:

$$\lambda = \frac{hc}{\sqrt{E(2m_0c^2 + E)}} \tag{I.2}$$

where m_0c^2 is the electron rest energy.

TEM (Fig. I.1a) is a very complex instruments. A typical TEM needs to generate and accelerate electrons to ∼100 keV, maintain high-vacuum through-out the column, have electromagnetic lens to sculpt the electron waves, and have detectors to collect scientific

data. Figure I.1b shows highly abstracted schema for selected area electron diffraction.

In conventional TEM, the incident swift electrons ($\psi_i(\mathbf{r})$) forms a parallel wave propagating along the optic axis ($\hat{\mathbf{z}}$): $\psi_i(\mathbf{r}) = \exp[2\pi i z/\lambda]$. If we set the origin at the specimen height, the expression simplifies to $\psi_i = 1$.

If the specimen is weak phase object (i.e., thin specimen with light atoms), the transmitted wave gains phase proportional to projected atomic potential ($v_z(\mathbf{r})$), and interaction parameter ($\sigma_e = 2\pi me\lambda/h^2$, m: relativistic mass, e: electron charge): $\psi_t(\mathbf{r}) = \exp[i\sigma_e v_z(\mathbf{r})]$. Notably, when either σ_e or $v_z(\mathbf{r})$ is small, we can Taylor expand the wavefunction:

$$\psi_t(\mathbf{r}) \approx \exp[i\sigma_e v_z(\mathbf{r})] \approx 1 + i\sigma_e v_z(\mathbf{r}) + ... \tag{I.3}$$

Experimentally, the incident wave have a finite spatial extent often chosen deliberately with selected area (SA) aperture. We may simply multiply a binary circular mask function ($m_{SA}(\mathbf{r})$) with cutoff radius r_c:

$$\psi_{t,SA}(\mathbf{r}) = \psi_t(\mathbf{r}) m_{SA}(\mathbf{r}) \tag{I.4}$$

The transmitted wave is then focused to reciprocal space using post-specimen lens where final diffraction pattern ($I(\mathbf{k})$) is collected. Mathematically, this is equivalent measuring the squared modulus of Fourier transform of the wave:

$$\begin{aligned} I(\mathbf{k}) &= |\Psi_t(\mathbf{k})|^2 = |\mathcal{F}[\psi_t(\mathbf{r})]|^2 \\ &\approx |\mathcal{F}[1 + i\sigma_e v_z(x,y) + ...]|^2 \\ &\approx |(\delta(\mathbf{k}) + i\sigma_e \mathcal{F}[v_z(x,y)] + ...)|^2 \\ &\approx \delta^2(\mathbf{k}) + \sigma_e^2 |\mathcal{F}[v_z(x,y)|^2) \end{aligned} \tag{I.5}$$

The first term is a peak at reciprocal space origin, formed by all the unscattered electrons (i.e., the center beam). The second term is Fourier transform of projected potential (i.e., the reciprocal space structure). Notably, in real experiments, the Fourier transform of the SA aperture is convolved to Eq. I.5 and Dirac delta functions will be well-behaved. In addition, the center beam is often blocked in order to prevent over-saturating sensitive camera components.

The projection-slice theorem (Eq. I.6) states that a Fourier transform of projection is

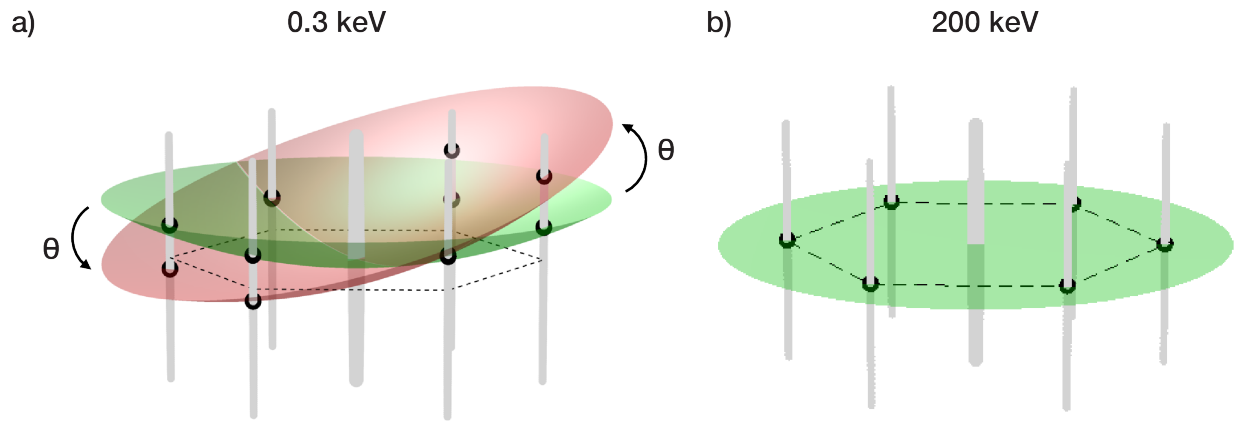

Figure I.2: Ewald's sphere and specimen tilt. a-green) schematic diagram of Ewald's sphere at 0.3 keV represented along reciprocal lattice structure of a monolayer graphene (gray). Low energy is chosen to highlight the curvature of Ewald's sphere. red) Tilting specimen is equivalent to rocking the Ewald's sphere. b) Ewald's sphere at 200 keV—a realstic incident electron energy.

mapped to a planar slice in the reciprocal space. Mathematically:

$$F(\mathbf{k})|_{k_z=0} = \mathcal{F}_{x,y}\left[\int_{-\infty}^{\infty} dz\ f(x,y,z)\right] \tag{I.6}$$

Therefore, electron diffraction measures a planar slice through reciprocal space structure the atomic potential, along side a bright center beam.

$$I(\mathbf{k}) = \delta^2(\mathbf{k}) + \sigma_e^2 V^2(\mathbf{k})|_{k_z=0} \tag{I.7}$$

This approximation works well for $\sigma_e v_z(\mathbf{r}) \ll 1$—with high energy electron and thin specimen with light elements. In order to accurately describe the diffraction of real specimens, more complicated approximation such as Bloch wave propagation or multislice propagation is required [10].

To improve the accuracy of our analytic description of electron diffraction, we consider Ewald's sphere (Fig. I.2). Eq. I.7 implies that we may obtain information from arbitrarily high frequency ($|\mathbf{k}| \to \infty$). Intuitively we should not be able to measure any features smaller than the incident electron wave length. Electron diffraction is an elastic process; the wave vector of scattered electron should conserve its length. The result is that electron diffraction measures reciprocal space information along a spherically curved surface, called Ewald's sphere (Fig. I.2a-green). An immediate consequence of the Ewald's sphere is that the information transfer is limited to a critical frequency, $k_c = 2\pi/\lambda$, as expected.

Because of the Ewald's sphere curvature, electron diffraction measures information slightly above $k_z = 0$ plane—known as the excitation error. Notably, at infinite incident electron energy the Ewald's sphere becomes flat and Eq. I.7 becomes accurate again. As shown in Figure I.2b) at typical TEM operation energy, Ewald's sphere is very flat. In Chapter II, the excitation error in TEM is experimentally measured and discussed in more detail.

This kinematic approximation including excitation error due to Ewald's sphere accurately describes diffraction of 2D materials much thinner than the mean free path (e.g. $\ll$ 150 nm for 200 keV electron in Si [11]) where multiple scattering is negligible.

Because electron diffraction measures only a slice of information, Ewald's sphere needs to be tilted (Fig. I.2a-red) in order to collect the full 3D reciprocal space information. This is analogous to how computed tomography (CT) measures 3D information. The next chapter will give a comprehensive description to the 3D reciprocal space structure of 2D materials and 3D electron diffraction will be introduced as the experimental method to decipher complex 3D structure of 2D materials.

References

[1] *The Nobel Prize in Physics 1914. NobelPrize.org. Nobel Prize Outreach AB 2023.* https://www.nobelprize.org/prizes/physics/1914/summary, Accessed: 2023-04-20.

[2] *The Nobel Prize in Physics 1915. NobelPrize.org. Nobel Prize Outreach AB 2023.* https://www.nobelprize.org/prizes/physics/1915/summary, Accessed: 2023-04-20.

[3] R. E. Franklin and R. G. Gosling, "Molecular configuration in sodium thymonucleate", Nature **171**, 740–741 (1953) 10.1038/171740a0.

[4] L. de Broglie, "Recherches sur la théorie des quanta", Ann. Phys. (Paris) **10**, 22–128 (1925) 10.1051/anphys/192510030022.

[5] G. P. Thomson and A. Reid, "Diffraction of Cathode Rays by a Thin Film", Nature **119**, 890 (1927) 10.1038/119890a0.

[6] C. J. Davisson and L. H. Germer, "Reflection of electrons by a crystal of Nickel", P. Natl. Acad. Sci. USA **14**, 317–322 (1928) 10.1073/pnas.14.4.317.

[7] *The Nobel Prize in Physics 1986. NobelPrize.org. Nobel Prize Outreach AB 2023.* https://www.nobelprize.org/prizes/physics/1986/summary, Accessed: 2023-04-18.

[8] *The Nobel Prize in Chemistry 2011. NobelPrize.org. Nobel Prize Outreach AB 2023.* https://www.nobelprize.org/prizes/chemistry/2011/summary, Accessed: 2023-04-18.

[9] P. E. Batson, N. Dellby, and O. L. Krivanek, "Sub-ångstrom resolution using aberration corrected electron optics", Nature **418**, 617–620 (2002) 10.1038/nature00972.

[10]E. J. Kirkland, *Advanced computing in electron microscopy*, 2nd ed. (Springer, 2010).

[11]K. Iakoubovskii, K. Mitsuishi, Y. Nakayama, and K. Furuya, "Mean free path of inelastic electron scattering in elemental solids and oxides using transmission electron microscopy: atomic number dependent oscillatory behavior", Phys. Rev. B **77**, 104102 (2008) 10.1103/PhysRevB.77.104102.

Chapter II

Reciprocal Structures of 2D Materials

The characteristics of layered two-dimensional (2D) materials and heterostructures are intimately linked with stacking order, as thickness and interlayer registry dramatically alter the confinement and symmetry of the system. For instance, inversion symmetric monolayer 1T-MoS_2 is metallic [1] while mirror symmetric monolayer 2H-MoS_2 is a direct band gap semiconductor [2]. In several 2D systems, the intrinsic inversion asymmetry or symmetry breaking via external perturbation bear possibilities for electronic switching [3, 4] or valleytronic devices [5]. Recently, superconductivity was observed in bilayer graphene when the interlayer twist is tuned to a 'magic angle' [6].

High-precision characterization of stacking order, interlayer spacing, twist, and roughness is paramount to harnessing the diversity of 2D phenomena. The field of 2D materials erupted with facile identification of single layer graphene when exfoliated onto $\sim$300 nm thick SiO_2 substrates [7]. Since then, thickness characterization techniques have expanded to Raman spectroscopy [8], atomic force microscopy [9], and electron microscopy [10]. Thickness alone, however, provides an incomplete picture of the atomic structure and stacking order. Scanning transmission electron microscopy (STEM) can image thickness with atomic resolution [11, 12], yet, this real-space projection of the specimen loses out-of-plane information, poorly discerns light elements bonded to heavy elements, and requires high radiation doses. Furthermore, a fundamental trade-off between resolution and field-of-view limits atomic resolution imaging to small regions of interest, typically $(20\text{ nm})^2$. In contrast, electron diffraction remains a longstanding powerful tool for obtaining a representative average of the atomic structure across large areas, at lower doses, with high-throughput and high precision.

We demonstrate electron diffraction is particularly apt for probing the three-

dimensional (3D) structure of 2D materials. Contrary to the confined real-space structure, we show 2D materials have striking, measurable features in the third dimension of reciprocal space that describe key structural parameters such as stacking order, twist, strain, chemistry, and inter- or intra- layer spacing. In 2D materials, Bragg peaks extend into near infinite rods running perpendicular to the specimen surface. Each Bragg rod oscillates with intensity and phase described by the atomic arrangement within and between each 2D layer.

Prominent distinctions arise in the reciprocal (k) space structure of 2D materials: ∘ In-plane lattice strain moves the position of Bragg rods. ∘ Rod oscillation frequencies are inversely proportional to inter- and intra-layer spacing. ∘ Out-of-plane strain changes the oscillation frequency. ∘ Symmetry and structure of first order rods (Γ_1) reveal stacking order. ∘ Second order (Γ_2) facilitates thickness determination. ∘ TMD chemistry changes the amplitude of oscillations. ∘ Twisted layers are described by a superposition of diffraction patterns for non-overlapping (incommensurate) Bragg rods. ∘ Progressive broadening of rods is associated with out-of-plane micro-corrugation and stiffness. ∘ Curvature of the Ewald sphere results in a small, measurable excitation error in the diffraction pattern that breaks expected Friedel symmetry.

Combining specimen tilt and diffraction, we construct 'diffraction tilt-patterns' which measure the 3D structural details of single and multilayer 2D materials. This work substantially extends previous work for few-layer graphene [13, 14] and boron nitride [15] to transition metal dichalcogenides (TMDs) and multilayer materials. Furthermore, we expound the foundational details required to enable a wide range 3D diffraction analysis across all 2D materials.

Background to Diffraction of 2D Materials

We are challenged to discern the third dimension of 2D materials in real and reciprocal space. Graphene is an archetypal 2D crystal where sp^2 bonding forms a hexagonal lattice lying within a single plane. Graphene's real-space lattice, $V_g(\mathbf{r}) = \text{Ш}_{\mathbf{a}_1,\mathbf{a}_2}(\mathbf{r})\delta(z) \circledast \sum_j f(\mathbf{r} - \mathbf{r}_j)$, is described by two lattice vectors, $\mathbf{a}_1$, $\mathbf{a}_2$, with magnitude $a_g = 2.46$ Å, and a two atom sublattice at $\mathbf{r}_j$ $(j \in 0, 1)$ that mimics a honeycomb. The corresponding reciprocal lattice of graphene defines Bragg rods spaced $b_g = \frac{4\pi}{a_g\sqrt{3}} = 2.949$ Å^{-1}apart and is described by :

$$V_g(\mathbf{k}) = \text{Ш}_{\mathbf{b}_1,\mathbf{b}_2}(\mathbf{k}) \cdot S_g(\mathbf{k}) \tag{II.1}$$

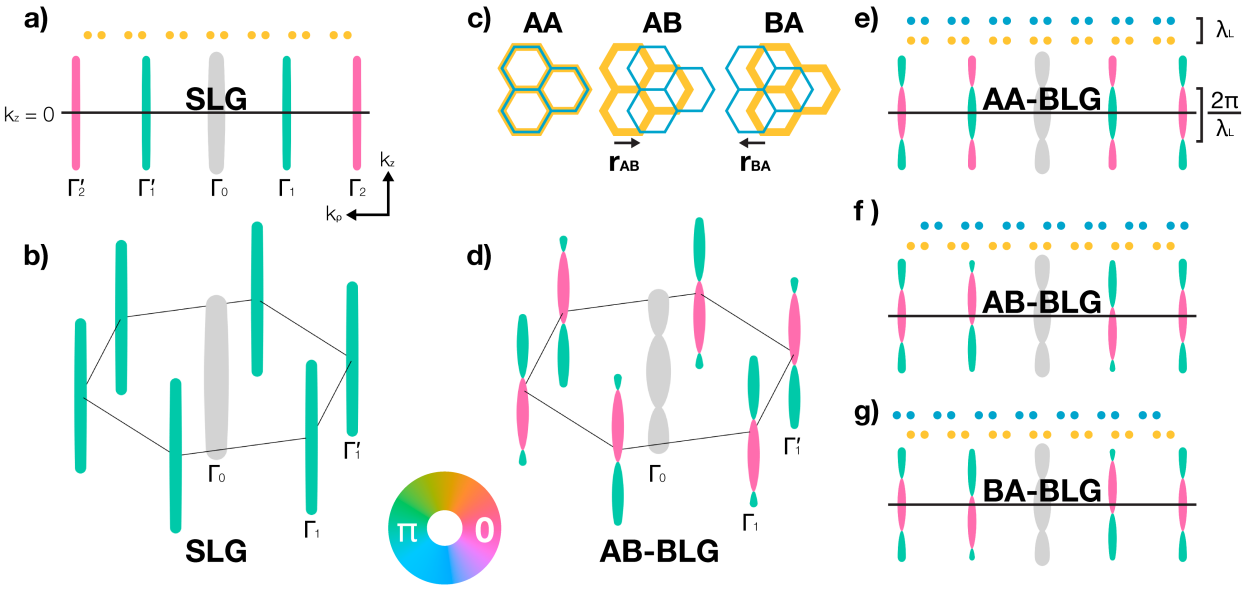

Figure II.1: 3D reciprocal structure of Single and Bilayer Graphene. 3D reciprocal space structure of a,b) single layer graphene (SLG). Width and color of Bragg rods indicate magnitude and phase (magenta = 0, teal = π), the hexagon marks $k_z = 0$ plane. c) Bilayer graphene (BLG) illustrated for AA, AB, and BA registry along $\hat{\mathbf{z}}$. d) 3D k-space structure of AB-BLG. Sinusoidal magnitude—signature of multilayer systems— is apparent. The structure of e) AA, f) AB and g) BA from side view are shown for both first (Γ_1) and second (Γ_2) order Bragg rods along with atomic stacking along <100> direction in real-space. The barely visible decay in rod magnitude seen in SLG is due to the finite size of carbon atoms. The rod structure of BLG's are sinusoidal with symmetry identical to the real-space. 6-fold symmetry of SLG and inversion symmetry of Bernal BLG is clearly shown in k-space. All structures are centered around the inversion center in real-space to maximize interpretability.

where the complex magnitude is determined by structure factor $S_g(\mathbf{k}) = \sum_j f(\mathbf{k}) e^{-i\mathbf{k}\cdot\mathbf{r}_j}$. For graphene, the single atomic plane, with near infinite confinement along $\hat{\mathbf{z}}$ (Fig. II.1a-*top*), has a reciprocal structure with near infinite extent out-of-plane along $\hat{\mathbf{k}}_z$(Fig. II.1a-*bottom*). Similar elongated rel-rods arise from planar shape factors [16, 17] that have been studied in surface layer diffraction experiments on bulk materials and thin-films [18–20]. Appendix A.1 discusses $\text{Ш}(\mathbf{k})$ formulation and normalization prefactor.

Therefore, 2D materials have Bragg peaks that stretch into rods. Figure II.1a,b shows single layer graphene (SLG) in reciprocal space. Its k-lattice has 6-fold rotational symmetry (Fig. II.1b), reflecting the real-space symmetry at the inversion center. The rod intensity decays slowly from the origin due to the small but finite size of each atom (described by atomic scattering factor $f(\mathbf{k})$). The attenuating magnitude reaches 80% by 0.038 Å^{-1}. Both first (Γ_1) and second order (Γ_2) rods are shown in Figure II.1a. For SLG, the more distant second order Bragg rods have ~94% of the squared magnitude of the first order rods.

Combining specimen tilt and diffraction allows quantification of each Bragg rod's 3D

structure. In a 'diffraction tilt-pattern', diffraction peaks are quantified across specimen tilt angles. As the specimen is tilted about an axis perpendicular to the beam direction, the diffraction plane rotates through the reciprocal rods of the material as shown in Figure II.2a for the first order rods of bilayer graphene. Figure II.2b illustrates the resulting tilt pattern, and the inset notes the specimen tilt axis.

Diffraction peaks both move and broaden when a 2D crystal is tilted and must be handled during quantification. Approaching higher tilts, peaks move outward from the axis of rotation—giving the illusion of unidirectional strain. The increasing distance between Bragg peaks reflects the apparent contraction in real-space when a tilted 2D crystal is viewed in projection. Thus, diffraction peaks are minimally spaced apart when the 2D crystal is perpendicular to the beam (i.e. 'on-axis'). Also, the effective selected area increases as tilt increases and a geometric factor of $\cos(\theta)^{-2}$ must be incorporated to the kinematic model of diffraction of large crystals.

Bragg peaks also broaden at higher tilts due to out-of-plane rippling of the material. J.C. Meyer et al. quantified intrinsic microscopic roughing of graphene by measuring the Bragg rod precession [21]. Any micro-corrugation in a 2D sheet has local orientation changes that tilt the Bragg rods. Because selected area electron diffraction (SAED) measures an average of the crystal region, the superposition of tilted Bragg rods results in broadening along $\hat{\mathbf{k}}_z$. J.C. Meyer et al. measured Bragg rod broadening to quantify roughness of graphene and showed that suspended single layer graphene had a surface normal that varied by ± 5 degrees while bilayer graphene was smoother with a ± 1 degree variation. Their work also highlights the importance of quantifying Bragg peaks from integrated intensities—not peak maxima.

Bilayer Graphene

Atomically registered bilayer materials have Bragg rods that sinusoidally oscillate in complex magnitude (Fig. II.1d) with periodicity $(4\pi/\lambda_L)$ inversely proportional to the interlayer spacing, λ_L. The period of rod oscillation is independent of stacking order and depends only on interlayer spacing. Bilayer graphene (BLG) has reciprocal structure de-

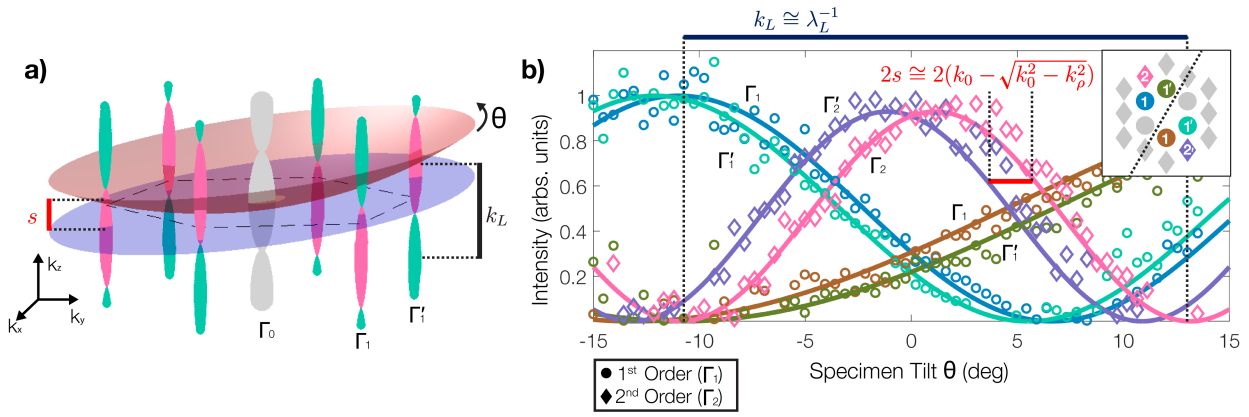

Figure II.2: Diffraction tilt-patterns of BLG. a) 3D reciprocal rod structure of Bernal stacked bilayer graphene. The magnitude varies sinusoidally with a periodicity inversely proportional to real-space interlayer spacing ($k_L = \frac{4\pi}{\lambda_L}$). At typical TEM operation energy (blue, 200 keV), SAED is a near planar slice through the k-space origin; red surface exaggerates the curvature of Ewald sphere with slow electron (0.3 keV). Tilting the specimen in TEM column changes the beam's incident angle and effectively rocks the diffraction plane with respect to the Bragg rods, accessing out-of-plane information hidden in conventional TEM. The excitation error (s)—due to the curvature—is small but not negligible at low tilt angles close to the k-space origin. b) Kinematic (−) and experimental (○, ◊) tilt-patterns of BLG. The tilt-patterns oscillates with frequency k_L. Non-trivial Ewald sphere curvature separates analogous 2nd order Friedel pair tilt-patterns (magenta(Γ_2) and blue(Γ_2')) with phase difference associated with s.

scribed by:

$$V_{bg}(\mathbf{r}) = \big[\text{Ш}_{\mathbf{a}_1,\mathbf{a}_2}(\mathbf{r} - \boldsymbol{\Delta}/2)\delta(z - \lambda_L/2) + \text{Ш}_{\mathbf{a}_1,\mathbf{a}_2}(\mathbf{r} + \boldsymbol{\Delta}/2)\delta(z + \lambda_L/2)\big] \circledast \textstyle\sum_i f(\mathbf{r} - \mathbf{r}_i) \tag{II.2}$$

$$V_{bg}(\mathbf{k}) = \text{Ш}_{\mathbf{b}_1,\mathbf{b}_2}(\mathbf{k})\big[2\cos\big(\frac{\lambda_L}{2}k_z + \frac{\boldsymbol{\Delta}}{2}\cdot\mathbf{k}\big)\big]\cdot S_g(\mathbf{k}) \tag{II.3}$$

where $\boldsymbol{\Delta}$ is the order parameter representing in-plane translation.

Changes to stacking order move Bragg rods up and down along $\hat{\mathbf{k}}_z$. More specifically, in-plane displacement of a layer, $\boldsymbol{\Delta}$, adds a phase shift $\frac{1}{2}\boldsymbol{\Delta}\cdot\mathbf{k}$ to the sinusoidal intensity of each Bragg rod. There are three high-symmetry stacking configurations for BLG: energetically stable AB or BA (called Bernal or graphitic) and unstable AA (Fig. II.1c) [22]. The arrangement of the sinusoidal rods reflect the real-space symmetry. AA-BLG is defined by two aligned layers ($\boldsymbol{\Delta} = 0$) with a mirror plane in-between (Fig. II.1e). The reciprocal space structure matches the real-space 6-fold symmetry with a mirror plane at $k_z = 0$. In AB/BA-BLG, one layer is bond-length shifted with respect to the other along an in-plane bond direction ($\boldsymbol{\Delta} = \frac{\mathbf{a_1}+\mathbf{a_2}}{3}$) [23]. This translation breaks out-of-plane mirror symmetry and reduces the 6-fold symmetry to 3-fold.

Figure II.1e,f,g depicts the rod structure of AA, AB, and BA-BLG. The magnitude of each rod is described by its width and complex phase with color; magenta and teal represent 0 and π respectively. Mirror symmetric AA-BLG has first order diffraction rods (Γ_1) centered about $k_z = 0$ (Fig. II.1c). For AB-BLG, the in-plane translation between atomic layers displaces Γ_1 and Γ_1' Bragg rods in opposite out-of-plane directions ($\pm\hat{\mathbf{k}}_z$) with a $\pi/3$ phase shift (Fig. 1f, g).

Γ_1 rods reveal stacking order in 2D materials. For Bernal BLG the maximum intensity of odd order Bragg rods can only be measured by tilting the specimen (Fig. II.2a). In the experimental tilt-pattern of AB-BLG (Fig. II.2b), the non-symmetric first order Bragg rods are obvious. The blue Γ_1 curve decreases to zero intensity at 6 degrees tilt but reaches a maximum tilt at -12 degrees (also expected at 23 degrees). The brown Γ_1 rod on the other side of the rotation axis follows a similar opposite trend. Bragg rods more distant from the axis of rotation oscillate more rapidly in the tilt pattern. Here the axis of rotation passes through Γ_2 as shown in Figure II.2b-*inset*. In real-space, the maximum intensity of Γ_1 occurs when Bernal bilayer graphene is tilted so all atoms between layers lie atop one another when viewed along the beam direction. For AB and BA the patterns are mirrored and maximum intensity occurs when tilting opposite directions. Brown et al. exploited this broken symmetry using specimen tilt to quickly distinguish AB and BA domains in bilayer graphene [13]. For AA-BLG the maximum diffraction intensity trivially occurs at 0 degree tilt.

Γ_2 rods reveal the number of layers in multilayer graphene, but not stacking order. For untilted specimens ($k_z \approx 0$), the intensity of the Γ_2 rods in the bilayer is four times that of monolayer graphene and will continue to scale with number of layers squared, N^2, as discussed in section II. Shown in Figure II.1e–g, the Γ_2 rods are identical and indiscernible for all three BLG stacking orders. Γ_2 rod intensity has a mirror symmetric maxima at $k_z = 0$ that is clearly seen in the experimentally measured tilt-pattern (Fig. II.2b). The slight deviation of Γ_2 maxima from zero tilt is due to finite curvature of the Ewald sphere.

Beam Energy & the Ewald Sphere

Elastic scattering preserves kinetic energy on the proverbial Ewald sphere in reciprocal space [24]. At finite beam energies, the diffraction pattern is described by a spherical surface cutting through the reciprocal lattice. At typical TEM energies (60–300 keV), the curvature of the Ewald sphere is small but not negligible. As shown in Figure II.2a, the Ewald sphere passes through Bragg rods slightly above the $k_z = 0$ plane (historically

referred to as excitation error, s). Tilting the specimen is equivalent to tilting the Ewald sphere.

Diffraction tilt-patterns come in Friedel pairs [25] comprised of a Bragg rod (at $\mathbf{k}$) and its centrosymmetric pair (at $-\mathbf{k}$). For a flat Ewald sphere (infinite beam energy) the Friedel pairs have equivalent tilt-patterns. However, with Ewald curvature the tilt patterns for each Friedel pair bifurcate with increasing separation at lower beam voltages (higher curvature). Figure II.2b shows the measurable curvature of the Ewald sphere in an experimental diffraction tilt-pattern of bilayer graphene. Here, curves appear in pairs offset by a few degrees. This is most clearly seen in Γ_2 diffraction (Fig. II.2b *pink, purple*) where the maximum intensity occurs at $\pm 1.1°$. This angular distance in the split of paired tilt-patterns directly measures the Ewald sphere curvature and excitation error s: $s = k_0 - \sqrt{k_0^2 - k_\rho^2}$ where k_0 is the wavenumber of the incident electron and k_ρ is the in-plane radial distance to k-space origin. For small tilt angles and Bragg peaks close to the k-space origin this will scale approximately linearly, while for larger angles at larger radial distances a conversion from specimen tilt to a Cartesian basis is detailed in Appendix A.2. Here, the $\pm 1.1°$ split in the low-angle tilt-patterns corresponds to an excitation error of 0.085 Å^{-1}at 80 keV.

Twisted, Moiré Layers

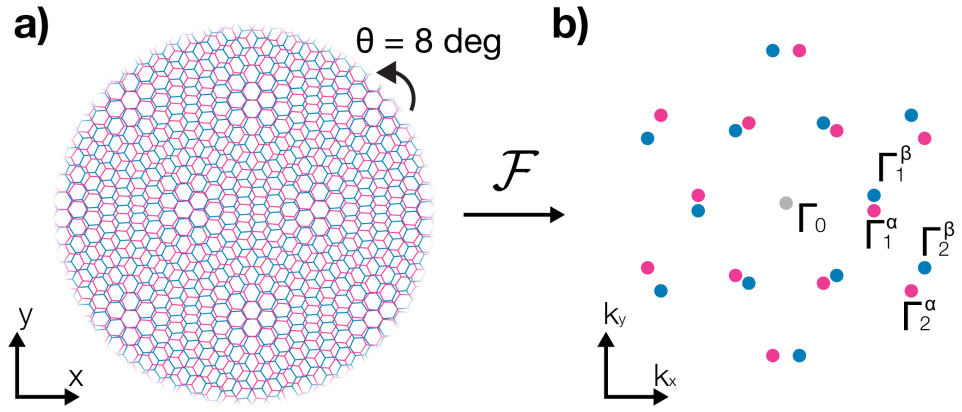

Figure II.3: Twisted Bilayer Graphene. a) Twisted bilayer graphene with an incommensurate intralayer twist angle ($\theta = 8$ deg). b) Reciprocal structure of incommensurate tBLG is a simple superposition of layers.

Significant interest in twisted multilayer materials has followed the micromechanical exfoliation of 2D heterojunctions [26] and discovery of superconductivity in low-twist angle bilayer graphene [6]. The reciprocal lattice of twisted bilayers is described by $|\mathcal{F}[\text{Ш}_\alpha(\mathbf{r}) + \text{Ш}_\beta(\mathbf{r})]|^2 = |\text{Ш}_\alpha(\mathbf{k})|^2 + |\text{Ш}_\beta(\mathbf{k})|^2 + \text{Ш}_\alpha^*(\mathbf{k})\text{Ш}_\beta(\mathbf{k}) + \text{Ш}_\alpha(\mathbf{k})\text{Ш}_\beta^*(\mathbf{k})$, for layers α

and β. For incommensurate stacking, the cross term is zero and the diffraction pattern is a trivial superposition of each individual layer (Fig. II.3). This allows independent characterization of each incommensurate layer; however, we lose the ability to characterize interlayer spacing. If α and β are commensurate [27], the cross term is zero where the Bragg rods from each layer do not overlap. Only overlapping rods may interfere and sinusoidally oscillate. As shown by Brown et al., each twisted layer can be independently mapped in real space with dark field TEM by placing an aperture around each distinct Bragg peak in the diffraction plane of the TEM [13].

H. Yoo et al. recently reported at low-twist angles (< 3 deg) in bilayer graphene periodic restructuring occurs and superlattice peaks emerge [28]. Systems with periodic lattice distortions (PLDs), either from interlayer interaction or charge order, are not so simply described as a superposition of layers[29, 30]. In Chapter III, we will dive deep and describe the complex periodic relaxation behavior using torsional PLDs.

2D Transition Metal Dichalcogenides

Transition metal dichalcogenides (TMDs) are comprised of three atomic planes and two chemical species within each van der Waals (vdW) layer that add complexity to the Bragg rod structure (Fig. II.4a,c,e-*top*). Six chalcogens encapsulate each metal atom geometrically with two tetrahedrons. Single layer TMDs are categorized into hexagonal 'H' or trigonal 'T' polytype phases by this local metal-chalcogen coordination complex [31]. In the H-phase, the two tetrahedrons align along $\hat{\mathbf{z}}$ (Fig. II.4a), and in the T-phase, the two are displaced by 30 degrees giving rise to inversion symmetry (Fig. II.4e). Although isomeric to the 1T, the 2H phase notably breaks this inversion symmetry within a single layer but regains it in the bilayer. Broken inversion symmetry can significantly change electronic structure and has been associated with a metal-insulator transition in the 1T $\rightarrow$ 2H transformation [1, 2] and the indirect to direct band gap transition in 2H TMDs reduced to a single layer (1H) [2]. In several TMDs, such as TaS_2 and $TaSe_2$, the 1T phase permits room temperature charge ordering and even superconductivity at higher pressures [32].

Diffraction combined with specimen tilt can precisely determine metal-chalcogen coordination within a single vdW layer due to its sensitivity to crystal symmetry. The three atomic planes comprising a vdW layer are described by Bragg rods oscillating with a periodicity inversely proportional to λ_ℓ, the intralayer spacing between chalcogen-chalcogen

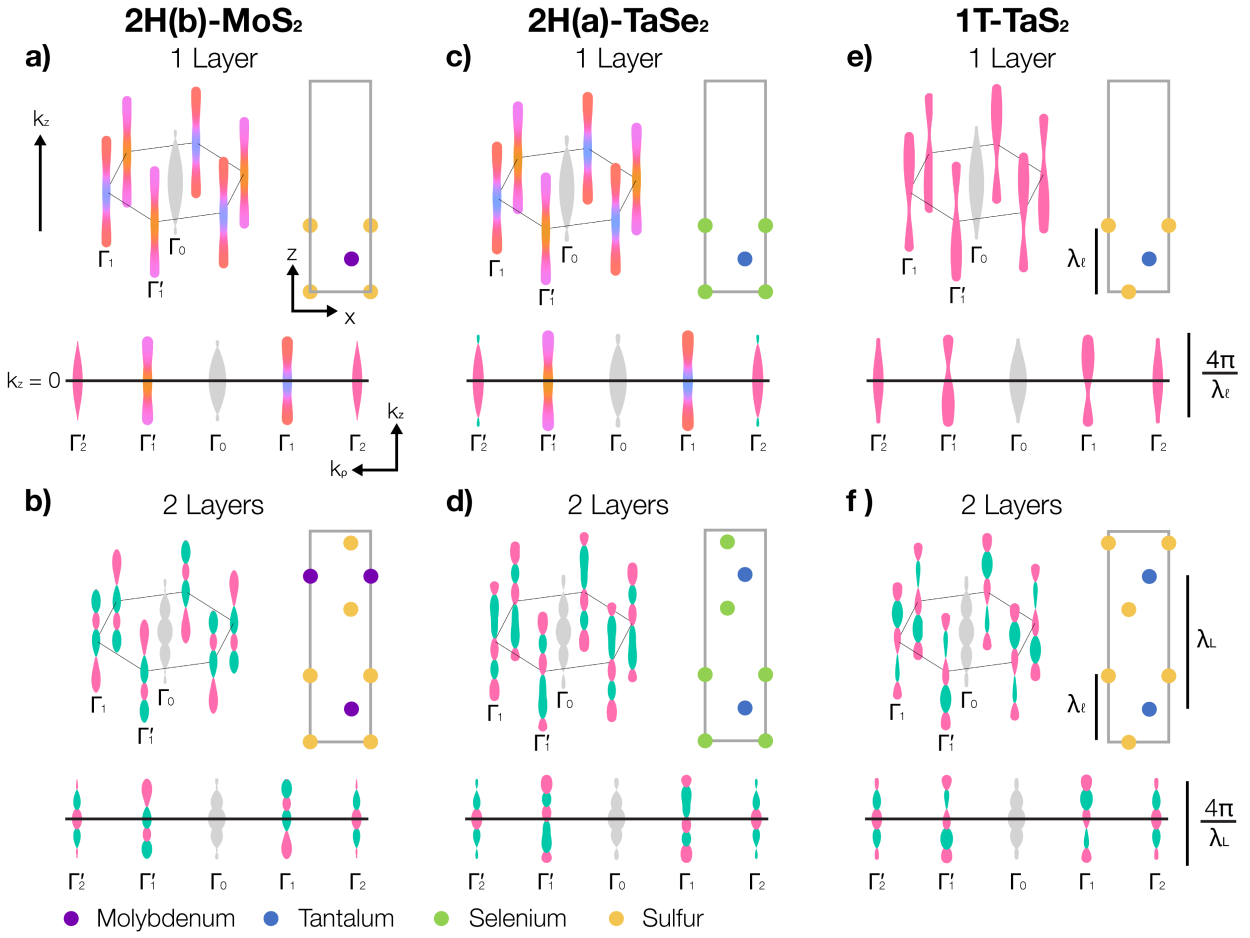

Figure II.4: 3D reciprocal structure of 2D transition metal dichalcogenides and polytypes. For each TMD, the Bragg rods (Γ_0, Γ_1) are shown in 3D alongside a real-space <100> projection of the crystal stacking order. Below, a sideview of the Bragg rods (Γ_0, Γ_1, Γ_2) quantitatively illustrates the structure in k-space. Bragg rods have thickness and color indicating the complex magnitude and phase respectively. For single layer TMDs (a,c,e), two sinusoidal oscillations are determined by the interlayer spacing of the 3 atomic planes. The complexity increases noticeably for 2 vdW layers (b,d,f) which includes a beating frequency from interlayer spacing. Noticeably, H-phase MoS_2 and $TaSe_2$ have different stable multilayer stacking, denoted 2H(b) and 2H(a), leading to drastically different Bragg rod contours.

atomic planes:

$$V_{1H}(\mathbf{k}) = \text{Ш}_{\mathbf{b}_1,\mathbf{b}_2}(\mathbf{k})[f_m(\mathbf{k}) + 2f_c(\mathbf{k})e^{-i\mathbf{k}\cdot\mathbf{r}_0}\cos\left(k_z\frac{\lambda_\ell}{2}\right)] \tag{II.4}$$

$$V_{1T}(\mathbf{k}) = \text{Ш}_{\mathbf{b}_1,\mathbf{b}_2}(\mathbf{k})[f_m(\mathbf{k}) + 2f_c(\mathbf{k})\cos\left(\mathbf{k}\cdot\mathbf{r}_0 + k_z\frac{\lambda_\ell}{2}\right)] \tag{II.5}$$

where f_m and f_c are the atomic scattering factors of the metal and chalcogen atoms, respectively, and $\mathbf{r}_0$ is the in–plane metal–chalcogen bond direction ($\mathbf{r}_0 = \frac{\mathbf{a}_1+\mathbf{a}_2}{3}$). 1H denotes monolayer 2H.

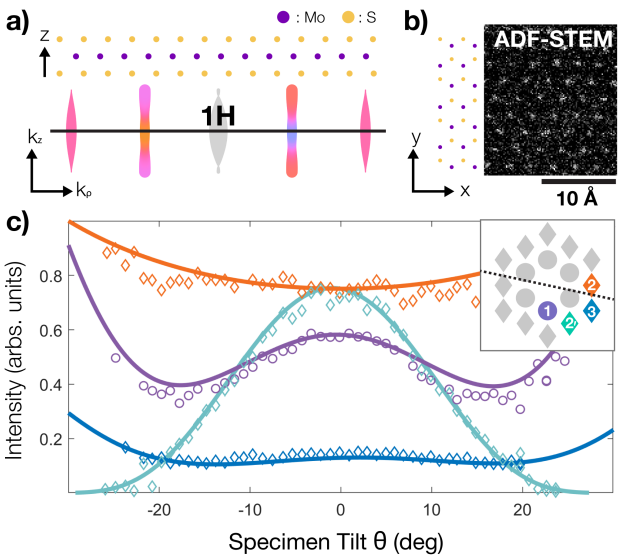

Figure II.5: K-structure of monolayer 2H-MoS_2. The real and k-space structure of monolayer a) 2H-MoS_2 polytype shows mirror symmetry distinct from 1T. However, b) real-space schematic and ADF-STEM image along $\hat{\mathbf{z}}$ shows classification of 2H and 1T phase is extremely difficult because Mo atom intensities overwhelm S atoms. c) Directly probing the rod structure, the experimental tilt-pattern shows clear mirror symmetry and shows good agreement with the 2H analytic model.

Figure II.4-*top* highlights the 3D reciprocal space structure of several monolayer TMDs. The change in metal-chalcogen coordination drastically changes the Bragg rod structure (Fig. II.4 a,c vs. e), whereas the change in chemical composition alters the contour of the rod intensities (Fig. II.4 a vs. c). The broken inversion symmetry of the 1H structure is represented in the complex phase of Eq. II.4 that continuously changes on the Γ_1 Bragg rod along $\hat{\mathbf{k}}_z$ (Fig. II.4 a,c)—this phase is not measurable from the diffraction amplitude. The 1T Γ_1 rods are markedly distinct with strong asymmetric oscillation of amplitude. Similar to graphene, we see TMDs possess Γ_2 rods symmetric about $k_z = 0$ and insensitive to chalcogen coordination.

The experimental tilt-pattern of an exfoliated MoS_2 flake shown in Figure II.5 reveals a single layer H phase. The Γ_1 and Γ_3 curves (Fig. II.5c-*purple,blue*) are symmetric about $\theta = 0$ degree, which indicates a mirror plane at $k_z = 0$. This feature clearly discerns monolayers of the 2H and 1T polytypes (see also Appendix A.10, A.11). The kinematic model of monolayer 2H-MoS_2 closely matches the experimental result (Fig. II.5c). Although monolayer 2H and 1T phases have different projected structure in real-space, the light sulfur atoms are virtually invisible in high-angle annular dark field (HAADF) STEM making this distinction challenging to characterize in real space (Fig. II.5b).

The intralayer spacing in a 2D TMD is precisely quantified by diffraction tilt-patterns

for the first time. Nonlinear regression analysis of the experimental monolayer 2H-MoS_2 data reveals an intralayer chalcogen-chalcogen spacing (λ_ℓ) of 3.07 Å with a 95% confidence interval of $\pm$ 0.11 Å based on a kinematic model. Multiple scattering may further reduce precision, especially in thicker systems containing strong scatterers. Our single layer value is comparable to the previously reported 3.01 Å for bulk 2H-MoS_2 [33].

The addition of a second vdW layer opens a wider range of stacking configurations and the Bragg rod complexity expands quickly—with 3 Fourier coefficients per vdW layer. Most notably, bilayer gains a beat frequency described by the interlayer spacing, λ_L. The interlayer beating is concisely expressed for bilayer 1T: $V_{2T}(\mathbf{k}) = V_{1T}(\mathbf{k}) \cdot 2\cos\left(k_z \frac{\lambda_L}{2}\right)$. The rapid rod oscillation from the larger vdW gap ($\lambda_L > \lambda_\ell$) beats with intralayer oscillations to create a non-uniform spacing between amplitude minima and maxima.

Additionally, multilayer TMDs have several stacking geometries both within and between their vdW layers. For instance, 2H-MoS_2 and 2H-$TaSe_2$ have distinct structures, typically denoted as 2H(b) and 2H(a) respectively (Fig. II.4b,d). The Bragg rod structure for single layer and bilayer T and H phases are shown in Figure II.4. Appendix A.8 provides an atlas of TMD stacking geometries and illustrates the distinct structures in k-space that allow unique identification and quantification.

Multilayer 2D Materials

Here we use multilayer graphene to illustrate how diffraction tilt-patterns can characterize thicker 2D materials. In atomically registered multilayer graphene, there are three possible sublattice positions—A,B,C—each one bond-length apart from the others (Fig. II.6a). The two ordered stackings, hexagonally symmetric AB (Bernal) and rhombohedrally symmetric ABC, have been shown to have dramatically different band structures and transport properties [34, 35]. However, thickness and stacking order determination is particularly difficult for samples more than three layers thick. In bulk materials, the rods give way to discrete peaks along $\hat{\mathbf{k}}_z$(Appendix A.6, but at intermediate thicknesses (3–15 layers) they still contain interpretable out-of-plane structural information. Although the possible stacking configurations grows exponentially with thickness, leveraging minimal prior knowledge about the specimen significantly reduces the number of possibilities and makes exact determination of structure tractable.

Here, we characterize the out-of-plane structure of mechanically exfoliated 6- and 12-layer graphene samples. At these intermediate thicknesses, the number of graphene layers

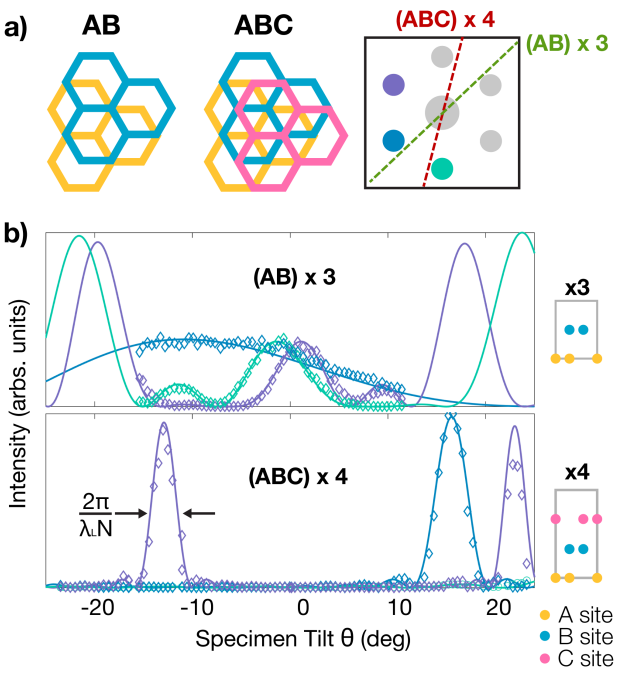

Figure II.6: Diffraction tilt-patterns of multilayer Bernal and rhombohedral graphene. a) real-space stacking of Bernal (AB) and rhombohedral (ABC) graphene layers. b) Experimental diffraction tilt-patterns are plotted along with matched kinematically modeled patterns. Top right inset labels the plotted Bragg rods and specimen tilt axis.

is redundantly described by the width of each Bragg rod along $\hat{\mathbf{k}}_z$ ($\Delta k_z = \frac{2\pi}{\lambda_L N}$), the angle which the 2nd order peak first reaches zero while tilting with an axis of rotation along Γ_1 ($N = \frac{21}{\theta(deg)}$), and the intensity of the second order Bragg Rod ($I = 4\frac{\sin^2 ½k_z\lambda_L N}{\sin^2 ½k_z\lambda_L}$). These three relationships are derived in Appendix A.3, A.4 from analytic models of multilayer graphene.

By measuring the relative intensity of the 1st and 2nd order Bragg peaks ($|\Gamma_1/\Gamma_2|$) at zero tilt ($k_z = 0$), we can determine the fraction of each sublattice in the system. For instance, with equal number of all three sublattices' layers (e.g. ABCABC) the first order Bragg peaks have zero intensity; if the system has only two sublattices' layers in equal number (e.g. ABAB) the relative intensity is 0.25 (Appendix A.5).

Applying these rules to the tilt-pattern in Figure II.6b-*top*, we determined the sample has 6 layers and an equal number of A and B sublattices. Registered 6-layer graphene has 3^5 possible configurations. Eliminating the trivial duplicates and those with incorrect sublattice proportions leaves only 7 possible stacking orders from which we matched the correct stacking—ABABAB—by comparison with kinematically modeled tilt-patterns.

Likewise, the sample in Figure II.6b-*bottom* was found to be 12 layers thick with an equal proportion of A,B, and C sublattices, allowing the stacking order to be classified as

ABCABCABCABC; the rhombohedral ordered stacking. Fast identification of rhombohedral graphene may have importance in fabrication of 2D heterostructure devices.

Summary & Conclusion

Dimensionally confined 2D materials have rich 3D structure in reciprocal space described by near-infinite Bragg rods that oscillate with complex magnitude encoding the out-of-plane structure. Using a simple kinematic model of diffraction, combined with specimen tilt, the structure of these Bragg rods has been mapped in detail for several 2D materials (graphene, TMDs) across a range of stacking geometries. Using this 3D diffraction technique, we probed out-of-plane structure and symmetry to quantitatively determine critical structural parameters such as inter- & intra-layer spacings and stacking order in multilayer graphene and TMDs. For single layer MoS_2 we extracted a chalcogen-chalcogen layer spacing of 3.07 ± 0.11 Å. We accurately characterized the full interlayer stacking order of bilayer to multilayer graphene (demonstrated up to 12 layers), as well as identified multilayer rhombohedral graphene. The physical and electronic properties of layered 2D materials are often dramatically susceptible to these parameters. Although efficiently extracted with 3D diffraction, out-of-plane features are challenging or impossible to extract using real-space optical or surface measurement methods. However, our results are obtained using a rudimentary TEM available at most institutions. With the increasing complexity of multilayered materials, engineered by composition, twist, and stacking order—the foundational details outlined in this manuscript enable rapid and / or high-precision characterization across the complete class of 2D materials. Reciprocal structures illustrated throughout the manuscript and Appendix A provide a 2D materials atlas for 3D diffraction. Furthermore, this work directly empowers a broader range of advanced diffraction based imaging techniques—such as dark-field TEM and 4D STEM—capable of mapping structural order in real space.

References

[1] M. Acerce, D. Voiry, and M. Chhowalla, "Metallic 1T phase MoS_2 nanosheets as supercapacitor electrode materials", Nat. Nanotechnol. **10**, 313–318 (2015) 10.1038/nnano.2015.40.

[2] A. Splendiani, L. Sun, Y. Zhang, T. Li, J. Kim, C.-Y. Chim, G. Galli, and F. Wang, "Emerging Photoluminescence in Monolayer MoS_2", Nano. Lett. **10**, 1271–1275 (2010) 10.1021/nl1903868w.

[3] E. V. Castro, K. S. Novoselov, S. V. Morozov, N. M. R. Peres, J. M. B. Lopes dos Santos, J. Nilsson, F. Guinea, A. K. Geim, and A. H. Castro Neto, "Biased bilayer graphene: semiconductor with a

gap tunable by the electric field effect", Phys. Rev. Lett. **99**, 216802 (2007) 10.1103/PhysRevLett.99.216802.

[4]T. Ohta, A. Bostwick, T. Seyller, K. Horn, and E. Rotenberg, "Controlling the electronic structure of bilayer graphene", Science **313**, 951–954 (2006) 10.1126/science.1130681.

[5]J. R. Schaibley, H. Yu, G. Clark, P. Rivera, J. S. Ross, K. L. Seyler, W. Yao, and X. Xu, "Valleytronics in 2D materials", Nat. Rev. Mater. **1**, 16055 (2016) 10.1038/natrevmats.2016.55.

[6]Y. Cao, V. Fatemi, S. Fang, K. Watanabe, T. Taniguchi, E. Kaxiras, and P. Jarillo-Herrero, "Unconventional superconductivity in magic-angle graphene superlattices", Nature **556**, 43–50 (2018) 10.1038/nature26160.

[7]P. Blake, E. W. Hill, A. H. Castro Neto, K. S. Novoselov, D. Jiang, R. Yang, T. J. Booth, and A. K. Geim, "Making graphene visible", Appl. Phys. Lett. **91**, 063124 (2007) 10.1063/1.2768624.

[8]A. C. Ferrari, J. C. Meyer, V. Scardaci, C. Casiraghi, M. Lazzeri, F. Mauri, S. Piscanec, D. Jiang, K. S. Novoselov, S. Roth, and A. K. Geim, "Raman spectrum of graphene and graphene layers", Phys. Rev. Lett. **97**, 187401 (2006) 10.1103/PhysRevLett.97.187401.

[9]K. S. Novoselov, A. K. Geim, S. V. Morozov, D. Jiang, Y. Zhang, S. V. Dubonos, I. V. Grigorieva, and A. A. Firsov, "Electric field effect in atomically thin carbon films", Science **306**, 666–669 (2004) 10.1126/science.1102896.

[10]X. Li, W. Cai, J. An, S. Kim, J. Nah, D. Yang, R. Piner, A. Velamakanni, I. Jung, E. Tutuc, S. K. Banerjee, L. Colombo, and R. S. Ruoff, "Large-area synthesis of high-quality and uniform graphene films on copper foils", Science **324**, 1312–1314 (2009) 10.1126/science.1171245.

[11]N. Alem, Q. M. Ramasse, C. R. Seabourne, O. V. Yazyev, K. Erickson, M. C. Sarahan, C. Kisielowski, A. J. Scott, S. G. Louie, and A. Zettl, "Subangstrom edge relaxations probed by electron microscopy in hexagonal boron nitride", Phys. Rev. Lett. **109**, 205502 (2012) 10.1103/PhysRevLett.109.205502.

[12]P. Y. Huang, C. S. Ruiz-Vargas, A. M. van der Zande, W. S. Whitney, M. P. Levendorf, J. W. Kevek, S. Garg, J. S. Alden, C. J. Hustedt, Y. Zhu, J. Park, P. L. McEuen, and D. A. Muller, "Grains and grain boundaries in single-layer graphene atomic patchwork quilts", Nature **469**, 389 (2011) 10.1038/nature09718.

[13]L. Brown, R. Hovden, P. Huang, M. Wojcik, D. A. Muller, and J. Park, "Twinning and Twisting of Tri- and Bilayer Graphene", Nano. Lett. **12**, 1609–1615 (2012) 10.1021/nl204547v.

[14]J. Ping and M. S. Fuhrer, "Layer number and stacking sequence imaging of few-layer graphene by transmission electron microscopy", Nano. Lett. **12**, 4635–4641 (2012) 10.1021/nl301932v.

[15]C.-J. Kim, L. Brown, M. W. Graham, R. Hovden, R. W. Havener, P. L. McEuen, D. A. Muller, and J. Park, "Stacking Order Dependent Second Harmonic Generation and Topological Defects in h-BN Bilayers", Nano. Lett. **13**, 5660–5665 (2013) 10.1021/nl403328s.

[16]A. L. G. Rees and J. A. Spink, "The shape transform in electron diffraction by small crystals", Acta Crystallogr. **3**, 316–317 (1950) 10.1107/S0365110X50000823.

[17]J. M. Cowley, A. L. G. Rees, and J. A. Spink, "The morphology of zinc oxide smoke particles", Proc. Phys. Soc. B **64**, 638–644 (1951) 10.1088/0370-1301/64/8/303.

[18]M. Henzler, "Spot profile analysis (LEED) of defects at silicon surfaces", Surf. Sci. **132**, 82–91 (1983) 10.1016/0039-6028(83)90533-2.

[19]M. G. Lagally, D. E. Savage, and M. C. Tringides, "Diffraction from disordered surfaces: an overview", in *Reflection high-energy electron diffraction and reflection electron imaging of surfaces*, edited by P. K. Larsen and P. J. Dobson (Springer US, Boston, MA, 1988), pp. 139–174, 10.1007/978-1-4684-5580-9_11.

[20]I. K. Robinson, "Crystal truncation rods and surface roughness", Phys. Rev. B **33**, 3830–3836 (1986) 10.1103/PhysRevB.33.3830.

[21]J. C. Meyer, A. K. Geim, M. I. Katsnelson, K. S. Novoselov, T. J. Booth, and S. Roth, "The structure of suspended graphene sheets", Nature **446**, 60–63 (2007) 10.1038/nature05545.

[22]A. M. Popov, I. V. Lebedeva, A. A. Knizhnik, Y. E. Lozovik, and B. V. Potapkin, "Commensurate-incommensurate phase transition in bilayer graphene", Phys. Rev. B **84**, 045404 (2011) 10.1103/PhysRevB.84.045404.

[23]J. D. Bernal, "The structure of graphite", Proc. R. Soc. Lond. A **106**, 10.1098/rspa.1924.0101 (1924) 10.1098/rspa.1924.0101.

[24]P. P. Ewald, "Die Berechnung optischer und elektrostatischer Gitterpotentiale", Ann. Phys. (Berlin) **369**, 253 (1921) 10.1002/andp.19213690304.

[25]G. Friedel, "Sur les symétries cristallines que peut révéler la diffraction des rayons Röntgen", C. R. Acad. Sci. **157**, 1533–1536 (1913).

[26]H. Fang, C. Battaglia, C. Carraro, S. Nemsak, B. Ozdol, J. S. Kang, H. A. Bechtel, S. B. Desai, F. Kronast, A. A. Unal, G. Conti, C. Conlon, G. K. Palsson, M. C. Martin, A. M. Minor, C. S. Fadley, E. Yablonovitch, R. Maboudian, and A. Javey, "Strong interlayer coupling in van der waals heterostructures built from single-layer chalcogenides", P. Natl Acad. Sci. USA **111**, 6198–6202 (2014) 10.1073/pnas.1405435111.

[27]E. J. Mele, "Commensuration and interlayer coherence in twisted bilayer graphene", Phys. Rev. B **81**, 161405(R) (2010) 10.1103/PhysRevB.81.161405.

[28]H. Yoo, K. Zhang, R. Engelke, P. Cazeaux, S. H. Sung, R. Hovden, A. W. Tsen, T. Taniguchi, K. Watanabe, G.-C. Yi, M. Kim, M. Luskin, E. B. Tadmor, and P. Kim, Nat. Mater. **18**, 448–453 (2019) 10.1038/s41563-019-0346-z.

[29]S. H. Sung, Y. M. Goh, H. Yoo, R. Engelke, H. Xie, K. Zhang, Z. Li, A. Ye, P. B. Deotare, E. B. Tadmor, A. J. Mannix, J. Park, L. Zhao, and R. Kim P. Hovden, "Two-dimensional charge order stabilized in clean polytype heterostructures", Nat. Commun. **13**, 7826 (2022) 10.1038/s41467-022-35477-x.

[30]R. Hovden, A. W. Tsen, P. Liu, B. H. Savitzky, I. El Baggari, Y. Liu, W. Lu, Y. P. Sun, P. Kim, A. N. Pasupathy, and L. F. Kourkoutis, "Atomic lattice disorder in charge-density-wave phases of exfo-

liated dichalcogenides (1T-TaS_2)", Proc. Natl. Acad. Sci. **113**, 11420–11424 (2016) 10.1073/pnas.1606044113.

[31]J. A. Wilson and A. D. Yoffe, "The transition metal dichalcogenides discussion and interpretation of the observed optical, electrical and structural properties", Adv. Phys. **18**, 193 (1969) 10.1080/00018736900101307.

[32]B. Sipos, A. F. Kusmartseva, A. Akrap, H. Berger, L. Forro, and E. Tutis, "From mott state to superconductivity in 1T-TaS_2", Nat. Mater. **7**, 960–965 (2008) 10.1038/nmat2318.

[33]B. Schönfeld, J. J. Huang, and S. C. Moss, "Anisotropic mean-square displacements (MSD) in single-crystals of 2H- and 3R-MoS_2", Acta Crystallogr. Sect. B **39**, 404–407 (1983) 10.1107/S0108768183002645.

[34]R. Xiao, F. Tasnádi, K. Koepernik, J. W. F. Venderbos, M. Richter, and M. Taut, "Density functional investigation of rhombohedral stacks of graphene: topological surface states, nonlinear dielectric response, and bulk limit", Phys. Rev. B **84**, 165404 (2011) 10.1103/PhysRevB.84.165404.

[35]W. Bao, L. Jing, J. Velasco Jr, Y. Lee, G. Liu, D. Tran, B. Standley, M. Aykol, S. B. Cronin, D. Smirnov, M. Koshino, E. McCann, M. Bockrath, and C. N. Lau, "Stacking-dependent band gap and quantum transport in trilayer graphene", Nat. Phys. **7**, 948 (2011) 10.1038/nphys2103.

Chapter III

Torsional Periodic Lattice Distortions and Diffraction of Twisted 2D Materials

Periodic lattice distortions (PLD) are at the heart of correlated electronic behavior such as superconductivity [1], metal-insulator transitions [2], and charge density waves (CDW) [3]. PLDs are typically intrinsic to a crystal [3, 4], Fermi-surface driven [5], accompanied by a CDW, and have periodicity spanning a few unit cells ($\sim$1–2 nm). However, recently extrinsic van der Waals (vdW) driven superlattices with tunable periodicity (up to a few 100 nm) were discovered in twisted bilayer graphene (TBG) [6]. TBG has been spotlighted for extraordinary correlated electron behaviors for twist at the so-called "magic" angle ($\sim$1.1°) [7]. Yoo et al. showed that magic angle TBG is not a simple superposition of two constituent layers [6], but rather a 2D crystal that periodically restructures at the mesoscale. Subsequent reports showed moiré superlattices of other vdW systems with similar periodic restructuring [8–11]. Furthermore, this restructuring has a dramatic effect on the band-structure, magnetism, and superconducting properties [6, 9, 12]. Therefore, understanding twisted 2D materials requires a full description of the atomistic structure down to picoscale displacements. However, a systematic depiction of restructured moiré superlattices is near absent and limited to descriptions of local stacking geometry.

Here, we show the atomic structure of 2D moiré superlattices at and near the magic angle are concisely and accurately described by a torsional PLD comprised of three transverse displacement waves. In this way, the complexity of low-twist moiré crystal restructuring is reduced to a single PLD order-parameter with an amplitude and wave vector. Each layer in the bilayer system has an equal and opposite torsional PLD amplitude. From quantitative diffraction of low twist-angle and magic angle graphene the atomic displacements of the larger superlattice can be measured. In twisted bilayer graphene we report

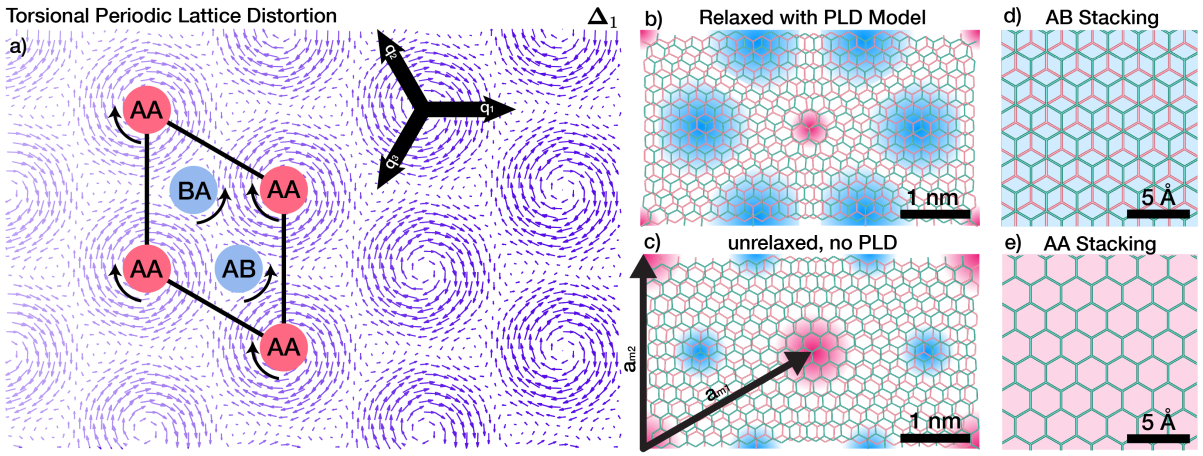

Figure III.1: Periodic Restructuring of Twisted Bilayer Graphene (TBG) a) Displacement field of torsional PLD. Local rotational fields for AA region and AB/BA regions are opposite. By including higher harmonics, PLD can exhibit any arbitrary pattern. The moiré supercell crystal structures of c) pristine TBG and b) restructured TBG with torsional PLD model. Red and blue overlay highlights energetically unfavorable AA stacked region, and stable AB/BA stacked region, respectively. PLD decreases the total energy of the system by expanding AB/BA domain and decreasing AA domain. Crystal structure of d) AB stacked and e) AA stacked bilayer graphene are shown as reference.

a torsional PLD amplitude of 7.8 $\pm$ 0.6 pm and 6.1 $\pm$ 0.4 pm for twist angle (θ) of 1.1° and 1.2° respectively. We report an upper bound for PLD amplitude of twisted bilayer graphene to be 22.6 pm based on interlayer interaction energy. In addition, we show that the torsional PLD amplitudes can be accurately predicted across all twist angles using an analytic model of the vdW stacking and elastic energies. Lastly, we show that this torsional PLD exists across a variety of other layered 2D materials.

Periodic Restructuring in Twisted Bilayer Graphene

Moiré patterns emerge for two rotated lattices. In TBG, two single layers of graphene are stacked with a small interlayer twist (Fig. III.1f). The moiré of this twisted bilayer graphene (TBG) is an alternating pattern of three high symmetry stackings (AA, AB and BA), separated by channels of solitonic, intermediate dislocation (often described as an energetic saddle-point) [13, 14]. In the energetically favorable AB stacking (also called Bernal stacking) half the atoms in one layer are atop atoms in the layer below (Fig. III.1h); BA stacking is the mirror of AB stacking. AA stacking (Fig. III.1i), where all atoms in both layers are aligned, requires much higher energy (~19 meV/atom [15]). Despite the complex super-structure of moiré stacking, the diffraction pattern of TBG is a simple superposition of two rotated single-layer Bragg peaks [16]—validated by quantum mechanical scattering simulation in Figure III.5b and previously measured experimentally at higher twist angles [17].

In low twist-angle bilayer materials, a striking restructuring of the moiré lattice emerges. Dark-field (DF-) TEM [6, 13] and later 4D-STEM [18, 19] revealed that this superlattice corresponds to a triangular array of AB/BA domains. However, domain boundaries soften near or above the magic angle ($\theta \approx 1^\circ$) and a simple array of perfect AB/BA domains fails to correctly capture the full atomistic structure of the twisted system [20, 21].

Here, we show that a PLD model provides a precise and concise description of lattice restructuring in TBG. PLDs are sinusoidal displacements of atomic positions ($\mathbf{r}' = \mathbf{r_0} + \mathbf{A}\sin(\mathbf{q}\cdot\mathbf{r}_0)$; $\mathbf{r}'$, $\mathbf{r}_0$ are deformed and original atomic positions, $\mathbf{q}$ is the wavevector, and $\mathbf{A}$ is the displacement vector). Both longitudinal ($\mathbf{A} \parallel \mathbf{q}$) and transverse ($\mathbf{A} \perp \mathbf{q}$) distortion waves naturally emerge in various charge ordered crystals including 2D materials (e.g. longitudinal: TaS_2 [3, 22], $NbSe_2$ [23]; or transverse: BSCMO [4], UPt_2Si_2 [24]).

A torsional PLD succinctly and accurately describes the relaxed structure of TBG (Fig. III.1c). The torsional displacement field is made from three non-orthogonal, transverse PLDs (Fig. III.1a):

$$\mathbf{\Delta}_n = A_n \sum_{i=1}^{3} \hat{\mathbf{A}}_i \sin(n\mathbf{q}_i \cdot \mathbf{r}_0 + \phi_i); \quad \hat{\mathbf{A}}_i \perp \mathbf{q}_i \tag{III.1}$$

Here, $\mathbf{r}_0$ are undistorted atom positions, $\mathbf{q}_i$ is the PLD wave vector, and $\hat{\mathbf{A}}_i$ is the unit vector describing transversity of PLD. The distorted lattice positions are given by: $\mathbf{r} = \mathbf{r}_0 + \mathbf{\Delta}_n$. Three $\mathbf{q}$'s are 120° apart with a magnitude set by the twist angle ($|\mathbf{q}| \approx b\theta$, b is reciprocal lattice constant) to accommodate symmetry of moiré pattern (See Appendix III.A.). The phase, ϕ_i, shifts or alters the relaxation patterns (Fig. III.2). For TBG, the origin is placed at the AA center ($\phi_i = 0$). Importantly, this torsional wave occurs in both layers, however, the direction of the field in each layer is reversed such that distortions are opposite. Transverse distortions, $\hat{\mathbf{A}}_i \perp \mathbf{q}_i$, are expected when the lattice constants of both layers are equivalent (otherwise longitudinal components, $\hat{\mathbf{A}}_i \parallel \mathbf{q}_i$, may be present). A single torsional PLD ($\mathbf{\Delta}_1$) is typically sufficient to describe the system, however, more generally PLDs with higher order harmonics ($n > 1$) are permissible and the total displacements become sum of multiple harmonics (as discussed later).

Figure III.1a illustrates the displacement field ($\mathbf{\Delta}_1$) from a torsional PLD in one layer of twisted bilayer graphene. The arrows show the direction and magnitude with which atoms displace from their expected lattice sites. The torsional field is a nanoscale trigonal

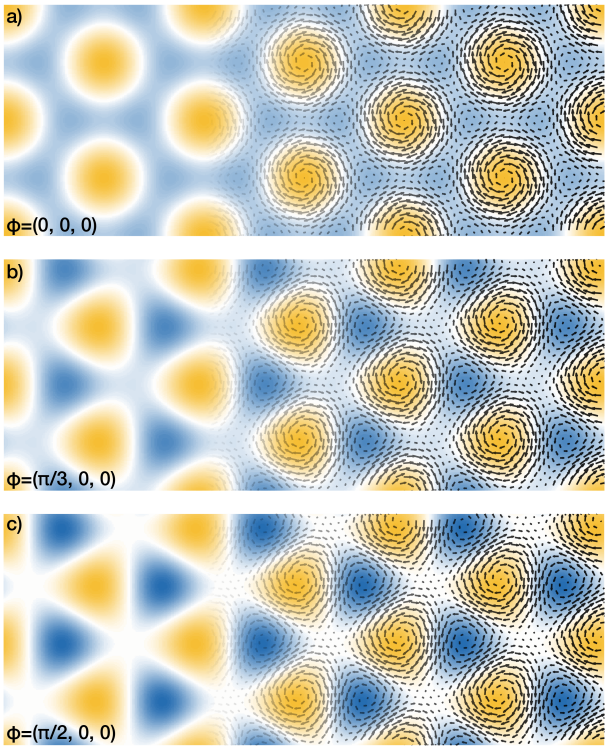

Figure III.2: Relative Phases of torsional PLD Torsional PLD behavior can be controlled by changing the phases (ϕ_i) of constituent sinusoids. Here, rotational field (Ω_1) with $(\phi_1, \phi_2, \phi_3) =$ a) $(0, 0, 0)$, b) $(\pi/3, 0, 0)$, c) $(\pi/2, 0, 0)$ are shown.

lattice of rotational distortions spaced $1/|\mathbf{q}|$ apart. The distortion field exhibits behaviors desired for relaxation of TBG—twisting AA regions in one direction and anti-twisting AB/BA regions in the other. The vdW interaction between layers strives to locally twist (anti-twist) AA (AB/BA) regions to minimize (maximize) interlayer registration and reduce the total interaction energy. The relaxed structure (Fig. III.1c)—obtained by applying displacements to original atomic sites (Fig. III.1d)—acts to maximize the low energy regions with AB/BA stacking and decreases the high energy regions with AA stacking.

Torsional PLDs are immediately apparent in an electron diffraction pattern. This atomic restructuring manifests as superlattice peaks that decorate Bragg peak pairs and appear more pronounced around higher order Bragg peaks. The superlattice peaks represent a symmetry reduction beyond that from the global twist angle. The torsional PLD superlattice peaks in TBG at 1.1° are shown (Fig. III.5a). The azimuthal intensity distribution of superlattice peaks in SAED of 1.1° TBG implies transversity of the distortion wave $(\hat{\mathbf{A}} \perp \mathbf{q})$.

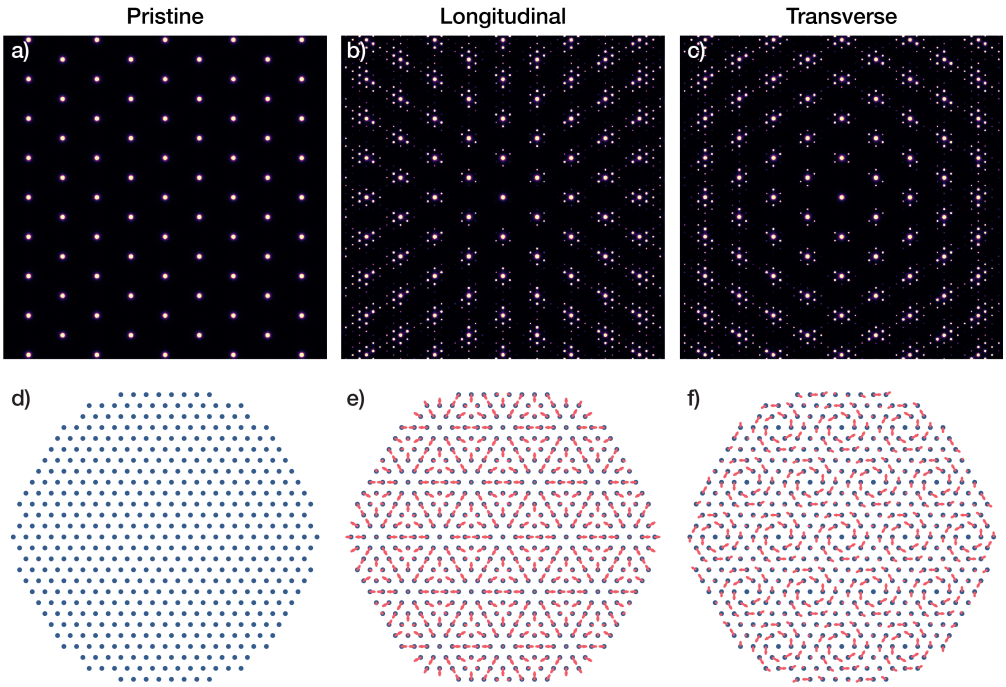

Figure III.3: Transversity of PLD Simulated diffraction of crystal with a) no PLD, b) longitudinal PLD and c) transverse PLD. $|\mathrm{q}|$ is set to be $5a_0$ where a_0 is pristine lattice constant ($a_0 = 5$Å, $|\mathbf{q}| = 5a_0$). Each PLD consists of three PLD waves oriented 120° apart. a) with no PLD, only the usual crystal Bragg peaks are present. b, c) superlattice peaks emerge with PLD. PLD superlattice peaks are located $\alpha\mathbf{q}$ away from Bragg peaks with intensity proportional to $|\mathrm{J}_\alpha(\mathbf{k}\cdot\mathbf{A})|^2$. Note the difference in distribution of superlattice peaks in b and c due to transversity of the PLD. d, e, f) Schematic real space diagram of pristine, longitudinal and transverse PLD. Blue circles represents pristine lattice points and red arrows denote resultant lattice distortion due to PLDs.

Diffraction of Moiré Materials

PLDs diffract into reciprocal space as superlattice peaks that surround each Bragg peak. These superlattice peaks are positioned $\alpha\mathbf{q}$ away from Bragg peaks (Fig. III.5i,j,k). The superlattice peaks have intensities proportional to $|\mathrm{J}_\alpha(\mathbf{k}\cdot\mathbf{A})|^2$ where J_α is a Bessel function of the first kind, $\mathbf{k}$ is the position of the superlattice peak in reciprocal space, and α is an integer [3, 22, 25]. For typical values of $\mathbf{k}$ and $\mathbf{A}$, the Bessel function monotonically increases with $|\mathbf{k}|$ and decreases inversely with the integer α. The appearance of strong superlattice peaks at high-order Bragg spots (i.e. at larger $|\mathbf{k}|$) is a signature for periodic lattice distortions (PLD) (Fig. III.3).

The dot product $(\mathbf{k}\cdot\mathbf{A})$ reveals transversity of PLDs in twisted bilayer materials. In reciprocal space, the transverse PLDs manifest as a distribution of superlattice peaks that are stronger along the azimuthal direction (Fig. III.3c). In contrast, a longitudinal PLD would produce superlattice peaks that become stronger radially along Bragg vectors (Fig. III.3b). The torsional PLD in TBG results from the superposition of three transverse PLDs.

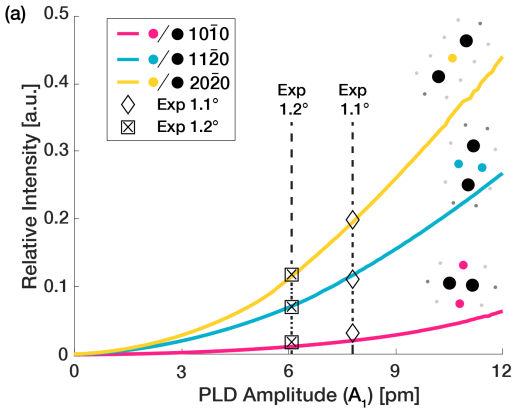

Figure III.4: Quantification of Torsional PLD Amplitude A_1 (a) Relative intensities of superlattice peaks to Bragg peaks of first order (red), second order (blue), and third order (yellow) diffraction spots characterized over a range of PLD amplitudes. The plot reveals that 1.1° and 1.2° rTBG are relaxed by single harmonic torsional PLD with amplitude 7.8 pm and 6.1 pm, respectively.

The torsional PLD quantitatively describes experimental observations of twisted bilayer diffraction—superlattice peaks near higher order Bragg peaks have higher intensities, and superlattice peak intensities increase monotonically as PLD amplitude increases. The torsional PLD in TBG is validated by quantum mechanical multislice simulation. Simulated SAED patterns (Fig. III.5f,g,h) show excellent agreement with experimental data (Fig. III.5c,d,e). More specifically, the relative superlattice to Bragg peak intensity and distribution of simulated superlattice peaks are consistent.

The torsional PLD in TBG is primarily described by a single amplitude coefficient (A_1). We report a torsional PLD amplitude (A_1) of 7.8 $\pm$ 0.6 pm for $\theta = 1.1°$ and 6.1 $\pm$ 0.4 pm for $1.2°$ near the magic angle in TBG. The PLD amplitude was quantified by matching experimental and simulated diffraction intensities (Fig. III.4). Torsional PLD amplitudes for additional twist angles are plotted in Figure III.6a—showing a decrease in amplitude as twist angle is increased and ultimately disappearing above $3.89°$.

Critical Twist Angles and the Low-twist Regime

Below a $3.89°$ twist angle, atomic distortions in TBG exceed a picometer $(A_1 > 1$ pm). The periodic relaxation of TBG results from competition between interlayer van der Waals stacking energy benefit (V_{vdW}) and elastic cost of distortion (V_{El}) [26]. Elastic energy cost to accommodate a torsional PLD with amplitude A_1, assuming Hookean elasticity, is $2\sqrt{3}\pi^2 G A_1^2$ for each layer, where G is shear modulus of graphene (9.01 eV/Å^2 [20]) (Fig. III.6b, top, blue, derived in Appendix B.4). Notably, the elastic energy per supercell is independent of the twist angle, and hence of moiré supercell size. For van der Waals

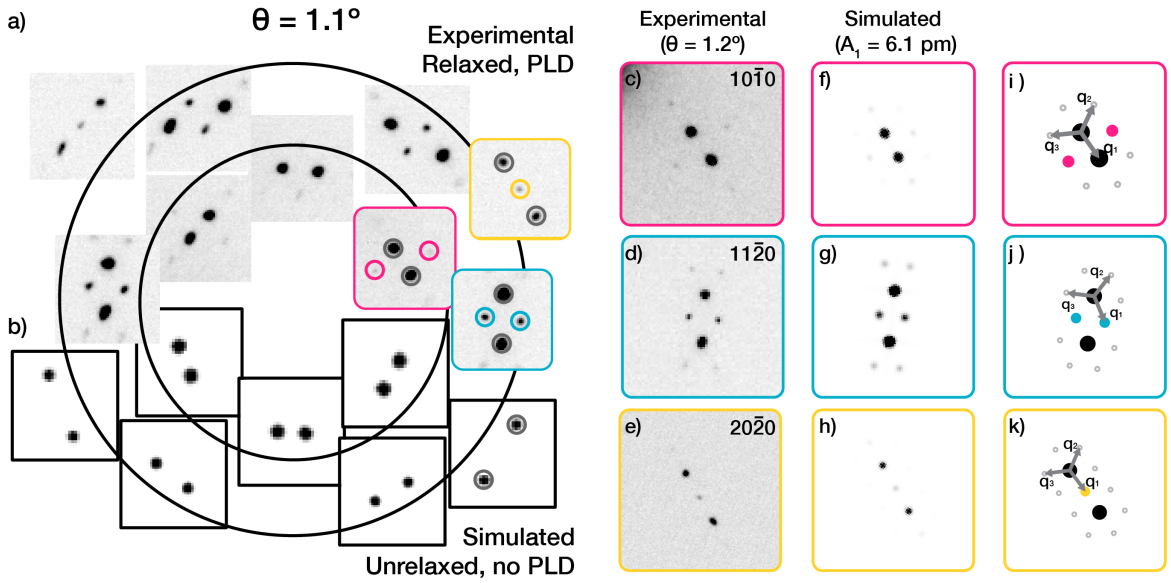

Figure III.5: Torsional Periodic Lattice Distortion (PLD) Model a) Electron diffraction of TBG ($\theta = 1.1°$) displays superlattice peak complexes in addition to two sets of Bragg peaks, marked by gray circles. b) The simulated diffraction pattern of unrelaxed TBG only shows two sets of Bragg peaks. Multislice simulation f–h) for PLD with only single harmonic (A_1 = 6.1 pm) matches greatly with the experimental data c–e). i–k) Schematic illustration shows PLD wave vectors ($\mathbf{q}_i$'s) in relation to Bragg and superlattice peaks.

interaction, V_{vdW}, we employ Kolmogorov and Crespi's model [27] and compute the interlayer energy as function of PLD amplitude. V_{vdW} has two salient features: first, energy per moiré supercell is proportional to the area of the cell ($\propto \theta^{-2}$) and second, V_{vdW} minimum is at $A_1 = A_{max} = 20.35$ pm (Fig. III.6b, top red). Therefore, at large θ where V_{El} dominates total energy, the total energy is at minimum at small A_1. In contrast, as θ decreases, A_1 approaches 20 pm.

We report a upper and lower bound of the PLD amplitude, A_1, to be 0 pm and 22.6 pm, respectively. Local rotation due to the torsional PLD ($\Omega_1 = \frac{1}{2}\nabla \times \mathbf{\Delta}_1$) near AB region is $\frac{3qA_1}{4}$. For graphene (a = 2.46 Å), A_1 of 22.6 pm will restore all local twist in each layer ($|\Omega_1| = \frac{\theta}{2}$). Negative A_1 amplitude is energetically unfavorable as it increases the local twist angle which decreases the AB domain size. See Appendix B.2 for detailed discussion.

The interlayer interaction energy V_{vdW} of TBG is excellently approximated by a quadratic function within the geometrically-allowed region of A_1 ($0 \leq \theta \leq 22.6$ pm). A non-linear least squares fit gives semi-empirical model of $V_{vdW} = \frac{2v_0}{\theta^2}(A_1 - A_{max})^2$ where $v_0 = 0.0732$ eV Å^{-2} and $A_{max} = 20.35$ pm. Notably, A_{max} corresponds to energetically allowed maximum A_1. The total energy of TBG with a torsional PLD is $V_{tot} = 4\sqrt{3}\pi^2 G A_1^2 + \frac{2v_0}{\theta^2}(A_1 - A_{max})^2$. Minimizing V_{tot} with respect to A_1 gives a Lorentzian func-

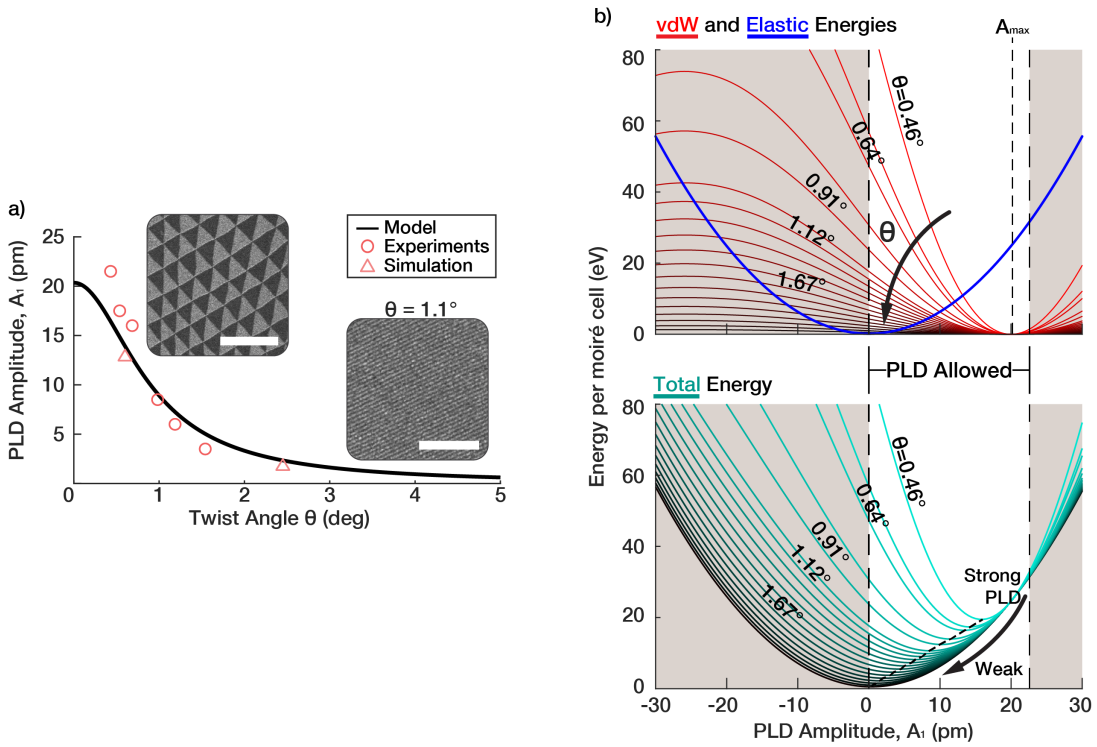

Figure III.6: Energy and Amplitude of PLDs in Twisted Bilayer Graphene (TBG) a) Torsional PLD model predicts the PLD amplitude (A_1) of TBG vs twist angle (θ) follows Lorentzian. Extracted torsional PLD amplitude (A_1) from experimental SAED (red circles) and computationally relaxed (red triangles) matches well with the Lorentzian model. Scale bars are 500 nm (0.1°) and 150 nm (1.1°) b) Top panel: V_{vdW} (red) and V_{El} (blue) of TBG with torsional PLD. Lighter region denotes geometrically allowed PLD amplitude ($0 \leq A_1 \leq$22.6 pm). Note that elastic cost of torsional PLD is twist angle independent, and V_{vdW} is proportional to θ^{-2} and has minimum at A_1 = 20.35 pm. Bottom panel: total energy landscape ($V_{vdW} + V_{El}$) of TBG with torsional PLD. θ dependence of V_{vdW} shifts the total energy minimum to stronger PLD.

tion:

$$A_1(\theta) = A_{max}(1 + \frac{2\pi^2\sqrt{3}G}{v_0}\theta^2)^{-1} \tag{III.2}$$

Eq. III.2 (Fig. III.6a, black) matches excellently with A_1 extracted from experimental data and simulations (Fig. III.6a red). The amplitude of the PLD exceeds 1 pm below 3.89° twist—which we define as the low-twist angle regime in TBG. Note, only at the lowest angles below $\sim 0.5^\circ$ do we see a slight underestimation from the Lorentzian model; suggesting higher order distortions become noticeable.

Sharp PLD Boundaries at Extreme Low-Twist Angles

We report at lower twist angles ($\theta \lesssim 0.5^\circ$), TBG relaxes with more complexity, thus roughly defining the extreme low-twist regime. Comparing diffraction patterns at higher θ (e.g., 1.1°, Fig. III.5a) and lower θ (e.g., 0.4°, Fig. III.10a), lower twist angle SAED patterns

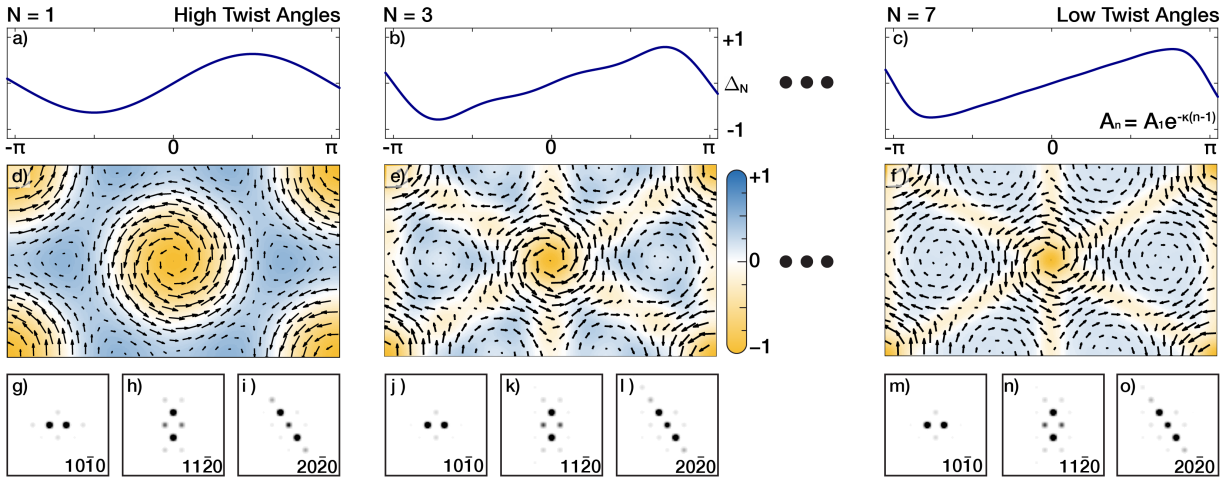

Figure III.7: PLDs as a Fourier Series in 2D Moiré Materials a–c) Evolution of periodic wave (Δ) as higher harmonic waves b) N=3, c) N=7) are included; Δ is normalized displacement magnitude over one period along one direction. Fourier coefficients (A_n) are tailored as exponential decay, which produces to a smooth 'sawtooth'-like waveform. Including harmonic waves allows high frequency (i.e. sharp) features in resultant waves. d–f) Torsional PLD structure with higher harmonic PLD included. The color denotes the amount of local rotation (Ω_N) due to the PLD displacement field (arrows). g–i) Quantum mechanical electron diffraction simulations of TBG with single harmonic torsional PLD captures the distortions in high twist angles (i.e. near magic-angle and higher) well. j–o) Adding higher harmonics slightly modifies the diffraction patterns and shows qualitatively better matches with low twist angle systems.

show not only stronger superlattice peaks, but also different distribution of superlattice peaks with higher order superlattice peaks. This is attributed to the sharpening of soliton boundaries between AB and BA domains. Yoo et al.'s work suggested that dislocation boundaries become more well-defined at low twist angles using DF-TEM. Even at zero-twist, soliton boundaries have been reported [13, 17]. In the extreme low-θ regime, shear soliton boundaries reach a minimum width previously reported to be 6.2 ± 0.6 nm [13]. However even when soliton boundaries have minimal width, as θ decreases these boundaries become a smaller fractional area of the moiré supercell. Thus, at extreme low-twist the PLD needs to be generalized to include an additional number (N) of Fourier harmonics to accommodate sharper boundaries:

$$\mathbf{\Delta}_N = \sum_{n=1}^{N} \mathbf{\Delta}_n \tag{III.3}$$

The Fourier coefficient A_n dictates the texture of a torsional PLD. Figure III.7d,e,f shows evolution of a torsional PLD as higher order Fourier harmonics are included. The arrows represent the displacement field of the torsional PLD and the colored overlay represents the local rotational field (Ω_N, see Appendix B.4) in one of the layers; the opposing layer has an equal and opposite local rotational field ($-\Omega_N$). Figure III.7d shows a tor-

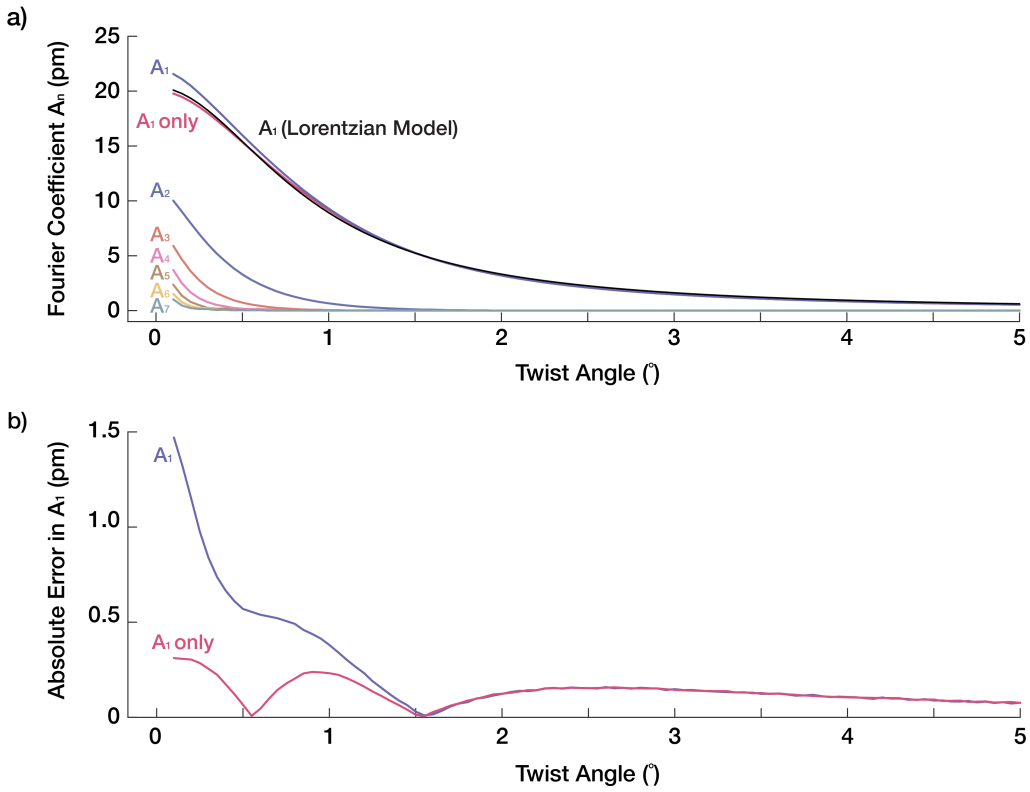

Figure III.8: Contribution of PLD Harmonics across Twist Angles a) Amplitude of nth order PLD harmonics (A_n) against twist angle. PLD amplitudes are obtained by minimizing total energy ($V_{vdW}+V_{El}$) with up to 9th order harmonic PLD included. At higher twist angle A_1 is dominant, and A_2, A_3, A_4 exceed 1 pm at $\theta \lesssim 0.9°$, 0.45°, 0.3° respectively. Magenta 'A_1 only' was obtained by minimizing the total energy with A_1 included. A_1 traces the Lorentzian model well at high θ and slightly deviates at $\theta \lesssim 0.5°$. b) Absolute error of Lorentzian model with respect to A_1 (blue) and 'A_1 only' (red).

sional PLD with a single coefficient. The PLD rotational field reveals most of relaxation is facilitated through twisting circular AA regions (orange). In contrast, with higher harmonics included (Fig. III.7e,f) triangular AB/BA regions are anti-twisted (blue) to maximize Bernal stacking within the system in addition to twisting AA regions. Fourier coefficient design produces Ω_N field pattern that matches previous reported experimental results of local twist fields [18]. Although each harmonic PLD wave contributes elastic energy independently (see Appendix B.6), this is not true for the interlayer van der Waals energy. In Fig. III.7e,f, A_n decays exponentially ($A_n = A_1 e^{-\kappa(n-1)}$); analogous to a smooth 'sawtooth'-like wave in one-dimensional wave (Fig. III.7a,b,c). Notably, for a smooth—i.e. infinitely differentiable—wave, exponential decay is the upper bound for Fourier coefficients (Paley-Wiener theorem).

The PLD amplitudes for higher harmonics (A_n) are calculated by minimizing the total interlayer and intralayer energies. Each higher order term becomes non-negligible in-

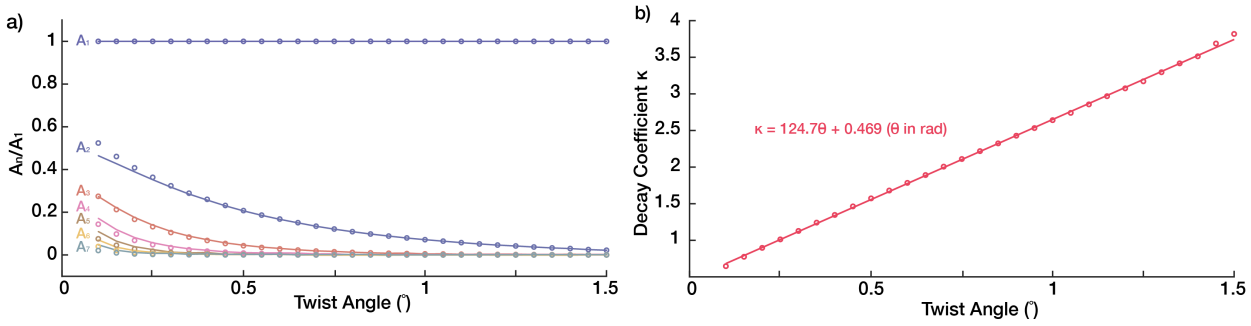

Figure III.9: Exponential Decay of PLD Harmonics a) Relative amplitude of PLD harmonics to fundamental harmonic (A_n/A_1) plotted versus twist angle (circles) closely follows exponential decay ($A_n = A_1 e^{-\kappa(\theta)\cdot(n-1)}$) (line). b) Decay parameter, κ, is linear proportional to θ. Therefore, decreasing θ slows down decay of A_n. Notably, exponential decay is the upper bound for Fourier coefficients (Paley-Wiener theorem)

crementally at smaller angles. A_2, A_3, and A_4 will exceed 1 pm at $\theta \lesssim 0.9°$, $0.45°$, and $0.3°$ respectively (Fig. III.8). We describe the extreme low-twist regime to be when A_3 becomes significant (> 1 pm), however, this demarcation is imprecise. A_n decays exponentially with coefficient $\kappa(\theta)$ linearly proportional to the twist angle ($A_n = A_1 e^{-\kappa(\theta)\cdot(n-1)}$). Thus, decreasing θ retards decay of A_n and higher harmonics becomes more significant (Fig. III.9). The fundamental PLD amplitude, $A_1(\theta)$, remains well described by the empirical Lorentzian, Eq. III.2, even when higher-order harmonics are present. If harmonics are ignored, the computed value of A_1 will deviate by more than 1 pm at twist angles below $\theta < 0.25°$ but never exceed ~10%. Noticeably, the inclusion of higher harmonics creates torsional PLD texture that allow enhancement of A_1 in the extreme low twist angle regime.

Multislice simulation of SAED (Fig. III.7g–o) shows that the distribution of superlattice peaks change with the presence of higher harmonics. n-th harmonic PLD waves add intensity to superlattice peaks $n\alpha\mathbf{q}$ away from each Bragg peak (α is the integer in J_α). Figure III.7g–o shows simulated TBG diffraction patterns with higher harmonics have stronger superlattice peaks further away from the Bragg peaks. The change is subtle because higher order harmonics are exponentially weaker.

As θ nears zero, many higher harmonics (N) are needed and the Fourier basis is more cumbersome. Instead, a hard-domain model, where the superlattice is treated as quilt of AA, AB and BA domains with dislocation boundaries may also become suitable. In the limit of zero angle twist, boundaries become the stacking fault boundaries reported by Brown et al. for untwisted bilayer graphene [17].

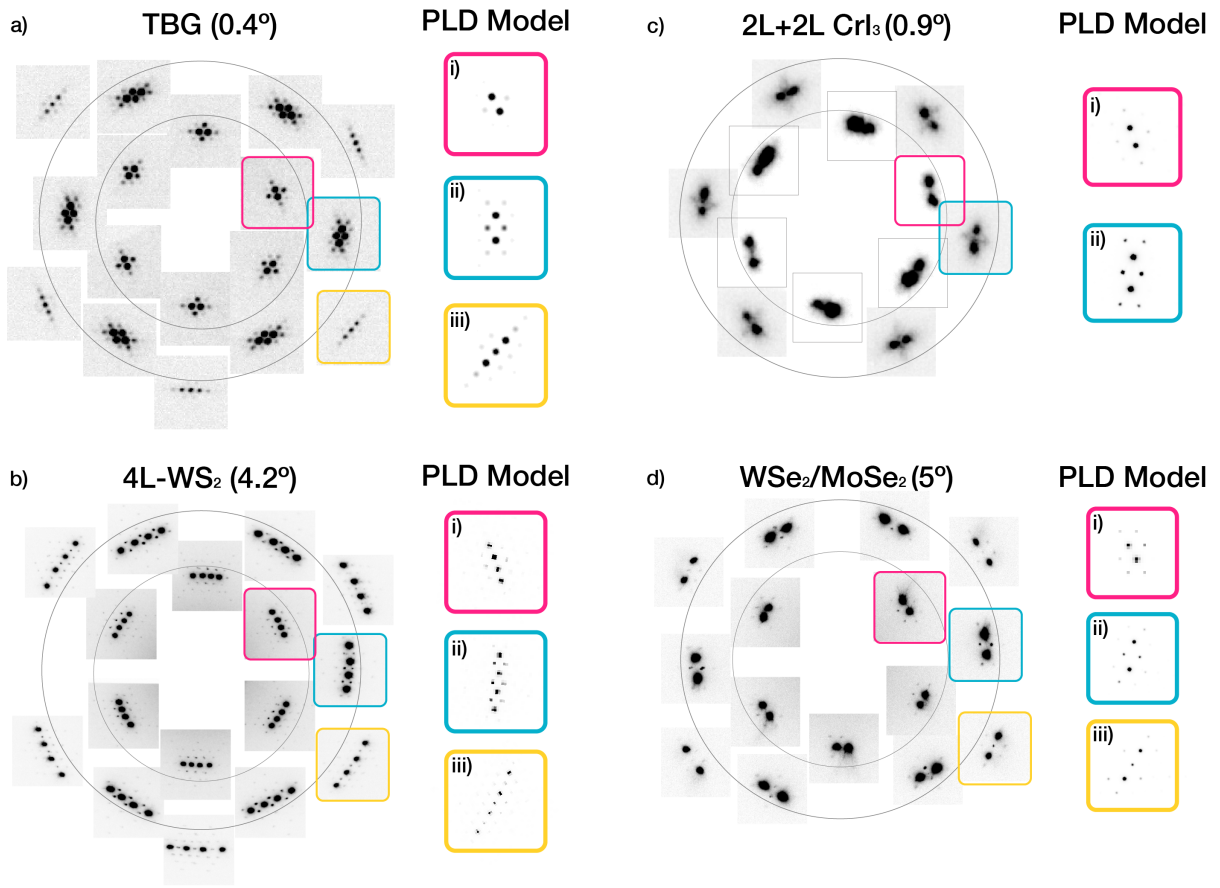

Figure III.10: Universal Torsional PLD Relaxation of Twisted 2D Materials Periodic relaxation is observed universally multiple twisted 2D systems. SAED of a) low-θ TBG, b) twisted four layer (4L) WS_2 homostructure c) twisted bilayer (2L + 2L) CrI_3 d) twisted $WSe_2/MoSe_2$ heterostructure shows bright Bragg peaks with small superlattice peaks. Insets i–iii are multislice simulated diffraction patterns with torsional PLD model. The torsional PLD model reproduces qualitatively accurate SAED patterns across multiple systems.

Torsional PLDs Across Many Twisted 2D Materials

Torsional PLDs in twisted 2D materials are a universal phenomenon and not limited to TBG [8–10, 28]. Figure III.10 shows SAED patterns that exhibit periodic relaxations of four distinct twisted 2D systems: a) low twist angle TBG, b) 4-layer of WS_2 (4L-WS_2), c) twisted double bilayer CrI_3 (2L+2L CrI_3), and d) twisted $WSe_2/MoSe_2$ heterostructure.

The relaxation behavior is present in layered transitional metal dichalcogendies (MX_2) and trihallides (MH_3). Figure III.10b shows the diffraction pattern of 4-layer homostructure of WS_2 with equal twist angles between layers. Surprisingly, a strong torsional PLD is observed, despite having a large twist angle ($\theta \approx 4^\circ$) [10]. For multi-layered system, relaxation may not be equivalent between layers. For 4L-WS_2, for example, the PLD amplitudes are strongest for the inner-most layers. Here equal and opposite PLDs of the inner

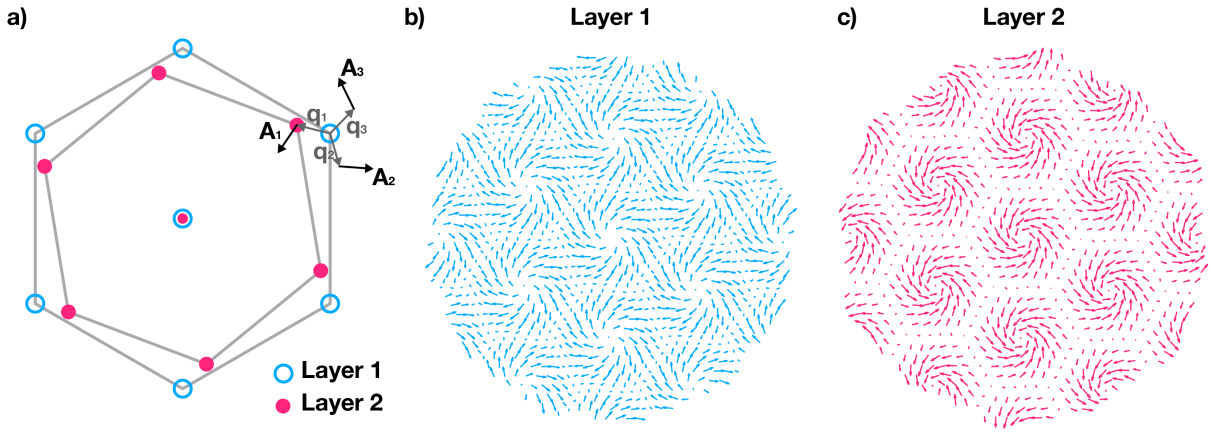

Figure III.11: Periodic relaxations in lattice mismatched twisted bilayer systems a) Schematic reciprocal lattice structure of twisted heterostructure of two lattice constant mismatched lattice. Layer 1 has smaller real space lattice constant. Vectors connecting first order Bragg peaks ($\mathbf{q}_{1,2,3}$) defines moiré unit cell and torsional PLD wavevectors. PLD displacement vectors ($\mathbf{A}_i$'s) are chosen to be non-orthogonal to $\mathbf{q}_i$'s. b, c) PLD displacement pattern with $\angle \mathbf{q}_i \mathbf{A}_i = 45°$. Layer 1 and 2 experiences expansion and compression of lattice, respectively, as well as torsional field.

two layers matches simulated diffraction patterns. (Fig. III.10b).

Figure III.10c shows 4-layers of twisted CrI_3, a magnetic 2D material, but with twist only between the middle two layers [9]. Xie et al. reported that this system shows magnetic behavior that cannot be explained by either 2-layer or 4-layer CrI_3 system and periodic relaxation must be accounted for to fully explain the materials properties. For 2L+2L CrI_3 system, the magnetic properties suggest that the outer layers distorted together with the inner layers (i.e. each bilayer acts like a monolayer). This is also consistent with diffraction simulations (Fig. III.10c).

Periodic reconstruction of twisted materials is not limited to homostructures. $WSe_2/MoSe_2$ heterostructures exhibit twist angle dependent excitonic behavior [29]. In Figure III.10d, we reveal that the heterostructure with $\theta \approx 5°$ periodically relaxes, despite having different lattice constants. A torsional PLD model is also applicable to such heterostructures. Simulated diffraction patterns (Fig. III.10d i–iii) show good agreement with the experimental diffraction pattern. It should be noted that the relaxation behavior of non-graphitic systems will be different when the stacking energy landscape is distinct [21]. Any stacking energy landscape can be accommodated by assigning the appropriate phase to each of the three PLD waves in a torsional PLD (Fig. III.2). Furthermore, due to lattice constant mismatch, reconstruction of heterobilayer involves compression and expansion of constituent layers [30, 31]. Compression/expansion of heterobilayer can be easily incorporated by including longitudinal components to $\hat{\mathbf{A}}_i$'s as demonstrated

in Figure III.11.

Discussion

Twisted 2D materials are complex moiré patterns where crystals deform according to a competition between intralayer elastic strain and interlayer van der Waals interactions. A reduction of symmetry arises not only from the global twist between layers but also the subsequent lattice restructuring. Thus, the twist-angle alone provides an incomplete description of the system. We show a torsional periodic lattice distortion is a precise order parameter to describe the atomic structure of twisted materials. Torsional periodic lattice distortions are comprised of three transverse PLDs that maximize the lower energy stacked domains and minimize and form solitonic shear boundaries in between. The amplitude and wavevector of torsional PLDs are defined by the twist angle and, in TBG, can be analytically and emperically predicted with picometer precision. In this sense, moiré materials are PLD engineering at low twist angles.

Despite the real-space complexity of low-twist moiré materials, the entire structure is sparsely described by a single value: the amplitude of the distortion wave. This choice of basis re-frames our understanding of low-twist angle materials. In the case of twisted bilayer graphene, the torsional PLD amplitude can be analytically calculated from the twist angle alone. Although the amplitude of the PLD can change gradually, the overall symmetry reduction occurs instantaneously—therefor a continuous phase transition is not expected. Although this work thoroughly describes TBG, it is extendable to a variety 2D materials and twist angles—each with a bespoke set of PLDs to match the interlayer energy landscapes.

References

[1] B. Sipos, A. F. Kusmartseva, A. Akrap, H. Berger, L. Forro, and E. Tutis, "From mott state to superconductivity in 1T-TaS_2", Nat. Mater. **7**, 960–965 (2008) 10.1038/nmat2318.

[2] N. F. Mott, "Metal-insulator transition", Rev. Mod. Phys. **40**, 677–683 (1968) 10 . 1103 / RevModPhys.40.677.

[3] J. Wilson, F. Di Salvo, and S. Mahajan, "Charge-density waves and superlattices in the metallic layered transition metal dichalcogenides", Adv. Phys. **24**, 117–201 (1975) 10 . 1080 / 00018737500101391.

[4]B. H. Savitzky, I. El Baggari, A. S. Admasu, J. Kim, S.-W. Cheong, R. Hovden, and L. F. Kourkoutis, "Bending and breaking of stripes in a charge ordered manganite", Nat. Commun. **8**, 1883 (2017) 10.1038/s41467-017-02156-1.

[5]R. Peierls, "Zur theorie der elektrischen und thermischen leitfähigkeit von metallen", Ann. Phys. **396**, 121–148 (1930) 10.1002/andp.19303960202.

[6]H. Yoo, K. Zhang, R. Engelke, P. Cazeaux, S. H. Sung, R. Hovden, A. W. Tsen, T. Taniguchi, K. Watanabe, G.-C. Yi, M. Kim, M. Luskin, E. B. Tadmor, and P. Kim, Nat. Mater. **18**, 448–453 (2019) 10.1038/s41563-019-0346-z.

[7]Y. Cao, V. Fatemi, S. Fang, K. Watanabe, T. Taniguchi, E. Kaxiras, and P. Jarillo-Herrero, "Unconventional superconductivity in magic-angle graphene superlattices", Nature **556**, 43 (2018) 10.1038/nature26160.

[8]A. Weston, Y. Zou, V. Enaldiev, A. Summerfield, N. Clark, V. Zólyomi, A. Graham, C. Yelgel, S. Magorrian, M. Zhou, J. Zultak, H. D., A. Barinov, T. H. Bointon, A. Kretinin, N. R. Wilson, P. H. Beton, V. I. Fal'ko, S. J. Haigh, and R. Gorbachev, "Atomic reconstruction in twisted bilayers of transition metal dichalcogenides", Nat. Nanotechnol. **15**, 592–597 (2020) 10.1038/s41565-020-0682-9.

[9]H. Xie, X. Luo, G. Ye, Z. Ye, H. Ge, S. H. Sung, E. Rennich, S. Yan, Y. Fu, T. S., H. Lei, R. Hovden, K. Sun, R. He, and L. Zhao, "Twist engineering of the two-dimensional magnetism in double bilayer chromium triiodide homostructures", Nat. Phys. **18**, 30–36 (2021) 10.1038/s41567-021-01408-8.

[10]A. J. Mannix, A. Ye, S. H. Sung, A. Ray, F. Mujid, C. Park, M. Lee, J.-H. Kang, R. Shreiner, H. A., D. A. Muller, R. Hovden, and J. Park, "Robotic four-dimensional pixel assembly of van der waals solids", Nat. Nanotechnol., 10.1038/s41565-021-01061-5 (2022) 10.1038/s41565-021-01061-5.

[11]W.-M. Zhao, L. Zhu, Z. Nie, Q.-Y. Li, Q.-W. Wang, L.-G. Dou, J.-G. Hu, L. Xian, S. Meng, and S.-C. Li, "Moiré enhanced charge density wave state in twisted 1t-tite$_2$/1t-tise$_2$ heterostructures", Nat. Mater, 10.1038/s41563-021-01167-0 (2021) 10.1038/s41563-021-01167-0.

[12]S. Carr, S. Fang, and E. Kaxiras, "Electronic-structure methods for twisted moiré layers", Nat. Rev. Mater. **5**, 748–763 (2020) 10.1038/s41578-020-0214-0.

[13]J. S. Alden, A. W. Tsen, P. Y. Huang, R. Hovden, L. Brown, J. Park, D. A. Muller, and P. L. McEuen, "Strain solitons and topological defects in bilayer graphene", Proc. Acad. Natl. Sci. **110**, 11256–11260 (2013) 10.1073/pnas.1309394110.

[14]E. Annevelink, H. T. Johnson, and E. Ertekin, "Topologically derived dislocation theory for twist and stretch moiré superlattices in bilayer graphene", Phys. Rev. B **102**, 184107 (2020) 10.1103/PhysRevB.102.184107.

[15]A. M. Popov, I. V. Lebedeva, A. A. Knizhnik, Y. E. Lozovik, and B. V. Potapkin, "Commensurate-incommensurate phase transition in bilayer graphene", Phys. Rev. B **84**, 045404 (2011) 10.1103/PhysRevB.84.045404.

[16]S. H. Sung, N. Schnitzer, L. Brown, J. Park, and R. Hovden, Phys. Rev. Mater. **3**, 064003 (2019) 10.1103/PhysRevMaterials.3.064003.

[17]L. Brown, R. Hovden, P. Huang, M. Wojcik, D. Muller, and J. Park, "Twinning and Twisting of Tri- and Bilayer Graphene", Nano Letters **140**, 1609 (2012).

[18]N. P. Kazmierczak, M. Van Winkle, C. Ophus, K. C. Bustillo, S. Carr, H. G. Brown, J. Ciston, T. Taniguchi, K. Watanabe, and D. K. Bediako, "Strain fields in twisted bilayer graphene", Nat. Mater., 956–963 (2021) 10.1038/s41563-021-00973-w.

[19]M. J. Zachman, J. Madsen, X. Zhang, P. M. Ajayan, T. Susi, and M. Chi, "Interferometric 4d-stem for lattice distortion and interlayer spacing measurements of bilayer and trilayer 2d materials", Small, 2100388.

[20]K. Zhang and E. B. Tadmor, "Structural and electron diffraction scaling of twisted graphene bilayers", J. Mech. Phys. Solids **112**, 225–238 (2018) 10.1016/j.jmps.2017.12.005.

[21]S. Carr, D. Massat, S. B. Torrisi, P. Cazeaux, M. Luskin, and E. Kaxiras, "Relaxation and domain formation in incommensurate two-dimensional heterostructures", Phys. Rev. B **98**, 224102 (2018) 10.1103/PhysRevB.98.224102.

[22]R. Hovden, A. W. Tsen, P. Liu, B. H. Savitzky, I. El Baggari, Y. Liu, W. Lu, Y. P. Sun, P. Kim, A. N. Pasupathy, and L. F. Kourkoutis, "Atomic lattice disorder in charge-density-wave phases of exfoliated dichalcogenides (1T-TaS_2)", Proc. Natl. Acad. Sci. **113**, 11420–11424 (2016) 10.1073/pnas.1606044113.

[23]H. Luo, J. Strychalska-Nowak, J. Li, J. Tao, T. Klimczuk, and R. J. Cava, "S-shaped suppression of the superconducting transition temperature in cu-intercalated $nbse_2$", Chem. Mater **29**, 3704–3712 (2017) 10.1021/acs.chemmater.7b00655.

[24]J. Lee, K. Prokeš, S. Park, I. Zaliznyak, S. Dissanayake, M. Matsuda, M. Frontzek, S. Stoupin, G. L. Chappell, R. E. Baumbach, C. Park, J. A. Mydosh, G. E. Granroth, and J. P. C. Ruff, "Charge density wave with anomalous temperature dependence in UPt_2Si_2", Phys. Rev. B **102**, 0411112(R) (2020) 10.1103/PhysRevB.102.041112.

[25]A. W. Overhauser, "Observability of charge-density waves by neutron diffraction", Phys. Rev. B **3**, 3173–3182 (1971) 10.1103/physrevb.3.3173.

[26]P. Bak, "Commensurate phases, incommensurate phases and the devil's staircase", Rep. Prog. Phys **45**, 587–629 (1982) 10.1088/0034-4885/45/6/001.

[27]A. N. Kolmogorov and V. H. Crespi, "Registry-dependent interlayer potential for graphitic systems", Phys. Rev. B **71**, 235415 (2005) 10.1103/PhysRevB.71.235415.

[28]K. Yasuda, X. Wang, K. Watanabe, T. Taniguchi, and P. Jarillo-Herrero, "Stacking-engineered ferroelectricity in bilayer boron nitride", Science **372**, 1458–1462 (2021) 10.1126/science.abd3230.

[29]L. Zhang, Z. Zhang, F. Wu, D. Wang, R. Gogna, S. Hou, K. Watanabe, T. Taniguchi, K. Kulkarni, T. Kuo, S. R. Forrest, and H. Deng, "Twist-angle dependence of moirè excitons in $ws_2/mose_2$ heterobilayers", Nat. Commun. **11**, 5888 (2020) 10.1038/s41467-020-19466-6.

[30]H. Li, S. Li, M. H. Naik, J. Xie, X. Li, J. Wang, E. Regan, D. Wang, W. Zhao, S. Zhao, S. Kahn, K. Yumigeta, M. Blei, T. Taniguchi, K. Watanabe, S. Tongay, A. Zettl, S. G. Louie, F. Wang, and M. F. Crommie, "Imaging moiré flat bands in three-dimensional reconstructed wse_2/ws_2 superlattices", Nat. Mater. **20**, 945–950 (2021) 10.1038/s41563-021-00923-6.

[31]C. R. Woods, L. Britnell, A. Eckmann, R. S. Ma, J. C. Lu, H. M. Guo, X. Lin, G. L. Yu, Y. Cao, R. V. Gorbachev, A. V. Kretinin, J. Park, L. A. Ponomarenko, M. I. Katsnelson, Y. N. Gornostyrev, K. Watanabe, T. Taniguchi, C. Casiraghi, H.-J. Gao, A. K. Geim, and K. S. Novoselov, Nat. Phys. **10**, 451–456 (2014) 10.1038/nphys2954.

Chapter IV

Two-dimensional Charge Order Stabilized in Clean Polytype Heterostructures

Introduction

Charge density waves (CDW) are an emergent periodic modulation of the electron density that permeates a crystal with strong electron-lattice coupling [1–4]. TaS_2 and TaS_xSe_{2-x} host several CDWs that spontaneously break crystal symmetries, mediate metal–insulator transitions, and compete with superconductivity [1, 5–7]. These quantum states are promising candidates for novel devices [8–11], efficient ultrafast non-volatile switching [12, 13], and suggest elusive chiral superconductivity [14, 15]. Law & Lee recently called for pristine 2D CDW syntheses to access exotic spin-liquid states in 1T-TaS_2 [16]. Unfortunately, extrinsic and thermal disorder in free standing 2D layers degrades correlation-driven quantum behavior [17, 18] and clean 2D charge density waves or superconductivity are near absent [19]. Room temperature access to spatially coherent charge density waves (e.g. commensurate states) and clean 2D confinement could enable a paradigm shift toward device logic and quantum computing.

Here we show the critical temperature for spatially-coherent, commensurate charge density waves (C-CDW) in 1T-TaS_2 can be raised to well above room temperature ($\sim$150 K above the expected transition) by synthesizing clean (minimal impurities or defects) interleaved 2D polytypic heterostructures. This stabilizes a collective insulating ground state (i.e. C-CDW) not expected to exist at room temperature. We show the formation of these spatially coherent states occurs when 2D CDWs are confined between metallic prismatic polytypes. Metallic layers screen impurity potentials to suppress the nearly-commensurate (NC-CDW) phase. At the same time, interleaving disables interlayer coupling between CDWs to ensure an unpaired electron in each 2D supercell. This raises the

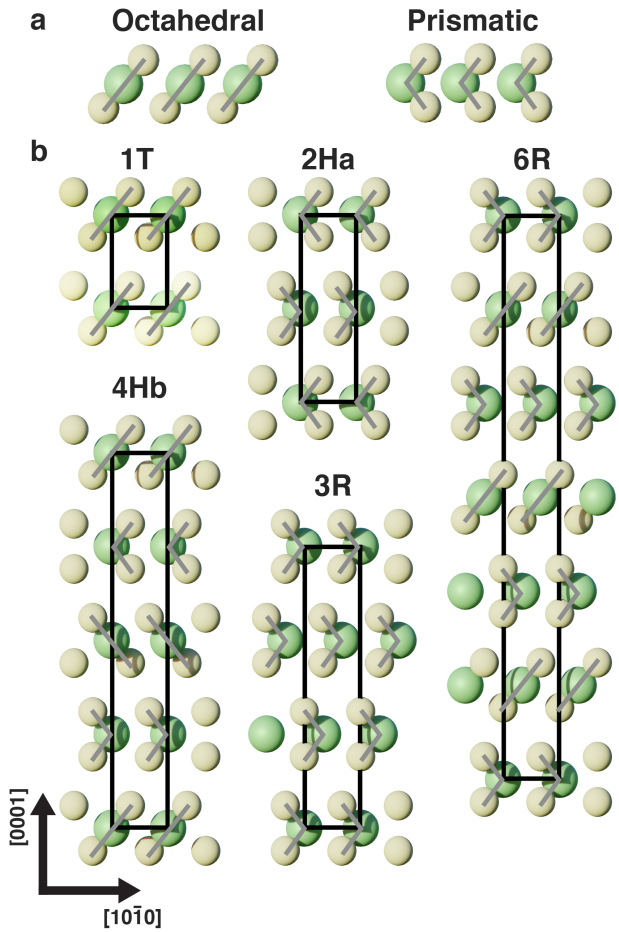

Figure IV.1: Unit cells of previously synthesized TaS_2 polytypes a) Intralayer Ta–S coordination for octahedral (left) and prismatic (right) coordination. Gray lines indicates Ta–S bonds. b) Unit cells of TaS_2 polytypes 1T, 2Ha, 3R, 4Hb and 6R along $\langle 11\bar{2}0 \rangle$ [1, 20–22]. Oc layers comprise 1T in bulk, Pr layers comprise 2Ha and 3R, and 4Hb and 6R contain alternating Oc–Pr stacking.

critical temperature of the C-CDW and forms out-of-plane twinned commensurate (tC) CDWs as revealed by scanned nanobeam electron diffraction. These results demonstrate polytype engineering as a route to isolating 2D collective quantum states in a well-defined extrinsic environment with identical chemistry but distinct band structure.

Layered TaS_2 polytypes (Fig. IV.1) are archetypal hosts to anomalous electronic properties associated with the formation of CDWs. The Ta coordination to six chalcogens dramatically changes its behavior. Prismatic coordination (Pr) found in the stable 2H polytype is metallic, even below the CDW onset around 90 K, and becomes superconducting around 0.5 K (enhanced to 2.2 K when thinned [5]). Octahedral (Oc) coordination found in the metastable 1T polytype has inversion symmetry and exhibits three distinct, salient CDW phases: commensurate (C), nearly-commensurate (NC), and incommensurate (IC). An intermediate triclinic phase has also been reported [23–25]. At room temperature,

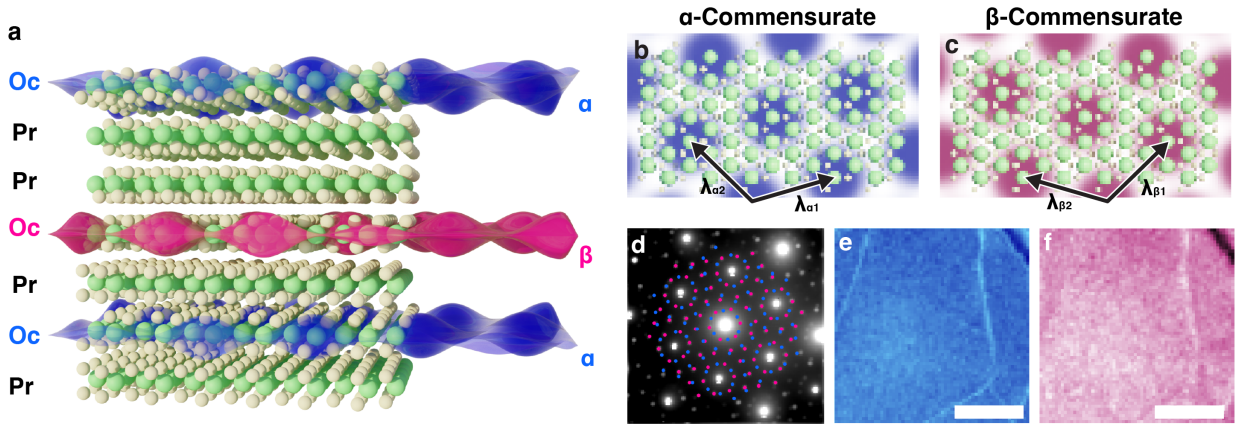

Figure IV.2: Twinned, commensurate CDW at room temperature in ultrathin TaS_2 a) Schematic illustration of room-temperature, out-of-plane twinned, commensurate CDW in 1T-TaS_2. Blue and red overlays represent CDW twins within octahedrally coordinated TaS_2. Metallic prismatic polytypes isolate octahedral layers to stabilize tC-CDWs. b, c) Twin superlattice structure illustrated for α and β C-CDW, respectively. d) Average diffraction pattern of twinned, C-CDW state over $(870\ \text{nm})^2$ field-of-view reveals two sets of superlattice peaks (marked with blue and red). e, f) Nanobeam diffraction imaging from each set of superlattice peaks maps the coexistence of both CDW twins—expected for twinning out-of-plane. Scale bar is 300 nm.

the conductive NC-CDW is generally accepted as a C-CDW with short range order [26–30] that permits electron transport along regions of discommensuration [31–33]. Below $\sim$200 K, the CDW wave vector locks into $\sim 13.9°$ away from the reciprocal lattice vector (Γ–M) to become a C-CDW that achieves long-range order with a $\sqrt{13} \times \sqrt{13}$ supercell [1, 34]. This reduction of crystal symmetry gaps the Fermi-surface and the commensurate phase becomes Mott insulating [1, 35, 36]. Above 352 K, the CDW wave vector aligns along the reciprocal lattice vector and becomes the disordered IC-CDW phase.

Twinned Commensurate Charge Density Waves

The tC-CDW phase reported herein has distinct out-of-plane charge order—illustrated in Figure IV.2a (See also: Fig. S1). 2D CDWs reside within Oc-layers sparsely interleaved between metallic Pr-layers. Each CDW is commensurate in one of two degenerate twin states, α-C (blue) or β -C (red) (Fig. IV.2b, c). The translational symmetry is described by in-plane CDW lattice vectors $(\boldsymbol{\lambda}_{\alpha 1}, \boldsymbol{\lambda}_{\alpha 2})$ and $(\boldsymbol{\lambda}_{\beta 1}, \boldsymbol{\lambda}_{\beta 2})$. CDWs are a prototypical manifestation of electron-lattice coupling, in which both the electron density and lattice positions undergo periodic modulations to reduce crystal symmetry and lower the electronic energy [37]. The associated periodic lattice distortions (PLD) diffract incident swift electrons into low-intensity superlattice peaks between Bragg peaks [38, 39]. Polytypes and stacking order thereof manifests as changes in Bragg peak intensities where as CDWs produce distinct superlattice peaks [28, 38, 40]. Figure IV.2d shows the position averaged

convergent beam electron diffraction pattern (0.55 mrad semi-convergence angle, 80 keV) of the tC-CDW phase at room temperature with α, β superlattice peaks annotated (blue, red). Regularly spaced superlattice peaks and bright first order superlattice peaks are characteristic of C-CDWs and match the tC-CDW peaks.

Both α and β CDW states were mapped over microns of area to reveal a uniform coexistence of both twins when viewed in projection out-of-plane (Fig. IV.2e, f). This is evidently different from recently reported in-plane twin CDWs created by femtosecond light pulses [41]. Mapping CDW structure required a electron microscope pixel array detector (EMPAD) with 1,000,000:1 dynamic range [42] allowing Bragg beams to be imaged while still maintaining single electron sensitivity near CDW peaks. A convergent beam electron diffraction (CBED; 0.55 mrad convergence semi-angle, 200 keV) pattern was collected at every beam position across large fields of view—an emerging technique often called 4D-STEM. [42–44]. For 4D-STEM, a CBED pattern was recorded at each beam position using the EMPAD detector. EMPAD's high dynamic range (1,000,000:1) and single electron sensitivity [42] allows simultaneous recording of intense Bragg beams alongside weak superlattice reflections. Virtual satellite dark field images were formed by integrating intensities from all satellite peaks at each scan position. In this way, the local CDW structure was measured at $\sim$4.6 nm resolution and across >1 μm fields of view. It demonstrates 4D-STEM as an invaluable tool for mapping charge order in materials. Previous approaches to mapping CDWs entailed sparse measurement from a handful of diffraction patterns [41], small-area tracking of atomic displacements [45], or traditional dark-field TEM techniques that result in low resolution and debilitating signal-to-noise ratios [1, 46].

Clean Polytype Heterostructures

Thermal treatment reproducibly forms the tC-CDW phase—a process summarized by the in-situ selected area electron diffraction (SAED) in Figure IV.3a. Initially, an exfoliated flake of 1T-TaS_2 hosts NC-CDWs (Fig. IV.3a, left) at room temperature with diffuse first-order superlattice peaks (cyan circles) and sharp second order superlattice peaks (cyan triangle). 1T-TaS_2 is heated past the reversible phase transition ($T_{NC\text{-}IC} \approx 352$ K) into the disordered IC-CDW state, which has characteristic azimuthally diffuse superlattice spots (Fig. IV.3a, right). Heating continues up to temperatures ($\sim$720 K) above the polytype transition ($T_{Oc\text{-}Pr} \approx 600$ K [47]) where it remains for several minutes. Upon cooling, the system does not return to the expected NC-CDW but instead enters a tC-CDW state with sharp, commensurate first and second order superlattice peaks duplicated with mirror symmetry (α, β) (Fig. IV.3a, bottom). The tC-CDW phase is stable and observable after

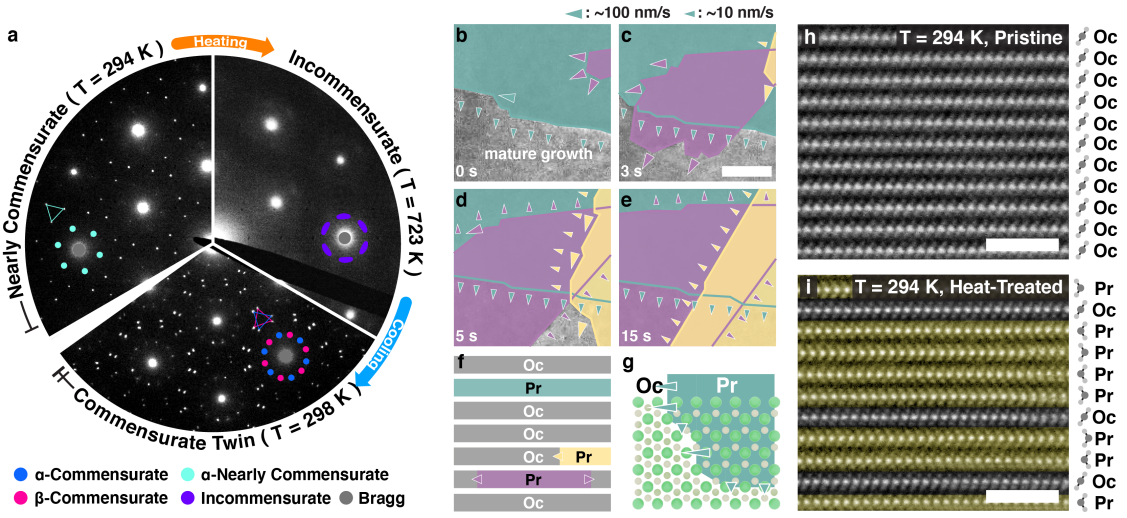

Figure IV.3: Polytype isolation forms 2D CDW layers a) Pristine 1T-TaS_2 at room temperature hosts NC-CDW (left). Upon heating the NC phase gives way to IC-CDW (right) at ~350 K; the transition is normally reversible. Strikingly, heating above ~620 K then cooling stabilizes tC-CDW (bottom). SAED patterns were formed from a 500 nm aperture b–e) In-situ TEM reveals layer-by-layer octahedral to prismatic polytypic transformations during heat treatment. Multiple polytypic domains (denoted green, purple, and yellow) nucleate and grow simultaneously without interaction. Scale bar is 350 nm. f) Schematic cross-section of TaS_2 during layer-by-layer polytypic transition. g) Fast and slow transitions occur along $\langle 10\bar{1}0 \rangle$ and $\langle 11\bar{2}0 \rangle$ directions respectively. h–i) Atomic resolution cross-sectional HAADF-STEM of h) pristine and i) heat-treated TaS_xSe_{2-x} confirms polytypic transformation. After treatment, prismatic (Pr) layers encapsulate monolayers of octahedral (Oc) layers. Scale bar is 2 nm. A selenium doped sample was imaged to enhance chalcogen visibility.

months of dry storage (RH ~10 %) at room temperature. Synthesis was replicated ex-situ in both high-vacuum ($< 10^{-7}$ Torr) and inert argon purged gloveboxes, but amorphized in ambient air. The tC-CDW was equivalently synthesized for both TaS_2 and TaS_xSe_{2-x}.

Heating above the polytype transition temperature ($T_{Oc\text{-}Pr}$) provokes layer-by-layer transitions from Oc to Pr polytypes instead of a rapid bulk transformation. Figure IV.3b–e shows in-situ TEM using high-frame-rate (25 fps) microscopy taken at ~710 K. Each colored overlay highlights the growth and formation of a new prismatic polytype domain. Arrows indicate movement of Oc/Pr coordination boundary with a fast-transition up to ~100 nm/s along $\langle 10\bar{1}0 \rangle$ crystal directions and a slow-transition at ~10 nm/s along $\langle 11\bar{2}0 \rangle$ (Fig. IV.3g).. Domains nucleate and boundaries progress independently between layers as illustrated in Figure IV.3b–f. Cooling the sample mid-transition produces a sparsely interleaved polytypic heterostructure.

Atomic resolution cross-section images of pristine and heat-treated samples (Fig. IV.3h and i, respectively) measured by high-angle annular dark-field (HAADF)-STEM reveal the interleaved polytypic heterostructure. Interleaving isolates monolayers of octahedral (Oc) coordination that host 2D-CDWs in a clean, defect-free environment of prismatic

(Pr) metallic layers. Although this system is best described as a sparse interleaving of Oc-layers within many Pr-layers (Fig. IV.3i), the uncorrelated polytype stacking may permit by chance a small (or even negligible) amount of layers which locally match a 4Hb (or another bulk polytype) unit cell.

The metallic 'Pr' layers are hypothesized to screen out-of-plane interactions and impurity potentials to stabilize low-temperature commensurate CDWs at room temperature. As a result, the NC-CDW state no longer exists and a long-range ordered tC-CDW emerges as a stable phase up to $\sim$350 K. This result is radically different from previous reports where free standing ultra-thin 1T-TaS_2 degrades long-range order [48] and broadens the NC-CDW phase by lowering T_{CCDW} [13, 18, 49]. However, our observation of 2D commensurate CDWs agrees with a theoretical prediction that commensurate CDWs are more stable in clean monolayer [50].

Understanding the role of disorder requires decoupling intrinsic quantum behavior from extrinsic influences at the surfaces, especially in low dimensions where long-range order becomes more fragile and vulnerable to impurities [17, 51, 52]. When the disorder strength reaches a certain threshold, the long-range C-CDW phase gives its way to a disordered phase [17]. Here, each 2D 1T-TaS_2 CDW is in its native chemical, endotaxial, and unstrained environment. Impurity potentials that pin CDWs [53] and break spatial coherence are mitigated by adjacent metallic Pr-layers. For C-CDWs (in 2D and above) in the presence of sufficiently weak disorder, the charge order remains stable [52]. Additionally, isolating monolayers of 1T-TaS_2 ensures an odd number of electrons per unit cell and elongates the Fermi surface out-of-plane—both expected to reduce the electronic energy.

Isolation of 2D Charge Density Waves

In the tC-CDW, metallic Pr-layers decouple interlayer CDW interactions to create isolated 2D CDWs with twin degeneracy. Using a phenomenological model we illustrate a kinetic pathway for accessing the tC-CDW. Here, local orientation of the CDW wave vector, θ, is an apt order parameter for describing the breaking of the mirror symmetry in the C$\rightleftharpoons$IC transition. This provides a simple, minimal phenomenological model to qualitatively capture the formation of twinned CDWs but does not model all remaining components of the complete CDW order parameter (See Appendix C.1). A free energy expansion of this order parameter combined with an XY interaction of the CDW wave vector qualitatively reproduces diffraction patterns for IC-CDW and α/β C-CDW. In diffraction, the

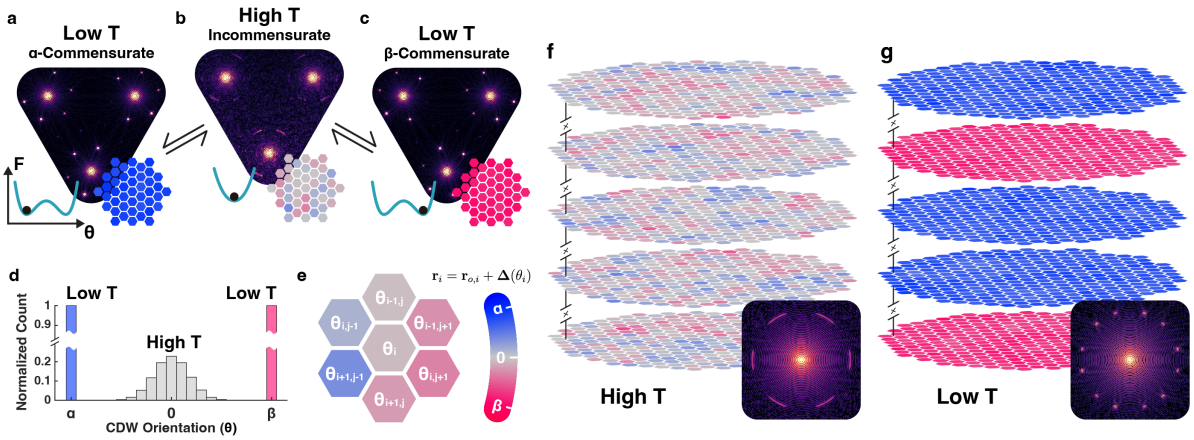

Figure IV.4: Phenomenological model illustrates formation of commensurate CDWs with out-of-plane twin degeneracy a–c) The CDW wave-vector direction θ defines an order parameter with degenerate commensurate twins when cooled from IC-CDW phase. Simulated far-field diffraction patterns for a) α-C, b) IC and c) β-C. The free energy (F) landscape (Inset-left) governs the mean θ and the real-space distribution (Inset-right). d) Histogram of θ shows zero-centered, wide distribution at high temperature. At low temperature, the distribution is narrow and centered at $\pm 13.9°$ for either twin. e) Map of local orientation of wave vector (θ) at IC phase. Each hexagonal cell represents θ at each Ta site. f) At high temperature θ is mean centered and disordered, however, g) at low-temperature each 2D layer converges into either α or β randomly when layers are decoupled. Simulated far-field diffraction patterns of multi-layer system in high temperature (Inset-f) and low temperature (Inset-g) resembles experimentally observed SAEDs.

superlattice peak location and shape encodes the distribution of the CDW order parameter. Simulated diffraction patterns at high temperatures feature first-order superlattice peaks azimuthally broadened by CDW disorder and centered along the reciprocal lattice (Γ–M) direction (Fig. IV.4b). At low temperature, the superlattice peaks are sharpened by long-range CDW order and located at $+13.9°$ or $-13.9°$ away from Γ–M (Fig. IV.4a,c). Figure IV.4d shows distribution of θ at high (gray) and low (blue, red) temperatures.

When cooled, the system chooses α or β with equal probability. For pristine 1T-TaS_2, CDWs couple between layers, twin degeneracy is broken, and no twinning occurs [54]. However, in the absence of interlayer interaction or extrinsic perturbation, each 2D CDW layer quenches randomly into either α or β C-CDW (Fig. IV.4g) from the high-temperature IC-CDW phase (Fig. IV.4f)—forming the out-of-plane twinned tC-CDW phase. In projection, the model produces diffraction pattern that resembles experimental SAED of IC-CDW and tC-CDW phases. (Fig. IV.4f,g Insets) In systems with very few CDW layers, one stronger CDW direction can sometimes emerge (Fig. S12b, c). From our model, out-of-plane twinning occurs for modest cooling rates but we note fast quenching predicts in-plane twinning similar to reported ultrafast optical excitations [41].

Optical and Electrical Characteristics of tC-CDW

Rotational-anisotropy second-harmonic generation (RA-SHG) revealed restoration of twin degeneracy in heat-treated samples. The RA-SHG of pristine sample (Fig. IV.5b) exhibits a hallmark of the RA-SHG pattern rotated away from the lattice vectors; breaking mirror symmetry due to formation of a single-domain NC-CDW. In contrast, the heat-treated sample's RA-SHG pattern (Fig. IV.5c) is mirror-symmetric to the crystalline directions and much stronger. Together, this is a strong evidence of equally weighted degenerate α and β states (i.e., tC-CDW) and the emergence of Pr-layers that are mirror symmetric and non-centrosymmetric.

Electronic measurement of the polytypic heterostructure with interleaved CDWs reveals a direct tC$\leftrightharpoons$IC transition at 350 K and removal of the disordered NC-CDW phase. Figure IV.5a shows in-plane resistance vs. temperature measurements of pristine 1T (pink) and heat-treated polytypic heterostructure (blue) are drastically different. The heterostructure features only one metal–insulator transition at 350 K, whereas pristine 1T-TaS_2 exhibits two transitions at $\sim$200 K (C$\leftrightharpoons$NC) and 350 K (NC$\leftrightharpoons$IC). Resistance jumps are a signature of emergent CDW order. At low temperature the metallic Pr-layers dominate in-plane conduction since the resistance is expected to monotonically decrease as observed in bulk material [55]. This hinders the quantification of resistance in individual Oc-layers, however the critical temperatures remain clearly visible.

Repeated in-situ heating–cooling cycles reveal the tC$\leftrightharpoons$IC transition is reversible and the NC-CDW phase is removed. Note that the intermediate triclinic phase was also not observed. Electronic measurements (Fig. IV.5a) match structure measurements from in-situ SAED (Fig. IV.3a) and confirm the insulating commensurate charge order of the tC-CDW phase. The interleaved polytype herein stabilizes coherent electronic states well above ($\sim$150 K) the normal critical temperature, and disordered NC-CDW phase is structurally and electronically removed.

Discussion

In summary, we have established a pathway toward stabilizing latent CDWs with long-range order at room temperature by reducing their dimensions to 2D using clean interleaved polytypes of TaS_2. The metallic layers isolate each 2D CDW to restore twin degeneracy giving rise to an out-of-plane twinned commensurate CDW phase. 4D-STEM proved invaluable for mapping CDW domains across large fields-of-view ($\sim$1 μm) to con-

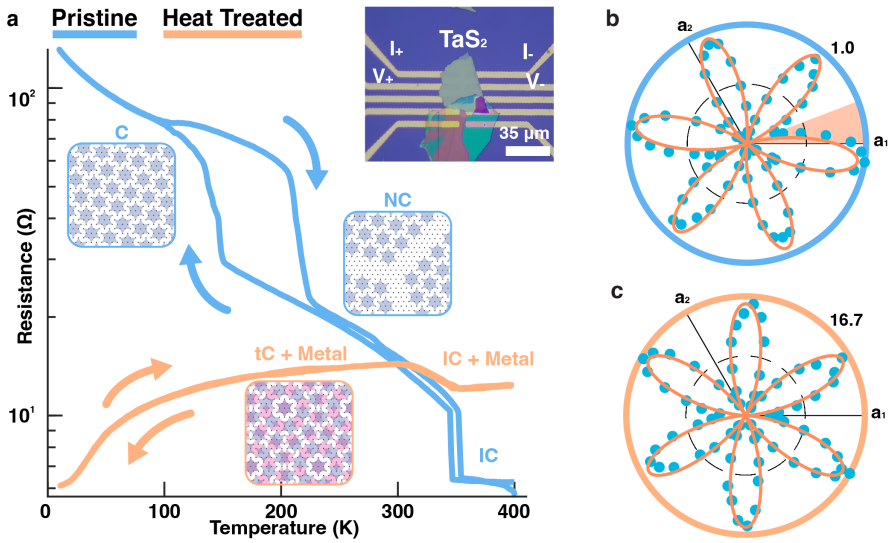

Figure IV.5: Electronic transport of tC-CDW phase transition and reversibility a) 4-point in-plane resistance measurement as function of temperature for pristine bulk (pink) and heat-treated (blue) TaS_2. Pristine samples show two jumps in resistance for C⇋NC and NC⇋IC, whereas the heat treated polytypic heterostructures only feature a single, reversible tC⇋IC transition at ∼350 K corresponding to the enhanced critical temperature for CDW commensuration and disappearance of the NC-CDW. Metallic Pr-layers dominate the overall trend of the resistance measurement, however, the single jump above room-temperature is a distinct feature of the tC-CDW. Schematics represent a simplified CDW structures of each phase. Inset) Optical image of the nanofabricated device. b) The RA-SHG pattern for pristine 1T samples display a mismatch between the nominal mirror direction and the crystalline direction, indicating the CDW breaks mirror symmetry. c) After heat treatment, the RA-SHG pattern is symmetric with respect to the crystal, implying equal weights between the α and β states. The SHG intensity also increases with mirror symmetric Pr-layers present.

firm twin structure while atomic resolution HAADF-STEM revealed the 2D CDW layers within a metallic phase. Both structural and electronic investigations show the disordered NC-CDW phase disappears when a 2D CDW is in a chemically and endotaxially native clean environment. The stabilization of ordered electronic phases with 2D polytype engineering has significant implications for new routes to access fragile, exotic correlated electron states.

References

[1]J. Wilson, F. Di Salvo, and S. Mahajan, "Charge-density waves and superlattices in the metallic layered transition metal dichalcogenides", Adv. Phys. **24**, 117–201 (1975) 10 . 1080 / 00018737500101391.

[2]S.-K. Chan and V. Heine, "Spin density wave and soft phonon mode from nesting fermi surfaces", J. Phys. F: Met. Phys. **3**, 795–809 (1973) 10.1088/0305-4608/3/4/022.

[3]S. Hellmann, T. Rohwer, M. Kallane, K. Hanff, C. Sohrt, A. Stange, A. Carr, M. M. Murnane, L. Kapteyn, L. Kipp, M. Bauer, and K. Rossnagel, "Time-domain classification of charge-density-wave insulators", Nat. Commun. **3**, 1069 (2012) 10.1038/ncomms2078.

[4]T. Pillo, J. Hayoz, H. Berger, R. Fasel, L. Schlapbach, and P. Aebi, "Interplay between electron-electron interaction and electron-phonon coupling near the fermi surface of 1t-tas$_2$", Phys. Rev. B **62**, 4277 (2000) 10.1103/PhysRevB.62.4277.

[5]E. Navarro-Moratalla, J. O. Island, S. Mañas-Valero, E. Pinilla-Cienfuegos, A. Castellanos-Gomez, J. Quereda, G. Rubio-Bollinger, L. Chirolli, J. A. Silva-Guillén, N. Agraït, G. A. Steele, F. Guinea, H. S. J. van der Zant, and E. Coronado, "Enhanced superconductivity in atomically thin TaS_2", Nat. Commun. **7**, 11043 (2016) 10.1038/ncomms11043.

[6]R. Ang, Z. C. Wang, C. L. Chen, J. Tang, Y. Liu, W. J. Lu, Y. P. Sun, T. Mori, and Y. Ikuhara, "Atomistic origin of an ordered superstructure induced superconductivity in layered chalcogenides", Nat. Commun. **6**, 6091 (2015) 10.1038/ncomms7091.

[7]L. Li, X. Deng, Z. Wang, Y. Liu, M. Abeykoon, E. Dooryhee, A. Tomic, Y. Huang, J. B. Warren, E. S. Bozin, S. J. L. Billinge, Y. P. Sun, Y. Zhu, G. Kotliar, and C. Petrovic, "Superconducting order from disorder in 2H-$TaSe_{2-x}S_x$", npj Quantum Mater. **2**, 11 (2017) 10.1038/s41535-017-0016-9.

[8]D. N. Basov, R. D. Averitt, and D. Hsieh, "Towards properties on demand in quantum materials", Nat. Mater. **16**, 1077–1088 (2017) 10.1038/nmat5017.

[9]Y. Tokura, M. Kawasaki, and N. Nagaosa, "Emergent functions of quantum materials", Nat. Phys **13**, 1056–1068 (2017) 10.1038/nphys4274.

[10]M. J. Hollander, Y. Liu, W.-J. Lu, L.-J. Li, Y. P. Sun, J. A. Robinson, and S. Datta, "Electrically Driven Reversible Insulator–Metal Phase Transition in 1T-TaS_2", Nano Lett. **15**, 1861–1866 (2015) 10.1021/nl504662b.

[11]G. Liu, B. Debnath, T. R. Pope, T. T. Salguero, R. K. Lake, and A. A. Balandin, "A charge-density-wave oscillator based on an integrated tantalum disulfide–boron nitride–graphene device operating at room temperature", Nat. Nanotechnol. **11**, 845–850 (2016) 10.1038/nnano.2016.108.

[12]I. Vaskivskyi, I. A. Mihailovic, S. Brazovskii, J. Gospodaric, T. Mertelj, D. Svetin, P. Sutar, and D. Mihailovic, "Fast electronic resistance switching involving hidden charge density wave states", Nat. Commun. **7**, 11442 (2016) 10.1038/ncomms11442.

[13]A. W. Tsen, R. Hovden, D. Wang, Y. D. Kim, J. Okamoto, K. A. Spoth, Y. Liu, W. Lu, Y. P. Sun, J. C. Hone, L. F. Kourkoutis, P. Kim, and A. N. Pasupathy, "Structure and control of charge density waves in two-dimensional 1T-TaS_2", Proc. Natl. Acad. Sci. **112**, 15054–15059 (2015) 10.1073/pnas.1512092112.

[14]A. Ribak, M. R. Skiff, M. Mograbi, P. K. Rout, M. H. Fishcer, J. Ruhman, K. Chashka, Y. Dagan, and A. Kanigel, "Chiral superconductivity in the alternate stacking compound 4Hb-TaS_2", Sci. Adv. **6**, eaax9480 (2020) 10.1126/sciadv.aax9480.

[15]R. Ganesh, G. Baskaran, J. van den Brink, and D. V. Efremov, "Theoretical prediction of a time-reversal broken chiral superconducting phase driven by electronic correlations in a single $TiSe_2$ layer", Phys. Rev. Lett. **113**, 177001 (2014) 10.1103/PhysRevLett.113.177001.

[16]K. Law and P. Lee, "1T-TaS_2 as a quantum spin liquid", Proc. Natl. Acad. Sci. **114**, 6996–7000 (2017) 10.1073/pnas.1706769114.

[17]L. Nie, G. Tarjus, and S. A. Kivelson, "Quenched disorder and vestigial nematicity in the pseudogap regime of the cuprates", Proc. Natl. Acad. Sci. **111**, 7980–7985 (2014) 10.1073/pnas.1406019111.

[18]Y. Yu, F. Yang, X. F. Lu, Y. J. Yan, Y.-H. Cho, L. Ma, X. Niu, S. Kim, Y.-W. Son, D. Feng, S. Li, S.-W. Cheong, X. H. Chen, and Y. Zheng, "Gate-tunable phase transitions in thin flakes of 1T-TaS_2", Nat. Nanotechnol. **10**, 270–276 (2015) 10.1038/nnano.2014.323.

[19]A. Devarakonda, H. Inoue, S. Fang, C. Ozsoy-Kesinbora, M. Kriener, L. Fu, E. Kaxiras, D. Bell, and J. Checkelsky, "Clean 2D superconductivity in a bulk van der waals superlattice", Science **370**, 231–236 (2020) 10.1126/science.aaz6643.

[20]F. Jellinek, "The system of Tantalum-Sulfur", J. Less Common Met. **4**, 9–15 (1962) 10.1016/0022-5088(62)90053-X.

[21]F. J. Di Salov, B. G. Bagley, J. M. Voorhoeve, and J. V. Waszczak, "Preparation and properties of a new polytype of tantalum disulfide (4Hb-TaS_2)", J. Phys. Chem. Solids **34**, 1357–1362 (1973) 10.1016/S0022-3697(73)80034-4.

[22]A. H. Thompson, "The synthesis and properties of 6R-TaS_2", Solid State Commun **17**, 1115–1117 (1975) 10.1016/0038-1098(75)90267-7.

[23]S. Tanda and T. Sambongi, "X-ray study of the new charge-density-wave phase in 1t-tas_2", Synth. Met. **11**, 85–100 (1985) 10.1016/0379-6779(85)90177-8.

[24]K. Nakatsugawa, S. Tanda, and T. N. Ikeda, "Multivalley free energy landscape and the origin of stripe and quasi-stripe cdw structures in monolayer MX_2 compounds", Sci. Rep. **10**, 1239 (2020) 10.1038/s41598-020-58013-7.

[25]W. Wang, D. Dietzel, and A. Schirmeisen, "Lattice discontinuities of 1t-tas_2 across first order charge density wave phase transitions", Sci. Rep. **9**, 7066 (2019) 10.1038/s41598-019-43307-2.

[26]R. V. Coleman, B. Giambattista, P. K. Hansma, A. Johnson, W. W. McNairy, and C. G. Slough, "Scanning tunnelling microscopy of charge-density waves in transition metal chalcogenides", Adv. Phys, **37**, 559–644 (1988) 10.1080/00018738800101439.

[27]X. L. Wu and C. M. Lieber, "Hexagonal domain-like charge density wave phase of TaS_2 determined by scanning tunneling microscopy", Science **243**, 1703–1705 (1989) 10.1126/science.243.4899.1703.

[28]R. Hovden, A. W. Tsen, P. Liu, B. H. Savitzky, I. El Baggari, Y. Liu, W. Lu, Y. P. Sun, P. Kim, A. N. Pasupathy, and L. F. Kourkoutis, "Atomic lattice disorder in charge-density-wave phases of exfoliated dichalcogenides (1T-TaS_2)", Proc. Natl. Acad. Sci. **113**, 11420–11424 (2016) 10.1073/pnas.1606044113.

[29]Y. A. Gerasimenko, P. Karpov, I. Vaskivskyi, S. Brazovskii, and D. Mihailovic, "Intertwined chiral charge orders and topological stabilization of the light-induced state of a prototypical transition metal dichalcogenide", npj Quantum Mater. **4**, 32 (2019) 10.1038/s41535-019-0172-1.

[30]S. Vogelgesang, G. Storeck, J. G. Horstmann, T. Diekmann, M. Sivis, S. Schramm, K. Rossnagel, S. Schäfer, and C. Ropers1, "Phase ordering of charge density waves traced by ultrafast low-energy electron diffraction", Nat. Phys. **14**, 184–190 (2017) 10.1038/nphys4309.

[31]D. Cho, S. Cheon, K.-S. Kim, S.-h. Lee, Y.-H. Cho, S.-W. Cheong, and H. W. Yom, "Nanoscale manipulation of the mott insulating state coupled to charge order in 1T-TaS_2", Nat. Commun. **7**, 10453 (2016) 10.1038/ncomms10453.

[32]B. Sipos, A. F. Kusmartseva, A. Akrap, H. Berger, L. Forro, and E. Tutis, "From mott state to superconductivity in 1T-TaS_2", Nat. Mater. **7**, 960–965 (2008) 10.1038/nmat2318.

[33]J. W. Park, G. Y. Cho, J. Lee, and H. W. Yeom, "Emergent honeycomb network of topological excitations in correlated charge density wave", Nat. Commun **10**, 4038 (2019).

[34]T. Ishiguro and H. Sato, "Electron microscopy of phase transformations in 1T-TaS_2", Phys. Rev. B **44**, 2046–2060 (1991) 10.1103/physrevb.44.2046.

[35]M. D. Johannes and I. I. Mazin, "Fermi surface nesting and the origin of charge density waves in metals", Phys. Rev. B **77**, 165135 (2008) 10.1103/physrevb.77.165135.

[36]K. Rossnagel, "On the origin of charge-density waves in select layered transition-metal dichalcogenides", J. Phys.: Condens. Matter. **23**, 213001 (2011) 10.1088/0953-8984/23/21/213001.

[37]W. L. McMillan, "Landau theory of charge-density waves in transition-metal dichalcogenides", Phys. Rev. B **12**, 1187–1196 (1975) 10.1103/physrevb.12.1187.

[38]A. W. Overhauser, "Observability of charge-density waves by neutron diffraction", Phys. Rev. B **3**, 3173–3182 (1971) 10.1103/physrevb.3.3173.

[39]I. El Baggari, B. H. Savitzky, A. S. Admasu, J. Kim, S.-W. Cheong, R. Hovden, and L. F. Kourkoutis, "Nature and evolution of incommensurate charge order in manganites visualized with cryogenic scanning transmission electron microscopy", Proc. Natl. Acad. Sci. **115**, 1445–1450 (2018) 10.1073/pnas.1714901115.

[40]S. H. Sung, N. Schnitzer, L. Brown, J. Park, and R. Hovden, "Stacking, strain, and twist in 2d materials quantified by 3d electron diffraction", Phys. Rev. Materials **3**, 064003 (2019) 10.1103/PhysRevMaterials.3.064003.

[41]A. Zong, X. Shen, A. Kogar, L. Ye, C. Marks, D. Chowdhury, T. Rohwer, B. Freelon, S. Weathersby, R. Li, J. Yang, J. Checkelsky, X. Wang, and N. Gedik, "Ultrafast manipulation of mirror domain walls in a charge density wave", Sci. Adv. **4**, eaau5501 (2018) 10.1126/sciadv.aau5501.

[42]M. W. Tate, P. Purohit, D. Chamberlain, K. X. Nguyen, R. Hovden, C. S. Chang, P. Deb, E. Turgut, J. T. Heron, D. G. Schlom, D. C. Ralph, G. D. Fuchs, K. S. Shanks, H. T. Philipp, D. A. Muller, and S. M. Gruner, "High dynamic range pixel array detector for scanning transmission electron microscopy", Microsc. Microanal. **22**, 237–249 (2016) 10.1017/S1431927615015664.

[43]O. Panova, C. Ophus, C. J. Takacs, K. C. Bustillo, L. Balhorn, A. Salleo, N. Balsara, and A. M. Minor, "Diffraction imaging of nanocrystalline structures in organic semiconductor molecular thin films", Nat. Mater. **18**, 860–865 (2019) 10.1038/s41563-019-0387-3.

[44]Q. Qiao, S. Zhou, J. Tao, J. Zheng, L. Wu, S. T. Ciocys, I. Maria, D. J. Srolovitz, G. Karapetrov, and Y. Zhu, "Anisotropic charge density wave in layered 1T-$TiSe_2$", Phys. Rev. Mat. **1**, 054002 (2017) 10.1103/PhysRevMaterials.1.054002.

[45]B. H. Savitzky, I. El Baggari, A. S. Admasu, J. Kim, S.-W. Cheong, R. Hovden, and L. F. Kourkoutis, "Bending and breaking of stripes in a charge ordered manganite", Nat. Commun. **8**, 1883 (2017) 10.1038/s41467-017-02156-1.

[46]C. H. Chen, J. M. Gibson, and R. M. Fleming, "Microstructure in the incommensurate and the commensurate charge-density-wave states of 2H-$TaSe_2$: a direct observation by electron microscopy", Phys. Rev. B **26**, 184–205 (1982) 10.1103/physrevb.26.184.

[47]F. L. Givens and G. E. Fredericks, "Thermal expansion of $NbSe_2$ and TaS_2", J. Phys. Chem. Solids **38**, 1363–1365 (1977) 10.1016/0022-3697(77)90008-7.

[48]D. Sakabe, Z. Liu, K. Suenaga, K. Nakatsugawa, and S. Tanda, "Direct observation of monolayer, bi-layer, and tri-layer charge density waves in 1T-TaS_2 by transmission electron microscopy without a substrate", npj Quantum Mater. **2**, 22 (2017) 10.1038/s41535-017-0025-8.

[49]M. Yoshida, Y. Zhang, J. Ye, R. Suzuki, Y. Imai, S. Kimura, A. Fujiwara, and Y. Iwasa, "Controlling charge-density-wave states in nano-thick crystals of 1T-TaS_2", Sci. Rep. **4**, 7302 (2014) 10.1038/srep07302.

[50]P. Darancet, A. J. Millis, and C. A. Marianetti, "Three-dimensional metallic and two-dimensional insulating behavior in octahedral tantalum dichalcogenides", Phys. Rev. B **90**, 045134 (2014) 10.1103/physrevb.90.045134.

[51]Y. Imry and S.-k. Ma, "Random-field instability of the ordered state of continuous symmetry", Phys. Rev. Lett. **35**, 1399–1401 (1975) 10.1103/physrevlett.35.1399.

[52]J. Cardy, *Scaling and renormalization in statistical physics*, Vol. 5 (Cambridge university press, 1996).

[53]T. M. Rice, S. Whitehouse, and P. Littlewood, "Impurity pinning of discommensurations in charge-density waves", Phys. Rev. B. **24**, 2751–2759 (1981) 10.1103/physrevb.24.2751.

[54]W. L. McMillan, "Theory of discommensurations and the commensurate-incommensurate charge-density-wave phase transition", Phys. Rev. B **14**, 1496–1502 (1976) 10.1103/physrevb.14.1496.

[55]A. H. Thompson, F. R. Gamble, and R. F. Koehler, "Effects of intercalation on electron transport in tantalum disulfide", Phys. Rev. B **5**, 2811–2816 (1972) 10.1103/physrevb.5.2811.

Chapter V

Enhancement and Melting of Charge Density Waves with 2D Endotaxy

Introduction

Some exotic crystals spontaneously reorganize their valence electrons into periodic structures known as charge density waves (CDWs). In essence, two crystals emerge—the underlying atomic lattice and the emergent charge lattice. Just like atomic crystals, a charge density wave has defects: dislocations, disclinations, or elastic deformation [1–3]. Furthermore, the charge density wave can undergo phase transitions wherein the charge lattice constant and unit cell changes shape. All of this CDW reshaping and topological breaking occurs even when the underlying atomic lattice remains unchanged.

In low dimensions, these quantum phase transitions are promising candidates for novel devices [4–7], efficient ultrafast non-volatile switching [8–10], and suggest elusive chiral superconductivity [11–13]. Unfortunately, 2D CDWs are inherently unstable and accessing low-dimensional CDWs remains a challenge [14, 15]. Even worse, at elevated temperatures where devices typically operate, disruption of charge density waves is all but guaranteed due to ever present disorder [16–18]. A long-range ordered incommensurate CDW has yet to be reported.

Here we stabilize ordered incommensurate charge density waves (oIC-CDW) at elevated temperatures (T_{IC} = 350 K) in two-dimensions by endotaxial synthesis of TaS_2 polytype heterostructures. The estimated hundred-fold enhancement of the charge density wave has an increased coherence length comparable to the underlying atomic crystal. The enhanced order of the oIC-CDW increases electronic resistivity. This substantial enhancement of charge order is achieved through encapsulation of an isolated octahedral

TaS_2 CDW layer within a matrix of prismatic TaS_2 metallic layers via 2D endotaxial synthesis.

Realizing the ordered incommensurate CDW reveals CDWs have hexatic structure at high-temperature—that is, long-range translational symmetry is limited by topological breaking of the CDW through dislocations and disclinations. We show at high-temperatures, the CDWs in TaS_2 continuously melt as additional dislocations and disclinations form in the charge lattice. This hexatic CDW melting process was not previously observable since the incommensurate CDW normally emerges as a highly-disordered, melted state. By restoring order through 2D endotaxy, we can reversibly melt and unmelt CDWs in TaS_2. Based on these results, we access new regimes of the CDW phase diagram for octahedrally coordinated TaS_2 in temperature vs disorder space. Similar vestigial ordering (i.e., hexaticity) was predicted by Nie, Tarjus and Kivelson [17]; however, with 2D endotaxy we can now tune down the disorder in the CDW phase diagram.

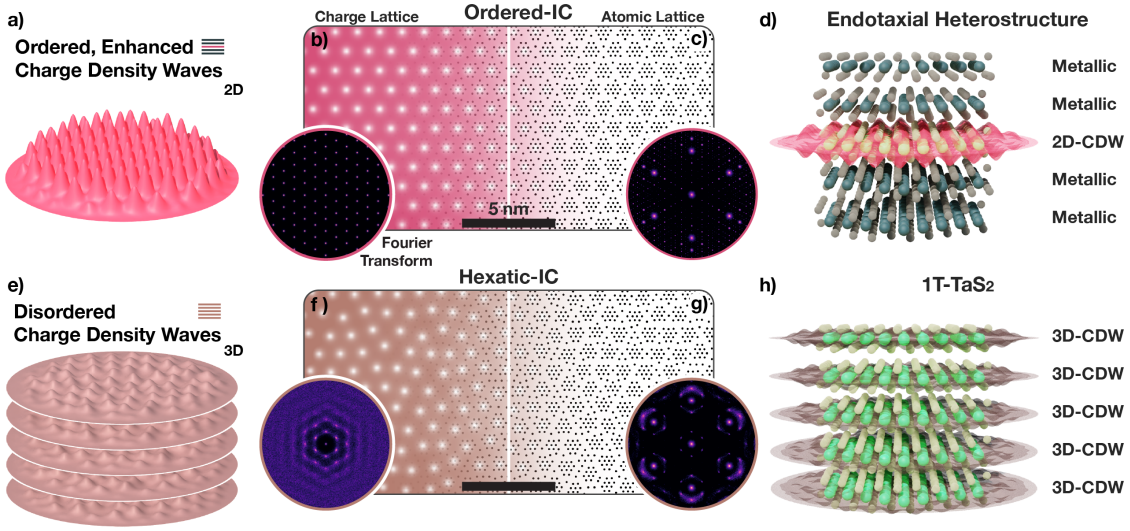

Figure V.1: Long-range Ordered Incommensurate Charge Density Waves. a) Schematic representation of ordered IC-CDW. The CDW is two-dimensional with little disorder. b) Ordered IC-CDW illustrated as a crystalline charge-density lattice. Inset) Fourier transform of the charge lattice shows well defined peaks. c) Associated periodic lattice distortions (PLDs) move tantalum nuclei along the charge density gradient. Inset) Simulated diffraction shows sharp superlattice peaks decorating Bragg peaks. d) Schematic representation of ordered IC-CDW in endotaxial polytype heterostructure. Mono- or few layers of endotaxially protected Oc-TaS_2 hosts 2D ordered IC-CDWs. e) Schematic representation of hexatic IC-CDW. The CDW phase is quasi-2D with non-trivial interlayer interactions, and hexatically disordered. f) Charge density distribution is comparable to hexatically disordered crystal lattice. Inset) Structure factor reveals azimuthally diffused peaks—characteristics of hexatic phases. g) Associated lattice distortion of IC-CDW with (inset) Fourier transform showing azimuthally blurred superlattice peaks while maintaining sharp Bragg peaks. h) Schematic representation of hexatic IC-CDW in bulk 1T-TaS2 where every layer hosts disordered IC-CDW.

The Ordered Incommensurate Charge Density Wave

The ordered incommensurate CDW (oIC) reported herein (Fig. V.1a–d) is strikingly distinct from the well-known incommensurate (IC) CDW (Fig. V.1e–h) found in 1T-TaS_2 or 1T-$TaSe_2$. Here, the oIC phase is a truly two-dimensional (2D) CDW with long-range positional and orientational order that couples strongly with the underlying crystal lattice (Fig. V.1a). The oIC-CDW, illustrated in Figure V.1b, is a crystalline charge-lattice with well-defined, sharp peaks in Fourier space (Fig. V.1b-inset). This CDW charge-lattice ($a_{CDW} = 11.87$ nm) exists within an underlying atomic lattice illustrated in Figure V.1c.

Electron–lattice interaction is an essential aspect of CDWs, and associated soft-phonon modes manifest as static periodic lattice distortions (PLDs) that reduce crystal symmetry and lower the electronic energy [19, 20]. For TaS_2, the CDW pulls atoms toward the nearest charge maximum to form periodic clusters of atoms (Fig. V.1c). Notably for incommensurate charge ordering, each cluster is distinct since the atomic lattice is not commensurate with the CDW. While these lattice distortions are small (<10 pm), selected area electron diffraction (SAED) is sensitive to subtle picoscale distortions and have been popular choice for characterization of CDW/PLDs [21]. CDW/PLDs diffract incident swift electrons into distinct superlattice peaks decorating each Bragg peak [2, 22–24]. In reciprocal space, the CDW charge lattice (Fig. V.1b-inset) and the measurable atomic superlattice peaks (Fig. V.1c-inset) have corresponding spacing, symmetry, and intensity.

Diffracted superlattice peaks provide a direct measure of the CDW lattice and contain rich information on their order-disorder. Specifically, diffraction represents an ensemble average of the structure over the selected area, and disorder manifests as diffused diffraction peaks [25, 26]. Disorder of CDWs smears superlattice peaks but leaves the principle Bragg peaks unaffected (Fig. V.1g-inset). For oIC-CDWs, the charge lattice is ordered with limited defects, thus diffraction shows both sharp superlattice and Bragg peaks (Fig. V.1c-inset). In contrast, the well-known IC-CDW in 1T-TaS_2 possesses significant disorder of its charge distribution. Across decades, the IC phase in 1T-TaS_2 is reported with a ring-like, azimuthally diffuse diffraction around each Bragg peak [22, 27–29], yet the origin of the diffused superlattice peaks is hardly discussed [30, 31].

Here we present the well-known IC-CDW in bulk 1T-TaS_2 as a hexatically disordered charge lattice containing dislocations and disclinations (Fig. V.1f). In-situ SAED of 1T-TaS_2 taken at 408 K (Fig. V.2a) shows azimuthally blurred first order superlattice peaks (marked brown). Averaging all six third order Bragg peaks (inset, Γ_3) better highlights

this point. Notably, hexatic phases are known to have six-fold rotational symmetric, azimuthally diffused peaks [32]. The experimental diffraction of IC-CDWs are consistent with a hexatic charge distribution (Fig. V.1f) [26, 31–33] and corresponding azimuthally diffuse structure factor (Fig. V.1f, g-inset). The IC-CDWs are three-dimensional (or quasi-2D) with non-negligible out-of-plane interactions (Fig. V.1e–h).

In contrast, the oIC-CDW, shows drastically sharper and stronger superlattice peaks measured by in-situ SAED at 408 K (Fig. V.2b). Sharpening is especially highlighted in averaged third order Bragg peaks (Γ_3). The measured superlattice peaks of oIC-CDW are sharper both in azimuthal (by $\sim$60%) and radial (by $\sim$50%) directions when compared to the IC-CDW. Notably, the superlattice peak widths of the oIC phase is comparable to the peak widths of the principle Bragg peaks. Therefore, the oIC is an spatially coherent electronic crystal over the selected area aperture size ($\sim$850 nm).

The oIC-CDW, a 2D charge ordered state, is enhanced by at least one-hundred fold over previously reported bulk IC-CDWs. Diffracted superlattice peaks in oIC-CDWs have an integrated intensity over ten times stronger despite that the number of charge ordered TaS_2 layers has been reduced to less than 10% of the material. Thus, endotaxial engineering improves not only the long range order but also the charge order amplitude of the IC-CDW. The correlation of long-range order and CDW enhancement is measured directly via hexatic CDW melting later in this manuscript.

Endotaxial Polytype Heterostructure of TaS_2

The oIC-CDW phase reported herein is stabilized by synthesizing endotaxial polytype heterostructures of TaS_2, where oIC-CDWs reside in monolayers of octahedrally coordinated (Oc-) TaS_2 embedded within prismatic (Pr-) TaS_2 matrix and one-to-one atomic registry (Fig. V.2e). Endotaxial polytype heterostructures are synthesized by heating 1T-TaS_2 at $\sim$720 K for 15–30 min in an inert environment. Notably, 1T-TaS_2 is metastable and goes through Oc-to-Pr endotaxial layer-by-layer polytype transformation upon heating ($\gtrsim$ 620 K). In-situ SAEDs (Fig. V.2c i–iv) were acquired at 20 seconds intervals at 408 K through the high temperature conversion process (723 K). These snapshots reveal sharpening of superlattice peaks—a clear indicator of enhanced CDW order. Cooling the sample midst transition stops the conversion and an interleaved polytype heterostructure is synthesized—confirmed by cross-sectional ADF-STEM.

Figure V.2d and e show atomic resolution micrographs of bulk 1T endotaxially con-

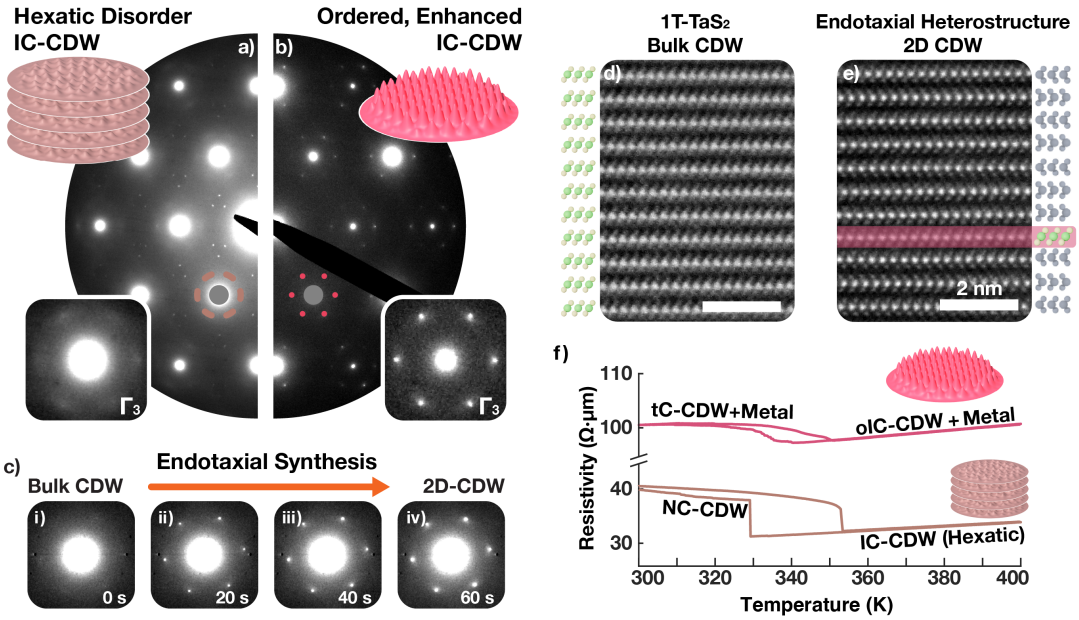

Figure V.2: Endotaxial Polytype Heterostructure of TaS_2. a) In bulk TaS_2, an IC-CDW phase emerges above 350 K, with azimuthally diffused superlattice peaks characteristic of hexatic disorder. b) oIC-CDW in endotaxial polytype heterostructure has enhanced long-range order and amplitude. Superlattice peaks are well-defined, sharper and brighter. c) Evolution of IC-CDW during the endotaxial synthesis. Atomic resolution cross-sectional HAADF-STEM of d) bulk and e) heat-treated TaS_xSe_{2-x} confirms polytypic transformation. After treatment, Pr layers encapsulate monolayers of Oc layers. Scale bar is 2 nm. A selenium doped sample was imaged to enhance chalcogen visibility. f) Resistivity vs temperature measurement of bulk (brown) and thermally-treated (red) TaS_2 shows a marked increase in resistivity in IC-CDW phases. In pristine sample IC-CDW gives way to nearly commensurate (NC-) CDW around 350 K. In polytype heterostructure, twinned commensurate (tC-) CDW emerges at a similar temperature range.

verted to a polytype heterostructure. The atomic resolution images demonstrate endotaxial monolayer encapsulation of Oc-TaS_2 (Fig. V.2e, highlighted red) in Pr-layers. The Pr-TaS_2 (bulk: 2H, 3R) are metallic above ∼100 K. Previous work showed these metallic layers decouple CDWs out-of-plane and raise the critical temperature for commensurate quantum states (i.e., C-CDW) up to 150 K [34].

Surprisingly, the endotaxial polytype heterostructure stabilizes long-range order in IC-CDWs at elevated ($\gtrsim$ 350 K) temperatures. The oIC-CDW phase has correlation length comparable to the crystal lattice, quantified by comparing widths of both superlattice and Bragg peaks from in-situ selected area electron diffraction patterns. This indicates the CDW is spatially coherent (i.e. defect-free) within the selected area aperture (∼850 nm diameter).

This enhancement of long-range CDW order is accompanied by a marked increase of the in-plane resistivity of the IC phase (Fig. V.2f). Figure V.2f shows temperature vs in-plane resistivity measurement of 1T (brown) and endotaxial (red) specimen. Resistivity of endotaxial TaS_2 is higher for IC-CDW phases (>358 K), despite having many metallic

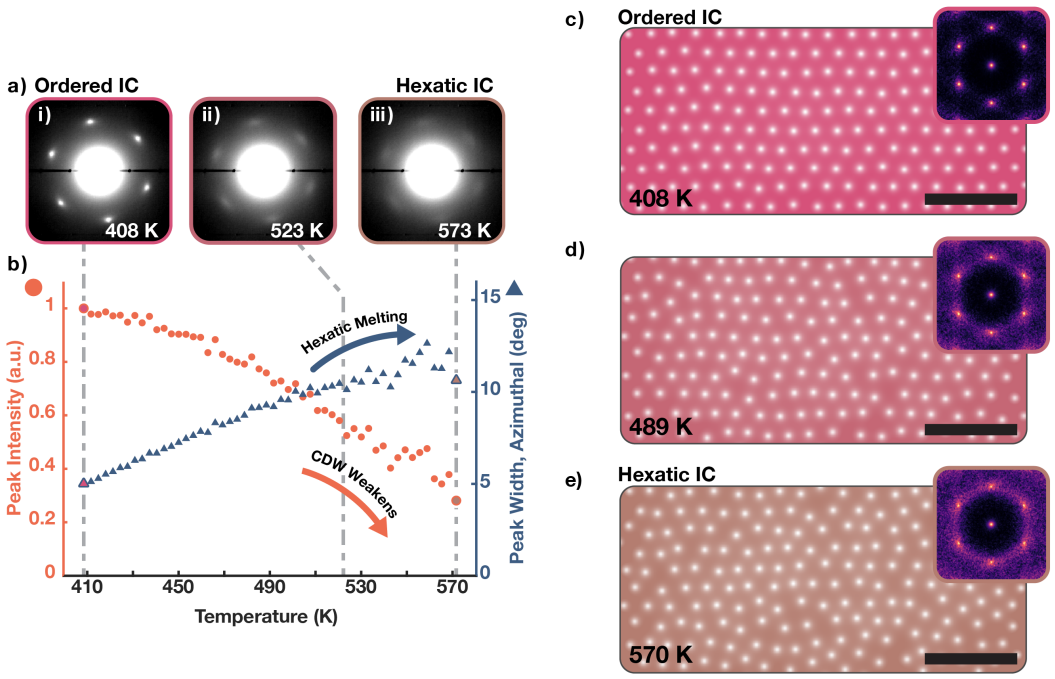

Figure V.3: Hexatic Melting of IC-CDWs. a) Averaged in-situ SAED patterns showing oIC-CDW superlattice peaks in endotaxial heterostructure. i—iii) As temperature increases (408 K, 523 K, 573 K), superlattice peaks continuously blur along azimuthal direction. b) Quantification of superlattice peak profile. b-blue) Azimuthal width of the peak continuously increases with temperature—a key feature in hexatic melting process. b-red) Integrated superlattice peak intensity of oIC phase monotonically decays as temperature increases despite the increase in peak width; CDW is weakening. c–e) Monte Carlo simulation of 2D Lennard-Jones crystal with increasing temperatures. This represents the charge density distribution. As temperature increases, the crystal progressively disorders with increasing numbers of disclinations and dislocations. Insets) Structure factor of the simulated crystals. six-fold symmetry is apparent. As temperature increases, peaks diffuse prominently along azimuthal direction.

layers introduced to the system. This implies that oIC-CDWs have a much higher resistivity than hexatic-IC in 1T-TaS_2.

Hexatic Melting of IC-CDW

Creating the oIC-CDW provides an ordered charge lattice that can be hexatically melted upon further heating. Hexatic melting is a uniquely 2D process wherein a crystal melts in two stages through the creation of dislocations and disclinations [33, 35–38]. During this process the reciprocal space structure continuously evolves. Initially at lower-temperatures (c.a. 350 K), the oIC phase is an ordered charge crystal with well-defined peaks reciprocal space (Fig. V.3c). As temperature rises, the CDW peaks continuously blur azimuthally as the density of dislocations and disclinations increases (Fig. V.3d, e). Azimuthal blurring of the reciprocal lattice is characteristic of hexatic phases and reflects the loss of translational symmetry while maintaining some orientational order [32]. Eventually, at higher temperatures (c.a. 570 K), the hexatic crystal completely dissociates into

an amorphous liquid state with ring-like structure factor. Figure V.3c–e, are generated using a phenomological Monte Carlo simulation wherein displacement of the CDW charge centers follow a temperature dependent Maxwell-Boltzmann probability distribution (See Methods). Here, the incommensurate CDW hexatically melts while the underlying atomic lattice remains unchanged—in diffraction this corresponds to a blurring of CDW superlattice peaks and preservation of Bragg peaks.

During the hexatic melting of oIC-CDWs, superlattice peaks increasingly blur as temperature is raised—clearly visible in in-situ SAED at Fig. V.3a-i) 473 K, Fig. V.3a-ii) 523 K, and Fig. V.3a-iii) 573 K. The blurring is anisotropic and more prominent along azimuthal directions as expected for hexatic phases. The CDW peaks are quantified throughout the melting process in Figure V.3b. Azimuthal peak width (Fig. V.3b, blue-triangles) increases continuously with temperature; roughly doubling when raised from 410 K to 570 K. Around 520 K the oIC has melted into a state that resembles the well-known IC-CDW for bulk TaS_2. This CDW melting process is reversible and peaks sharpen when temperature is decreased. Notably, Bragg peaks do not show appreciable changes indicating only the electronic crystal is melting, not the TaS_2 atomic crystal.

Although the CDW melting process appears hexatic, it is distinct from familiar liquid crystals, silica spheres, or atomic crystals wherein the amplitude of the order parameter does not change. Here, quantitative analysis of the superlattice peak intensities (Fig. V.3a-red) reveals the charge density wave amplitude decreases with temperature. This is expected as topological defects in CDWs (dislocations and disclinations) have locally divergent strain with elastic energy cost that forces a local amplitude collapse. These local CDW amplitude collapses have been observed at the center of topologcal defects in the 3D CDWs of manganites [1].

The CDW Phase Diagram for Octahedral TaS_2

Endotaxial synthesis of octahedrally coordinated TaS_2 allows access to new phases of matter and construction of a phase diagram for CDWs using temperature (T) and disorder (σ). The CDW phase diagram for 1T-TaS_2 is shown in Figure V.4. 1T-TaS_2 exists with native disorder and the ordered, commensurate phase (C-CDW, Fig. V.4g) is only observed at low-temperatures. At room temperature, the CDW is a partially-ordered NC phase (Fig. V.4f) that enters the hexatic IC phase upon heating (Fig. V.4e). At high-temperatures or high-disorder, CDWs degrade or vanish. The high disorder regime was historically achieved by substituting tantalum ions with other metal species (e.g. Ti, Nb) or by forc-

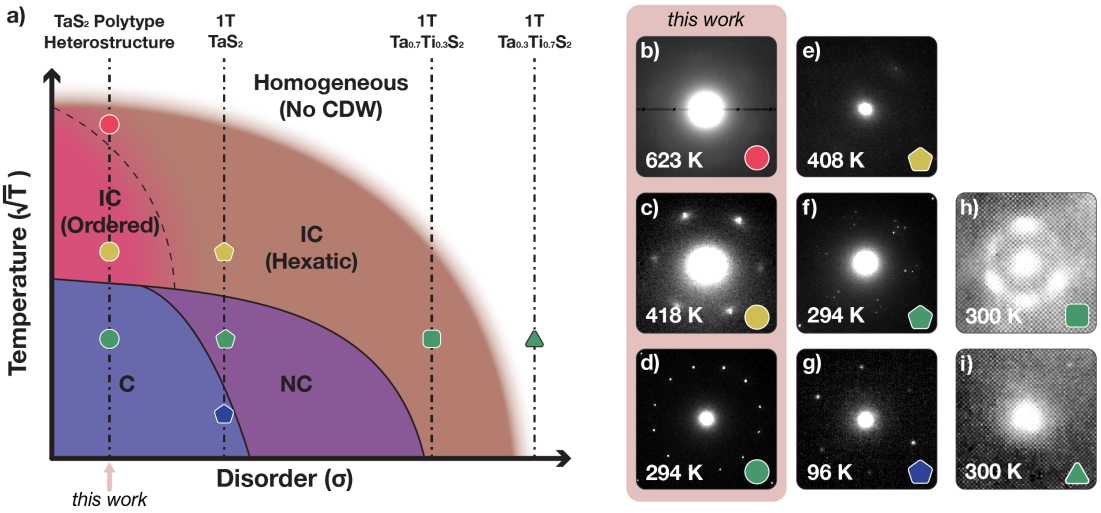

Figure V.4: Phase Diagram of Octahedrally Coordinated TaS_2. a) Schematic temperature vs disorder phase diagram of octahedrally coordinated TaS_2. As extrinsic disorder (σ) decreases, more ordered CDW phases are stabilized. At room temperature, polytype heterostructures with low disorder stabilizes C-CDW (d) instead of NC-CDW (f), and long-range ordered IC-CDW (c) phase instead of hexatically disordered IC-CDW (e). Furthermore, it stabilizes CDWs (b) at higher temperatures then bulk 1T-TaS_2 can ($T_{CDW} \cong 540$ K [39]). Substitutional disorder, on the other hand, destroys long-range order and hexatic IC-CDW is stable at room temperature (h) and leads to complete destruction of CDW eventually (i). b–i) Electron diffraction patterns showing superlattice peaks around a single Bragg peak reveals the charge ordering states. h,i) are adapted from Wilson et al. [22].

ing intercalates within the van der Waals gap [22]. At room temperature, mild substitution of titanium (1T-$Ta_{0.7}Ti_{0.3}S_2$) drives the system into hexatic-IC CDW states (Fig. V.4h), and as more titanium is substituted (1T-$Ta_{0.3}Ti_{0.7}S_2$) CDW vanishes completely (Fig. V.4i).

The low disorder regime, now accessible by endotaxial engineering, provides room temperature ordered C-CDWs and a novel ordered IC-CDW at higher temperatures. Notably with low-disorder, the C to IC transition is direct and the NC phase does not appear. The IC phase is ordered, but the CDW can be continuously melted into a disordered hexatic-IC phase (as described in figure V.3). The boundaries of the CDW phase diagram are drawn with consistency to hexatic melting of 2D collidal particles under temperature and disorder [40] as well as nematic CDWs [17, 18, 41].

Notably, CDWs in endotaxial TaS_2 are two dimensional and the oIC phase has enhanced order despite the 3D to 2D dimensionality reduction. In bulk 1T-TaS_2 CDWs are quasi-2D with non-negligible out-of-plane interaction (Fig. V.1h) [42–45]. Formation of endotaxial polytype heterostructures disrupts the out-of-plane interactions and CDWs reside in a protected 2D environment [34]. Stabilization of an ordered IC-CDW in 2D seemingly contradicts with Hohenberg-Mermin-Wagner theorem [14, 15] and Imry-Ma argument [16] which state spontaneous symmetry breaking of continuous symmetry (e.g. IC-CDWs) is unstable at non-zero temperatures in 2D. While both principles do not prevent

intermediate phases with short-range order (e.g., Berezinskii-Kosterlitz-Thouless (BKT) transition [33, 46]), the 2D CDWs should be none-the-less more fragile to disorder. An ordered IC phase can only emerge in ultra-clean environments. Here endotaxial TaS_2 is a synthesis protects CDW states by strain-free encapsulation in an chemically identical environment of metallic layers that shield off disorder.

Conclusion

In summary, we demonstrate that endotaxial synthesis of clean interleaved polytypic heterostructures can stabilize fragile quantum phases such as ordered CDWs even at high temperatures. Here, we stabilize and enhance 2D charge density waves (both long-range order and amplitude) in an endotaxially confined monolayer of 1T-TaS_2. Surprisingly, the low-dimensional symmetry breaking of an ordered incommensurate CDW (oIC-CDW) appears, suggesting the quantum states reside within minimal extrinsic disorder. By enhancing CDW order the hexatic nature of IC-CDWs are revealed. Experimental observation matches advanced simulation of electron diffraction of charge lattices to provide the real-space evolution of 2D CDW melting. Heating the oIC-CDW in-situ TEM above 400 K we see a reversable hexatic melting process, in which disclinations and dislocations destroy long-range translational symmetry of the CDW while maintaining its orientational order. The CDW melts well before the underlying atomic crystal changes. In 2D, CDWs are expected to manifest through vestigial electronic hexaticity—a weak CDW with substantial defects and short range order. The nature of vestigial phases in CDWs remains poorly understood with little direct evidence. From these results, a CDW phase diagram for 1T-TaS_2 is created and consistent with the predicted emergence of vestigial quantum order.

References

[1]B. H. Savitzky, I. El Baggari, A. S. Admasu, J. Kim, S.-W. Cheong, R. Hovden, and L. F. Kourkoutis, "Bending and breaking of stripes in a charge ordered manganite", Nat. Commun. **8**, 1883 (2017) 10.1038/s41467-017-02156-1.

[2]I. El Baggari, B. H. Savitzky, A. S. Admasu, J. Kim, S.-W. Cheong, R. Hovden, and L. F. Kourkoutis, "Nature and evolution of incommensurate charge order in manganites visualized with cryogenic scanning transmission electron microscopy", Proc. Natl. Acad. Sci. **115**, 1445–1450 (2018) 10.1073/pnas.1714901115.

[3]Y. I. Joe, X. M. Chen, P. Ghaemi, K. D. Finkelstein, G. A. de la Pena, Y. Gan, J. C. T. Lee, S. Yuan, J. Geck, G. J. Macdougall, T. C. Chiang, S. L. Cooper, E. Fradkin, and P. Abbamonte, "Emergence of charge density wave domain walls above the superconducting dome in 1T-$TiSe_2$", Nat. Phys. **10**, 421–425 (2014) 10.1038/nphys2935.

[4]M. J. Hollander, Y. Liu, W.-J. Lu, L.-J. Li, Y. P. Sun, J. A. Robinson, and S. Datta, "Electrically driven reversible insulator–metal phase transition in 1T-TaS_2", Nano Lett. **15**, 1861–1866 (2015) 10.1021/nl504662b.

[5]G. Liu, B. Debnath, T. R. Pope, T. T. Salguero, R. K. Lake, and A. A. Balandin, "A charge-density-wave oscillator based on an integrated tantalum disulfide–boron nitride–graphene device operating at room temperature", Nat. Nanotechnol. **11**, 845–850 (2016) 10.1038/nnano.2016.108.

[6]D. N. Basov, R. D. Averitt, and D. Hsieh, "Towards properties on demand in quantum materials", Nat. Mater. **16**, 1077–1088 (2017) 10.1038/nmat5017.

[7]Y. Tokura, M. Kawasaki, and N. Nagaosa, "Emergent functions of quantum materials", Nat. Phys **13**, 1056–1068 (2017) 10.1038/nphys4274.

[8]A. W. Tsen, R. Hovden, D. Wang, Y. D. Kim, J. Okamoto, K. A. Spoth, Y. Liu, W. Lu, Y. P. Sun, J. C. Hone, L. F. Kourkoutis, P. Kim, and A. N. Pasupathy, "Structure and control of charge density waves in two-dimensional 1T-TaS_2", Proc. Natl. Acad. Sci. **112**, 15054–15059 (2015) 10.1073/pnas.1512092112.

[9]I. Vaskivskyi, I. A. Mihailovic, S. Brazovskii, J. Gospodaric, T. Mertelj, D. Svetin, P. Sutar, and D. Mihailovic, "Fast electronic resistance switching involving hidden charge density wave states", Nat. Commun. **7**, 11442 (2016) 10.1038/ncomms11442.

[10]S. Hellmann, T. Rohwer, M. Kallane, K. Hanff, C. Sohrt, A. Stange, A. Carr, M. M. Murnane, L. Kapteyn, L. Kipp, M. Bauer, and K. Rossnagel, "Time-domain classification of charge-density-wave insulators", Nat. Commun. **3**, 1069 (2012) 10.1038/ncomms2078.

[11]R. Ganesh, G. Baskaran, J. van den Brink, and D. V. Efremov, "Theoretical prediction of a time-reversal broken chiral superconducting phase driven by electronic correlations in a single $TiSe_2$ layer", Phys. Rev. Lett. **113**, 177001 (2014) 10.1103/PhysRevLett.113.177001.

[12]A. Ribak, M. R. Skiff, M. Mograbi, P. K. Rout, M. H. Fishcer, J. Ruhman, K. Chashka, Y. Dagan, and A. Kanigel, "Chiral superconductivity in the alternate stacking compound 4Hb-TaS_2", Sci. Adv. **6**, eaax9480 (2020) 10.1126/sciadv.aax9480.

[13]E. Navarro-Moratalla, J. O. Island, S. Mañas-Valero, E. Pinilla-Cienfuegos, A. Castellanos-Gomez, J. Quereda, G. Rubio-Bollinger, L. Chirolli, J. A. Silva-Guillén, N. Agraït, G. A. Steele, F. Guinea, H. S. J. van der Zant, and E. Coronado, "Enhanced superconductivity in atomically thin TaS_2", Nat. Commun. **7**, 11043 (2016) 10.1038/ncomms11043.

[14]N. D. Mermin and H. Wagner, "Absence of ferromagnetism or antiferromagnetism in one- or two-dimensional isotropic heisenberg models", Phys. Rev. Lett **17**, 1133–1136 10.1103/PhysRevLett.17.1133.

[15]P. C. Hohenberg, "Existence of long-range order in one and two dimensions", Phys. Rev **158**, 383–386 (1967) 10.1103/PhysRev.158.383.

[16]Y. Imry and S.-k. Ma, "Random-field instability of the ordered state of continuous symmetry", Phys. Rev. Lett. **35**, 1399–1401 (1975) 10.1103/physrevlett.35.1399.

[17]L. Nie, G. Tarjus, and S. A. Kivelson, "Quenched disorder and vestigial nematicity in the pseudogap regime of the cuprates", Proc. Natl. Acad. Sci. **111**, 7980–7985 (2014) 10.1073/pnas.1406019111.

[18]Y. Yao, R. Willia, T. Lacmann, S.-M. Souliou, M. Frachet, K. Willia, M. Merz, F. Weber, C. Meingast, R. Heid, A.-A. Haghighirad, S. J., and M. Le Tacon, "An electronic nematic liquid in $BaNi_2As_2$", Nat. Commun. **13**, 4535 (2022) 10.1038/s41467-022-32112-7.

[19]W. L. McMillan, "Landau theory of charge-density waves in transition-metal dichalcogenides", Phys. Rev. B **12**, 1187–1196 (1975) 10.1103/physrevb.12.1187.

[20]R. Peierls, "Zur theorie der elektrischen und thermischen leitfähigkeit von metallen", Ann. Phys. **396**, 121–148 (1930) 10.1002/andp.19303960202.

[21]S. H. Sung, Y. M. Goh, H. Yoo, R. Engelke, H. Xie, K. Zhang, Z. Li, A. Ye, P. B. Deotare, E. B. Tadmor, A. J. Mannix, J. Park, L. Zhao, and R. Kim P. Hovden, "Two-dimensional charge order stabilized in clean polytype heterostructures", Nat. Commun. **13**, 7826 (2022) 10.1038/s41467-022-35477-x.

[22]J. Wilson, F. Di Salvo, and S. Mahajan, "Charge-density waves and superlattices in the metallic layered transition metal dichalcogenides", Adv. Phys. **24**, 117–201 (1975) 10.1080/00018737500101391.

[23]A. W. Overhauser, "Observability of charge-density waves by neutron diffraction", Phys. Rev. B **3**, 3173–3182 (1971) 10.1103/physrevb.3.3173.

[24]R. Hovden, A. W. Tsen, P. Liu, B. H. Savitzky, I. El Baggari, Y. Liu, W. Lu, Y. P. Sun, P. Kim, A. N. Pasupathy, and L. F. Kourkoutis, "Atomic lattice disorder in charge-density-wave phases of exfoliated dichalcogenides (1T-TaS_2)", Proc. Natl. Acad. Sci. **113**, 11420–11424 (2016) 10.1073/pnas.1606044113.

[25]K. Huang, "X-ray reflexions from dilute solid solutions", Proc. R. Soc. Lond. A **190**, 102–117 (1947) 10.1098/rspa.1947.0064.

[26]I. R. Peterson and V. M. Kaganer, "Diffraction line profile of a two-dimensional hexatic", Phys. Rev. Lett. **73**, 10.1103/PhysRevLett.73.102 (1994) 10.1103/PhysRevLett.73.102.

[27]P. M. Williams, G. S. Parry, and C. B. Scrub, "Diffraction evidence for the kohn anomaly in 1t tas_2", Philos. Mag., 695–699 (1974) 10.1080/14786437408213248.

[28]J. van Landuyt, G. van Tendeloo, and S. Amelincky, "Electron diffraction study of inter- and intrapolytypic phase transitions in transition metal dichalcogenides. i. electron diffraction patterns", Phys. Status Solidi A, 359–376 (1974) 10.1002/pssa.2210260138.

[29]T. Ishiguro and H. Sato, "Electron microscopy of phase transformations in 1T-TaS_2", Phys. Rev. B **44**, 2046–2060 (1991) 10.1103/physrevb.44.2046.

[30]T. R. Welberry and R. L. Withers, "Optical transforms of disordered systems displaying diffuse intensity loci", J. Appl. Cryst. **20**, 280–288 (1987) 10.1107/S0021889887086667.

[31]H. Dai and C. M. Lieber, Phys. Rev. Lett **69**, 1576–1579 (1992) 10.1103/PhysRevLett.69.1576.

[32]J. D. Brock, R. J. Birgeneau, and A. Lister D. a nd Aharony, "Hexatic ordering in liquid crystal films", Contemp. Phys **30**, 321–335 (1989) 10.1080/00107518908213772.

[33]J. M. Kosterlitz and D. J. Thouless, "Ordering, metastability and phase transitions in two-dimensional systems", Journal of Physics C: Solid State Physics **6**, 1181–1203 (1973) 10.1088/0022-3719/6/7/010.

[34]S. H. Sung, N. Schnitzer, S. Novakov, I. El Baggari, X. Luo, J. Gim, N. M. Vu, Z. Li, T. H. Brintlinger, Y. Liu, W. Lu, Y. P. Sun, P. B. Deotare, K. Sun, L. Zhao, L. F. Kourkoutis, J. T. Heron, and R. Hovden, "Two-dimensional charge order stabilized in clean polytype heterostructures", Nat. Commun. **13**, 413 (2022) 10.1038/s41467-021-27947-5.

[35]J. M. Kosterlitz and D. J. Thouless, "Long range order and metastability in two dimensional solids and superfluids. (application of dislocation theory)", Journal of Physics C: Solid State Physics **5**, L124–L126 (1972) 10.1088/0022-3719/5/11/002.

[36]B. I. Halperin and D. R. Nelson, "Theory of two-dimensional melting", Phys. Rev. Lett. **41**, 121–124 (1978) 10.1103/PhysRevLett.41.121.

[37]D. R. Nelson, M. Rubinstein, and F. Spaepen, "Order in two-dimensional binary random arrays", Philos. Mag. A **46**, 105–126 (1982) 10.1080/01418618208236211.

[38]A. P. Yougn, "Melting and the vector coulomb gas in two dimensions", Phys. Rev. B **19**, 1855–1866 (1979) 10.1103/PhysRevB.19.1855.

[39]S. C. Bayliss, A. Clarke, and L. Y. Liang, "Optical and thermal evidence for the metal-insulator transition in 1T-TaS_2", J. Phys. C: Solid State Phys. **16**, L831–L834 (1983) 10.1088/0022-3719/16/23/002.

[40]S. Deutschländer, T. Horn, H. Löwen, G. Maret, and P. Keim, "Two-dimensional melting under quenched disorder", Phys. Rev. Lett. **111**, 098301 (2013) 10.1103/PhysRevLett.111.098301.

[41]M. Frachet, P. Wiecki, T. Lacmann, S. M. Souliou, C. Willia K. Meingast, M. Merz, A.-A. Haghighirad, M. Le Tacon, and A. E. Böhmer, "Elastoresistivity in the incommensurate charge density wave phase of $BaNi_2(As_{1-x}P_x)_2$", npj Quant. Mater. **7**, 115 (2022) 10.1038/s41535-022-00525-8.

[42]M. Naito, H. Nishihara, and S. Tanaka, "Nuclear quadrupole resonance in the charge density wave state of 1T-TaS_2", J. Phys. Soc. Jpn. **53**, 1610–1613 (1984) 10.1143/JPSJ.53.1610.

[43]S. Tanda, T. Sambongi, T. Tani, and S. Tanaka, "X-ray study of charge density wave structure in 1T-TaS_2", J. Phys. Soc. Jpn. **53**, 476–479 (1984) 10.1143/JPSJ.53.476.

[44]T. Ritschel, J. Trinckquf, K. Koepernik, B. Büchner, Z. M. V., H. Berger, Y. I. Joe, P. Abbamonte, and J. Geck, "Orbital textures and charge density waves in transition metal dichalcogenides", Nat. Phys. **11**, 328–331 (2015) 10.1038/nphys3267.

[45]Q. Stahl, M. Kusch, F. Heinsch, G. Garbarino, N. Kretzschmar, K. Hanff, K. Rossnagel, J. Geck, and T. Ritschel, "Collapse of layer dimerization in the photo-induced hidden state of 1t-tas_2", Nat. Commun. **11**, 1247 (2020) 10.1038/s41467-020-15079-1.

[46]V. L. Berezinskiĭ, "Destruction of long-range order in one-dimensional and two-dimensional systems having a continuous symmetry group i. classical systems", Sov. Phys. JETP **32**, 493–500 (1970).

Chapter VI

Conclusion

Summary

Chapter I provided a brief introduction to electron microscopy and electron diffraction. Specifically, it motivated usage of high energy electron beam to achieve kinematic diffraction condition. Electron diffraction, while it is an old technique, is mature and still powerful tool for materials science.

3D reciprocal structure of 2D materials were extensively discussed in Chapter II. Despite its name, 2D materials have fascinating third dimension morphology and the out-of-plane interaction often play a significant role in the materials property. We introduced 3D electron diffraction, a powerful technique that captures rich out-of-plane information in 2D materials. Here, we identified the exact stacking and number of layers of 1, 2, 6, and 12 layer graphene and revealed metal–chalcogen coordination and bond length of monolayer MoS_2.

In Chapter III, we explored interlayer twist, a tunability unique to 2D materials. Moiré heterostructures periodically relaxes due to modulated out-of-plane interactions. We introduced torsional PLD as the single order parameter that describes positions of >10,000 carbon atoms. Furthermore, we experimentally quantify the torsional PLD amplitude from a single electron diffraction pattern.

In Chapter IV, we stabilize spatially-coherent, long-range ordered commensurate (C-) CDWs well above the room temperature by engineering novel endotaxial heterostructures of TaS_2 (up to 150 K increase in the critical temperature). The stabilization of ordered electronic phases with 2D endotaxy has significant implications for routes to access fragile, exotic correlated electron states. Stabilization of 2D CDWs with endotaxial engineering

has further implications in condensed matter physics. Low dimensional physics is hard to experimentally study because true 2D system is rare. The endotaxial heterostructure is a potential platform for experimental demonstration of exotic 2D physics.

In Chapter V, we took one step further with endotaxial engineering. Here, we enhanced long-range order and amplitude of incommensurate CDWs using 2D endotaxy. We showed enhancement process is equivalent to crystallizing a charge lattice, and highlighted hexatic nature of IC-CDW phase in octahedrally coordinated TaS_2. In combination of Chapter IV and V, we produced a charge order phase diagram for TaS_2 in temperature vs. disorder space.

Future Works

Here I discuss few possible future works.

In twisted bilayer graphene, localized AA core are expected to have large interlayer spacing and result in periodic buckling of the structure. However, torsional PLD model in Chapter III does not account for out-of-plane components of PLDs. Such buckling will result superlattice peaks to modulate along $\hat{\mathbf{k}}_z$. Using 3D electron diffraction, introduced in Chapter II, the out-of-plane rod structure of superlattice peaks should be captured, revealing full 3D structure of twisted 2D materials.

While Chapter IV and V of this thesis contains extensive works on CDW phases of TaS_2, there are much more to be studied. Historically, there are numerous experimental data and speculations on the room temperature nearly-commensurate (NC) phase, yet the nature of NC-CDW is still being debated. Specifically, there is still no full explanation of why NC-CDW diffraction pattern looks way it is. Combination of Landau theory based model with real space inhomogeneities added with Monte-Carlo method might shed light the perplexing structure of NC-CDW.

Lastly, endotaxial engineering have not been applied to other materials yet. There are numerous 2D materials that exhibits polytype transformations such as $MoTe_2$. Formation of endotaxial heterostructures might lead to unexpected, exciting discoveries.

APPENDICIES

Appendix A. Appendix for Chapter II

A.1. Mathematical Formulation of 2D Lattice

A 1D lattice with lattice constant a can be represented as an infinite array of Dirac delta functions ($\sum_m \delta(x - ma)$), or more compactly as a 'Shah' function ($\text{Ш}_a(x)$). The Fourier transform of the 1D Shah function using the non-unitary, angular frequency convention (i.e $\mathcal{F}[\,] = \int dx\, e^{-ikx}[\,]$) is:

$$\mathcal{F}[\text{Ш}_a(x)] = \text{Ш}_b(k), \tag{A.1}$$

where b is the reciprocal lattice constant. Note a normalization factor $\frac{2\pi}{a}$ has been included in reciprocal space Shah function, $\text{Ш}_b(k)$.

Expanding the definition, the 2D Shah function with two lattice vectors, $\mathbf{a_1}, \mathbf{a_2}$ ($\text{Ш}_{\mathbf{a}_1,\mathbf{a}_2}(\mathbf{r}_{xy})$) represents a 2D lattice:

$$\text{Ш}_{\mathbf{a_1},\mathbf{a_2}} = \sum_{m,n} \delta^2(\mathbf{r}_{xy} - (m\mathbf{a_1} + m\mathbf{a_2})). \tag{A.2}$$

The Fourier transform of the 2D Shah is $\text{Ш}_{\mathbf{b}_1,\mathbf{b}_2}(\mathbf{k_{xy}})$. Here $\mathbf{b_1}, \mathbf{b_2}$ are the reciprocal lattice vectors. This notation includes a normalization factor absorbed into the reciprocal Shah function, where the factor depends on the dimension of the function. The normalization factors are $\frac{2\pi}{a}, \frac{(2\pi)^2}{\Omega}, \frac{(2\pi)^3}{V}$ for the 1D, 2D and 3D cases, where a, Ω, V are the 1D, 2D, and 3D volumes of the real-space unit cell, respectively.

However, because the lattice is defined on a 2D plane, the real-space lattice points are infinite lines along $\hat{\mathbf{z}}$. To properly formulate a 2D planar lattice in 3D and place it in arbitrary z-position z_0, an additional delta function is necessary: ($\text{Ш}_{\mathbf{a}_1,\mathbf{a}_2}(\mathbf{r}_{xy})\delta(z - z_0)$). Applying the 3D Fourier transform, the reciprocal structure of the 2D lattice is:

$$\mathcal{F}[\text{Ш}_{\mathbf{a}_1,\mathbf{a}_2}(\mathbf{r}_{xy})\delta(z - z_0)] = e^{-ik_z z_0}\text{Ш}_{\mathbf{b}_1,\mathbf{b}_2}(\mathbf{k}_{xy}). \tag{A.3}$$

Therefore, the 3D reciprocal lattice of a 2D crystal is a 2D array of rods with phase associated with the z position.

A.2. Parameterizing the Ewald Sphere in Terms of Specimen Orientation

The Ewald sphere is most intuitively parameterized in terms of specimen orientation in spherical coordinates, where ϕ is the rotation angle of the specimen about the beam axis, and θ is the specimen tilt angle relative to the beam direction. The radius of the Ewald sphere is the wavenumber of the electron beam (k_0). A reciprocal space coordinate on the $k_z = 0$ plane $(k_x, k_y, 0)$ will be transformed as $k'_x = k_x - k_0 \sin(\theta)\cos(\phi)$, $k'_y = k_y - k_0 \sin(\theta)\sin(\phi)$, $k'_z = k_0 \cos(\theta)$. Thus, in Cartesian coordinates the Ewald sphere will cut through a reciprocal space rod at

$$k_z = k'_z - \sqrt{k_0^2 - {k'_x}^2 - {k'_y}^2} \tag{A.4}$$

and the in-plane radial distance to the reciprocal space origin is given by $k_\rho = \sqrt{k_x^2 + k_y^2}$

A.3. Extracting Number of Layers in Graphene from 2nd Order Rods

The three sublattices (A, B, C) of registered graphene have different phases associated with them ($\phi_A = 1 + e^{-\frac{2\pi i}{3}(h+k)}, \phi_B = e^{-\frac{2\pi i}{3}(h+k)} + e^{-\frac{4\pi i}{3}(h+k)}, \phi_C = 1 + e^{-\frac{4\pi i}{3}(h+k)}$), where *h*, *k* are reciprocal lattice indices. For example, in the 2nd order rods (e.g. $h = 1$, $k = -1$), the phase terms simply equal constants ($\phi_{A,B,C} = 2$).

Placing a sublattice at a specific $z = z_0$ adds an extra phase of $e^{-ik_z z_0}$. Therefore adding N layers with equal interlayer spacing (λ_L) results in the typical finite size effect for a crystal, a complex magnitude of $2(1+e^{-ik_z\lambda_L+e^{-2ik_z\lambda_L}}+...+e^{-ik_z\lambda(N-1)})$, or more compactly $2\sum_{n=0}^{N-1}(e^{-ik_z\lambda_L})^n$. This geometric series can be expanded as $2\frac{1-e^{-ik_z\lambda_L N}}{1-e^{-ik_z\lambda_L}}$. The measured intensity is equal to the magnitude squared:

$$I = 4\frac{\sin^2 ½k_z\lambda_L N}{\sin^2 ½k_z\lambda_L} \tag{A.5}$$

The numerator reaches zero at $k_z = \frac{2\pi m}{\lambda_L N}, m \in \mathbb{Z}$. If we choose $m = 1$ (the first minimum), the intensity is also zero with the exception of $N = 1$ (trivial SLG case). Therefore, the first minimum of the 2nd order Bragg rods of multilayer graphene occurs at $k_z = \frac{2\pi}{\lambda_L N}$

When tilted along the first order peaks by an angle θ, the diffraction plane slices the 2nd order rods at $k_z = b_g\sqrt{3}\tan\theta$, where $b_g = \frac{4\pi}{a_g\sqrt{3}}$ and a_g is the lattice constant of graphene. Substituting, we can arrive at $N = \frac{a_g}{2\lambda_L \tan\theta}$. Using $a_g = 2.46$ Å, $\lambda_L = 3.346$Å, $\tan\theta \approx \theta$ (in

radians), we arrive at:

$$N \approx \frac{21}{\theta(deg)} \tag{A.6}$$

A.4. Measuring Thickness in Multilayer Graphene from 2nd Order Bragg Rods

The maxima of measured intensity (Eq. 5) is at $k_z = \frac{(2m+1)\pi}{\lambda_L N}$:

$$I_m = \frac{4}{\sin^2 \frac{(2m+1)\pi}{2N}} \tag{A.7}$$

The relative intensity these maxima depends only on the number of layers, N.

$$\frac{I_m}{I_{m'}} = \frac{\sin^2 \frac{(2m'+1)\pi}{2N}}{\sin^2 \frac{(2m+1)\pi}{2N}} \tag{A.8}$$

Looking at this ratio for $(m, m') = (1, 2)$, we compare the maximum between the 1st and 2nd minima, and the maximum between the 2nd and 3rd minima:

$$\frac{I_1}{I_2} = \frac{\sin^2 \frac{5\pi}{2N}}{\sin^2 \frac{3\pi}{2N}} \tag{A.9}$$

Comparison of this expression with experimental data determines the number of layers in samples.

A.5. Extracting Fraction of Sublattices of Graphene

From Appendix A.3, the phase associated with each of the sub-lattices of registered graphene are $\phi_A = 1 + e^{-\frac{2\pi i}{3}(h+k)}, \phi_B = e^{-\frac{2\pi i}{3}(h+k)} + e^{-\frac{4\pi i}{3}(h+k)}, \phi_C = 1 + e^{-\frac{4\pi i}{3}(h+k)}$. Looking at $k_z = 0$, there is no phase term related to the out-of-plane; real-space equivalence of projected view.

Therefore the total added phase at k_z with N total layers and N_A, N_B, N_C layers for each sublattice, is:

$$\begin{aligned} &N_A(1 + e^{-\frac{2\pi i}{3}(h+k)}) + N_B(e^{-\frac{2\pi i}{3}(h+k)} + e^{-\frac{4\pi i}{3}(h+k)}) \\ &+ N_C(1 + e^{-\frac{4\pi i}{3}(h+k)}) \end{aligned} \tag{A.10}$$

For the 2nd order rods ($h+k=0$), the phase term reduces to $2(N_A+N_B+N_C)=2N$, resulting in a magnitude squared intensity of $4N^2$ for the 2nd order peaks at $k_z=0$.

For the 1st order peaks ($h+k=1$), the squared intensity reduces to phase term reduces to $N^2-3(N_AN_B+N_AN_C+N_BN_C)$. Defining fractional sublattice number $n_i \equiv N_i/N$, the relative intensity of 1st order to 2nd order is: $\frac{1-3(N_AN_B+N_AN_C+N_BN_C)}{N^2} = \frac{1-3(n_An_B+n_An_C+n_Bn_C)}{4}$

The scattering factor of the carbon atom is about 4.5 times greater at Γ_1 site than at Γ_2. Taking this into account, the relative intensity is then:

$$I_{1st/2nd} \approx 1-3(n_An_B+n_An_C+n_Bn_C). \tag{A.11}$$

Therefore, the rhombohedral stacking (ABCABCABC..., i.e $n_A=n_B=n_C=\frac{1}{3}$) has $I_{1st/2nd}=0$, while the Bernal stacking (ABABAB..., i.e $n_A=n_B\frac{1}{2}, n_C=0$) has $I_{1st/2nd}\approx 0.25$

A.6. Evolution of Bragg Rods with Thickness

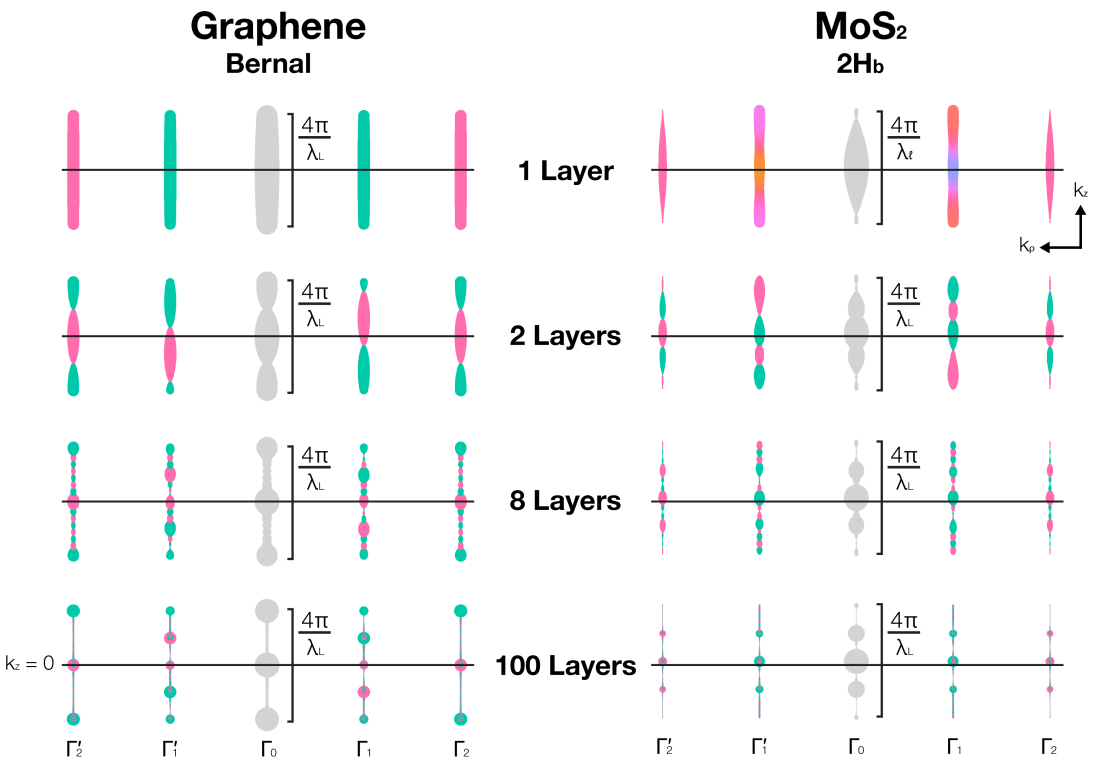

Figure VI.1: Evolution of Bragg Rods with Thickness. Sideview of the Bragg rods $(\Gamma_0, \Gamma_1, \Gamma_2)$ quantitatively illustrates the structure in k-space. With additional layers the rods converge into Bragg peaks. The thickness and color indicates complex magnitude and phase respectively.

A.7. Atlas of 3D Reciprocal Structure of 2D Materials

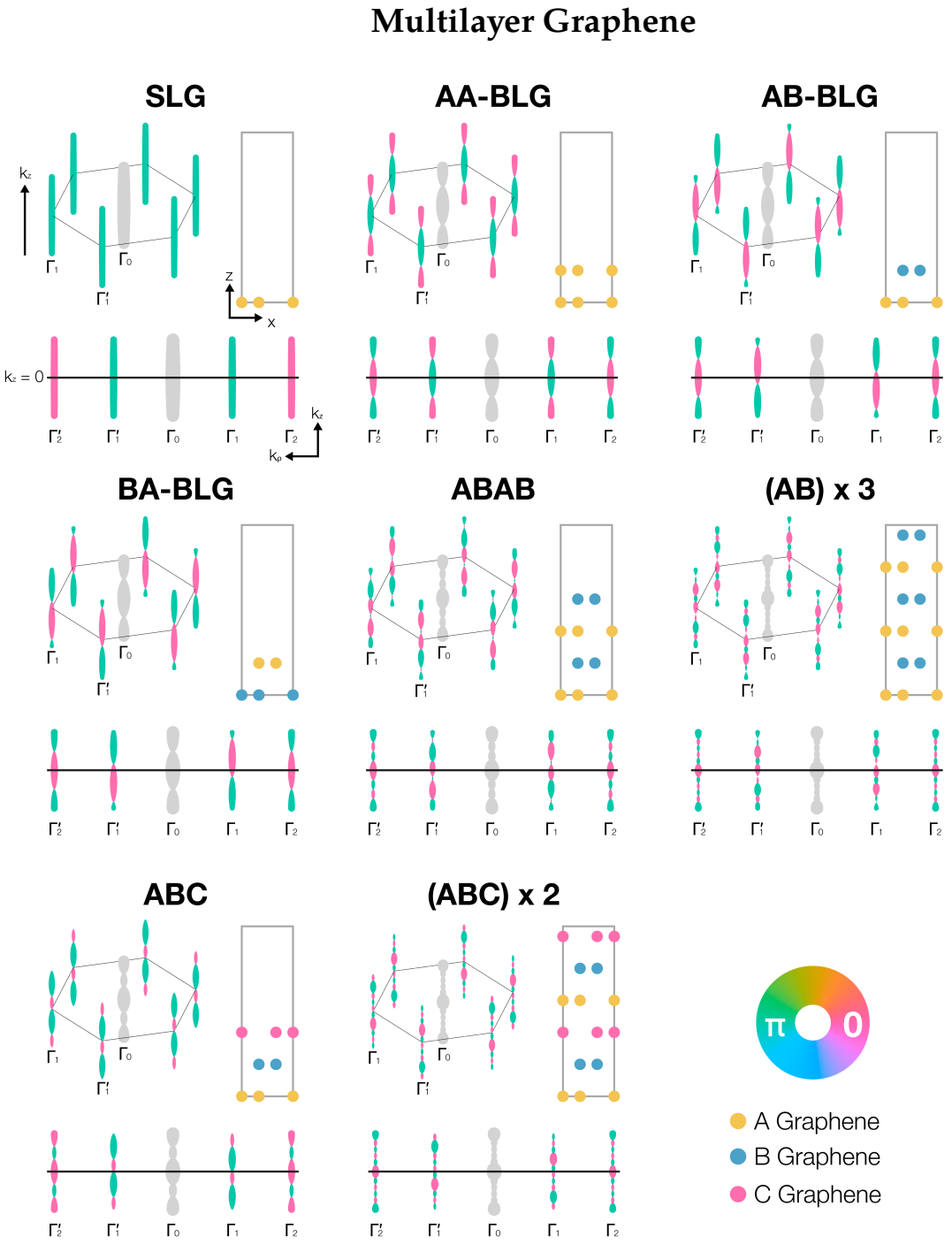

Figure VI.2: 3D Reciprocal Structure of Multilayer Graphene. The Bragg rods (Γ_0, Γ_1) are shown in 3D alongside a real-space <100> projection of the crystal stacking order. Below, a sideview of the Bragg rods $(\Gamma_0, \Gamma_1, \Gamma_2)$ quantitatively illustrates the structure in k-space. Bragg rods have thickness and color indicating the complex magnitude and phase respectively.

A.8. Atlas of 3D Reciprocal Structure of 2D Materials

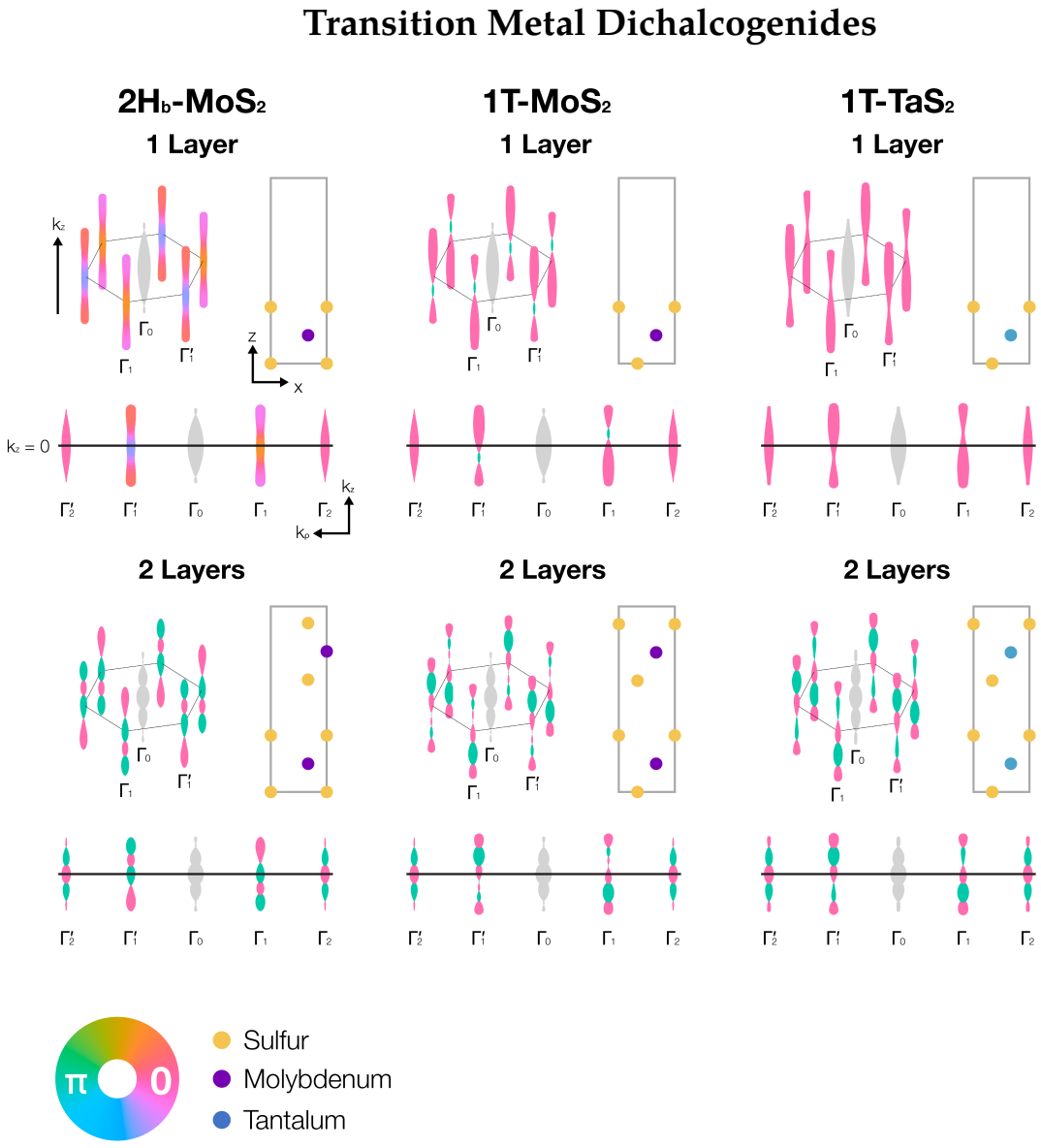

Figure VI.3: 3D Reciprocal Structure of mono- and bi-layer TMDs. The Bragg rods (Γ_0, Γ_1) are shown in 3D alongside a real-space <100> projection of the crystal stacking order. Below, a sideview of the Bragg rods $(\Gamma_0, \Gamma_1, \Gamma_2)$ quantitatively illustrates the structure in k-space. Bragg rods have thickness and color indicating the complex magnitude and phase respectively.

A.9. Atlas of Γ_1 Tilt-Patterns: Graphenes

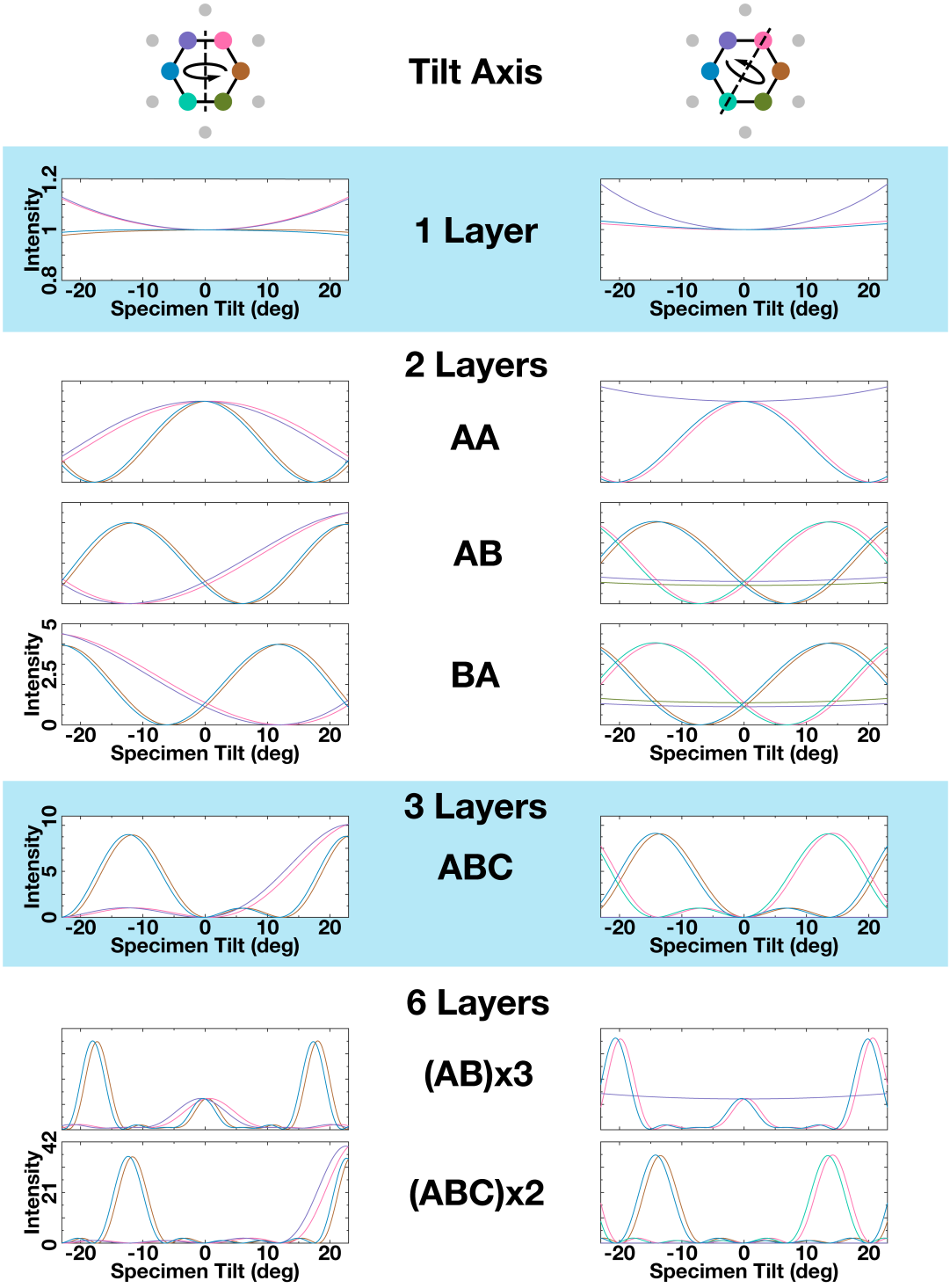

Figure VI.4: Simulated diffraction tilt-pattern of multilayer graphene. The axis of rotation illustrated *top* shows the principle axis that passes through second order Γ_2 (*left column*) and first order Γ_1 (*right column*) Bragg peaks. The tilt patterns are generated for first order peaks only. The small splitting of Friedel pairs in each curve corresponds to a 200 keV electron beam voltage.

A.10. Atlas of Γ_1 Tilt-Patterns: MoS_2

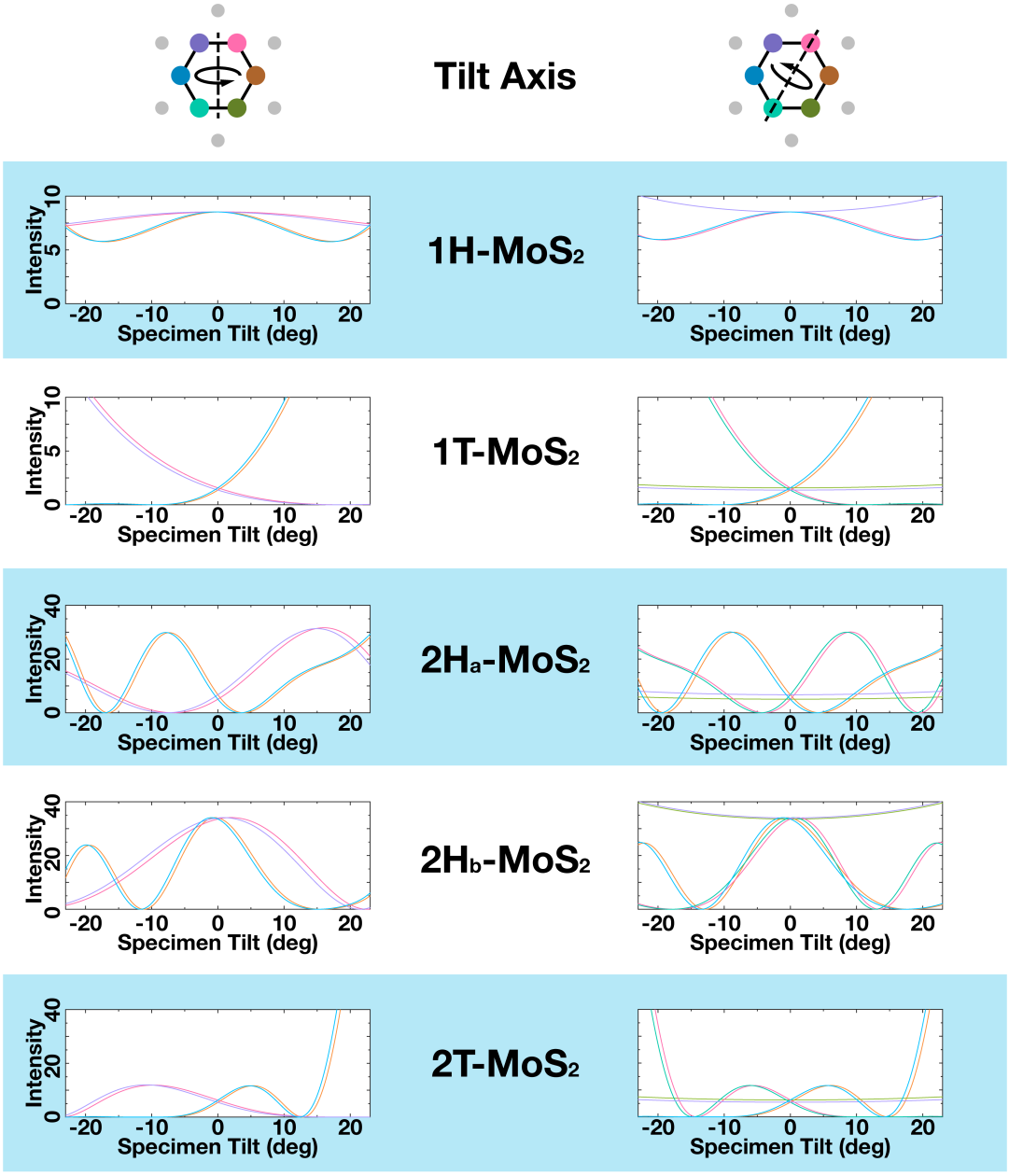

Figure VI.5: Simulated diffraction tilt-patterns of single and bilayer MoS_2 and polytypes thereof. The axis of rotation illustrated *top* shows the principle axis that passes through second order Γ_2 (*left column*) and first order Γ_1 (*right column*) Bragg peaks. The tilt patterns are generated for first order peaks only. The small splitting of Friedel pairs in each curve corresponds to a 200 keV electron beam voltage.

A.11. Atlas of Γ_1 Tilt-Patterns: Transition Metal Dichalcogenides

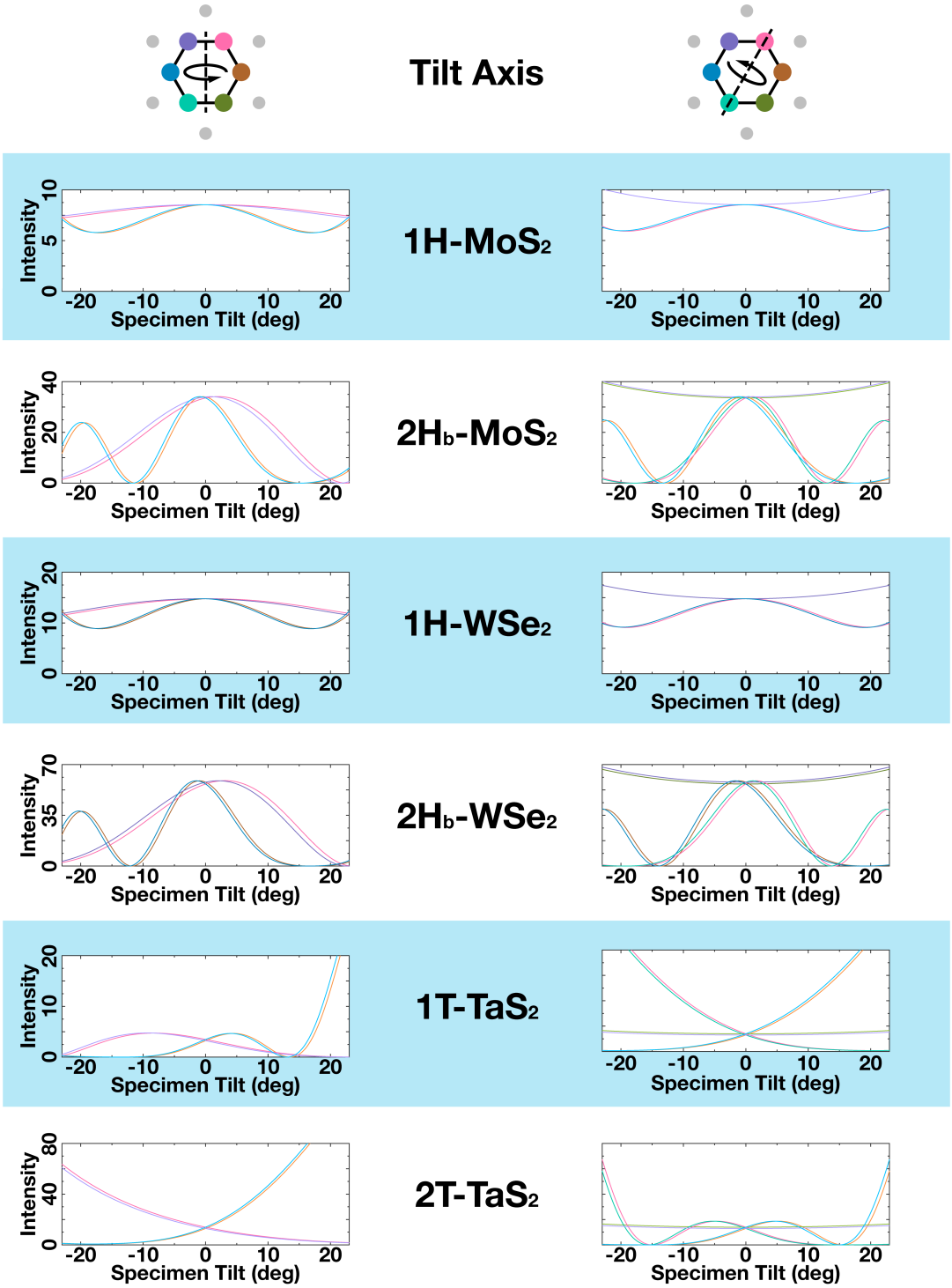

Figure VI.6: Simulated diffraction tilt-patterns of various MoS_2, WSe_2, TaS_2 and polytypes thereof. The axis of rotation illustrated *top* shows the principle axis that passes through second order Γ_2 (*left column*) and first order Γ_1 (*right column*) Bragg peaks. The tilt patterns are generated for first order peaks only. The small splitting of Friedel pairs in each curve corresponds to a 200 keV electron beam voltage.

Appendix B. Appendix for Chapter III

B.1. Definitions: Twisted Bilayer Graphene and its torsional PLD

Here, we define the real and reciprocal lattice constants (a; $b = \frac{4\pi}{a\sqrt{3}}$) and vectors for unrelaxed twisted bilayer graphene with twist angle θ. The real and reciprocal lattice vectors of constituent layers are defined:

Top Layer	Bottom Layer
$\mathbf{a}_1^t = a\big(\cos(-\frac{\theta}{2})\hat{\mathbf{x}} + \sin(-\frac{\theta}{2})\hat{\mathbf{y}}\big)$	$\mathbf{a}_1^b = a\big(\cos(\frac{\theta}{2})\hat{\mathbf{x}} + \sin(\frac{\theta}{2})\hat{\mathbf{y}}\big)$
$\mathbf{a}_2^t = a\big(\cos(\frac{2\pi}{3} - \frac{\theta}{2})\hat{\mathbf{x}} + \sin(\frac{2\pi}{3} - \frac{\theta}{2})\hat{\mathbf{y}}\big)$	$\mathbf{a}_2^b = a\big(\cos(\frac{2\pi}{3} + \frac{\theta}{2})\hat{\mathbf{x}} + \sin(\frac{2\pi}{3} + \frac{\theta}{2})\hat{\mathbf{y}}\big)$
$\mathbf{b}_1^t = b\big(\cos(\frac{\pi}{6} - \frac{\theta}{2})\hat{\mathbf{x}} + \sin(\frac{\pi}{6} - \frac{\theta}{2})\hat{\mathbf{y}}\big)$	$\mathbf{b}_1^b = b\big(\cos(\frac{\pi}{6} + \frac{\theta}{2})\hat{\mathbf{x}} + \sin(\frac{\pi}{6} + \frac{\theta}{2})\hat{\mathbf{y}}\big)$
$\mathbf{b}_2^t = b\big(\cos(\frac{\pi}{2} - \frac{\theta}{2})\hat{\mathbf{x}} + \sin(\frac{\pi}{2} - \frac{\theta}{2})\hat{\mathbf{y}}\big)$	$\mathbf{b}_2^b = b\big(\cos(\frac{\pi}{2} + \frac{\theta}{2})\hat{\mathbf{x}} + \sin(\frac{\pi}{2} + \frac{\theta}{2})\hat{\mathbf{y}}\big)$

Two layers stacked at an angle θ form a moiré pattern with greater periodicity in real space. The real and reciprocal lattice constants (a_m, q) of the moiré supercell are defined:

$$a_m = \kappa a; \quad q = \frac{4\pi}{a_m\sqrt{3}} = \frac{b}{\kappa} \tag{B.1}$$
$$\kappa = \big(2\sin(\frac{\theta}{2})\big)^{-1}$$

κ is a geometrically defined scaling factor of the moiré lattice constant with respect to the crystal lattice constant. The corresponding real and reciprocal lattice vectors of the moiré ($\mathbf{a}_m$, $\mathbf{q}$) are defined to be:

Real Space	Reciprocal Space
$\mathbf{a}_{m1} = a_m\big(\cos(\frac{\pi}{2})\hat{\mathbf{x}} + \sin(\frac{\pi}{2})\hat{\mathbf{y}}\big)$	$\mathbf{b}_{m1} = q\big(\cos(\frac{2\pi}{3})\hat{\mathbf{x}} + \sin(\frac{2\pi}{3})\hat{\mathbf{y}}\big)$
$\mathbf{a}_{m2} = a_m\big(\cos(\frac{7\pi}{6})\hat{\mathbf{x}} + \sin(\frac{7\pi}{6})\hat{\mathbf{y}}\big)$	$\mathbf{b}_{m2} = q\big(\cos(\pi)\hat{\mathbf{x}} + \sin(\pi)\hat{\mathbf{y}}\big)$

The complete torsional PLD field (Δ_{N}) is a sum over each n-th harmonic of the torsional PLD (Δ_n) up to a total of N harmonics. Larger number (N) of Fourier harmonics

is needed to accurately depict sharp boundaries at low twist angles.

$$\Delta_N = \sum_n^N \Delta_n \tag{B.2}$$

$$\Delta_n = \mathrm{A}_n\big(\hat{\mathbf{A}}_{100}\sin\left(n\mathbf{q}_{100}\cdot\mathbf{r}\right) + \hat{\mathbf{A}}_{010}\sin\left(n\mathbf{q}_{010}\cdot\mathbf{r}\right) + \hat{\mathbf{A}}_{001}\sin\left(n\mathbf{q}_{001}\cdot\mathbf{r}\right)\big);\ \hat{\mathbf{A}}\perp\mathbf{q} \tag{B.3}$$

Each harmonic Δ_n is a linear superposition of three PLD waves, with the order of harmonic (n) dictating the wave amplitude ($A_n = A_1 e^{-\kappa n}$) and frequency. From the symmetry of real space distortion, We define one of the PLD wave vectors ($\mathbf{q}_{010}$) to be the moiré reciprocal vector $\mathbf{b}_{m2}$ and define $\mathbf{q}_{100}$ and $\mathbf{q}_{001}$ to be $\pm 120°$ away from $\mathbf{q}_{010}$. In addition, for transverse waves in a torsional PLD, displacement vectors ($\hat{\mathbf{A}}$) are defined to be perpendicular to ($\mathbf{q}$):

$\mathbf{q}_{100} = q\big(\frac{1}{2}\hat{\mathbf{x}} + \frac{\sqrt{3}}{2}\hat{\mathbf{y}}\big)$	$\hat{\mathbf{A}}_{100} = -\frac{\sqrt{3}}{2}\hat{\mathbf{x}} + \frac{1}{2}\hat{\mathbf{y}}$
$\mathbf{q}_{010} = -q\hat{\mathbf{x}}$	$\hat{\mathbf{A}}_{010} = -\hat{\mathbf{y}}$
$\mathbf{q}_{001} = q\big(\frac{1}{2}\hat{\mathbf{x}} - \frac{\sqrt{3}}{2}\hat{\mathbf{y}}\big)$	$\hat{\mathbf{A}}_{001} = \frac{\sqrt{3}}{2}\hat{\mathbf{x}} + \frac{1}{2}\hat{\mathbf{y}}$

Using the definitions above, Δ_n can be expanded:

$$\begin{aligned}\Delta_n = \quad & \hat{\mathbf{x}}\big[-\frac{A_n\sqrt{3}}{2}(\sin\left(n\mathbf{q}_{100}\cdot\mathbf{r}\right) - \sin\left(n\mathbf{q}_{001}\cdot\mathbf{r}\right))\big] \\ & + \hat{\mathbf{y}}\big[\frac{A_n}{2}(\sin\left(n\mathbf{q}_{100}\cdot\mathbf{r}\right) + \sin\left(n\mathbf{q}_{001}\cdot\mathbf{r}\right) - 2\sin\left(n\mathbf{q}_{010}\cdot\mathbf{r}\right))\big]\end{aligned} \tag{B.4}$$

For later conveniences, partial derivatives are calculated :

$$\begin{aligned}
\tfrac{\partial\Delta_{n,x}}{\partial x} &= -\tfrac{nqA_n\sqrt{3}}{4}(\cos\left(n\mathbf{q}_{100}\cdot\mathbf{r}\right) - \cos\left(n\mathbf{q}_{001}\cdot\mathbf{r}\right)) \\
\tfrac{\partial\Delta_{n,y}}{\partial y} &= \tfrac{nqA_n\sqrt{3}}{4}(\cos\left(n\mathbf{q}_{100}\cdot\mathbf{r}\right) - \cos\left(n\mathbf{q}_{001}\cdot\mathbf{r}\right)) = -\tfrac{\partial\Delta_{n,x}}{\partial x} \\
\tfrac{\partial\Delta_{n,x}}{\partial y} &= -\tfrac{3nqA_n}{4}(\cos\left(n\mathbf{q}_{100}\cdot\mathbf{r}\right) + \cos\left(n\mathbf{q}_{001}\cdot\mathbf{r}\right)) \\
\tfrac{\partial\Delta_{n,y}}{\partial x} &= \tfrac{nqA_n}{4}(\cos\left(n\mathbf{q}_{100}\cdot\mathbf{r}\right) + \cos\left(n\mathbf{q}_{001}\cdot\mathbf{r}\right) + 4\cos\left(n\mathbf{q}_{010}\cdot\mathbf{r}\right))
\end{aligned}$$

B.2. Derivation: Local Rotation of Torsional PLD

To understand the resulting distortion of a displacement field ($\mathbf{u}$), we calculate the tensor gradient ($\nabla\mathbf{u}$) to obtain the local strain ($\underline{\epsilon}$) and rotation ($\underline{\underline{\omega}}$) tensors. We ignore out-of-

plane strain and stress for this model.

$$\nabla \mathbf{u} = \begin{bmatrix} \frac{\partial u_x}{\partial x} & \frac{\partial u_x}{\partial y} \\ \frac{\partial u_y}{\partial x} & \frac{\partial u_y}{\partial y} \end{bmatrix} = \underline{\underline{\epsilon}} + \underline{\underline{\omega}} \tag{B.5}$$

where,

$$\underline{\underline{\epsilon}} = \begin{bmatrix} \frac{\partial u_x}{\partial x} & \frac{1}{2}(\frac{\partial u_x}{\partial y} + \frac{\partial u_y}{\partial x}) \\ \frac{1}{2}(\frac{\partial u_x}{\partial y} + \frac{\partial u_y}{\partial x}) & \frac{\partial u_y}{\partial y} \end{bmatrix} \tag{B.6}$$

$$\underline{\underline{\omega}} = \begin{bmatrix} 0 & -\frac{1}{2}(\frac{\partial u_y}{\partial x} - \frac{\partial u_x}{\partial y}) \\ \frac{1}{2}(\frac{\partial u_y}{\partial x} - \frac{\partial u_x}{\partial y}) & 0 \end{bmatrix} \tag{B.7}$$

Here, we focus on $\underline{\underline{\omega}}$—also known as the infinitesimal rotational tensor—that describes local rotation due to the displacement field $\mathbf{u}$. We define the non-zero off-diagonal component of $\underline{\underline{\omega}}$ as rotational field Ω that characterizes the local twist due to $\mathbf{u}$. Notably, Ω is proportional to the curl of displacement field $(\nabla \times \mathbf{u})$.

$$\underline{\underline{\omega}} = \begin{bmatrix} 0 & -\Omega \\ \Omega & 0 \end{bmatrix} = \begin{bmatrix} 0 & -\frac{1}{2}(\frac{\partial u_y}{\partial x} - \frac{\partial u_x}{\partial y}) \\ \frac{1}{2}(\frac{\partial u_y}{\partial x} - \frac{\partial u_x}{\partial y}) & 0 \end{bmatrix} \tag{B.8}$$

From the definitions above, the rotational field due to Torsional PLD of n^{th} harmonic (Ω_n) is :

$$\begin{aligned} \Omega_n &= \frac{1}{2}(\frac{\partial \Delta_{n,y}}{\partial x} - \frac{\partial \Delta_{n,x}}{\partial y}) \\ &= \frac{nqA_n}{8}\Big(3(\cos(n\mathbf{q}_{100}\cdot\mathbf{r}) + \cos(n\mathbf{q}_{001}\cdot\mathbf{r})) \\ &\qquad + (\cos(n\mathbf{q}_{100}\cdot\mathbf{r}) + 4\cos(n\mathbf{q}_{010}\cdot\mathbf{r}) + \cos(n\mathbf{q}_{001}\cdot\mathbf{r}))\Big) \\ &= \frac{nqA_n}{2}\Big(\cos(n\mathbf{q}_{100}\cdot\mathbf{r}) + \cos(n\mathbf{q}_{010}\cdot\mathbf{r}) + \cos(n\mathbf{q}_{001}\cdot\mathbf{r})\Big) \end{aligned} \tag{B.9}$$

The local rotation at AA and AB core, $\mathbf{r}_{AA} = 0$ and $\mathbf{r}_{AB} = \frac{a_m}{\sqrt{3}}\hat{\mathbf{x}}$, are:

$$\Omega_n(\mathbf{r}_{AA}) = \frac{3nqA_n}{2}, \qquad \Omega_n(\mathbf{r}_{AB}) = \begin{cases} \frac{3nqA_n}{2} & n/3 \in \mathbb{Z} \\ -\frac{3nqA_n}{4} & else \end{cases} \tag{B.10}$$

Therefore, rotation in AA core is twice stronger than and opposite to that of AB core for

the fundamental frequency (A_1).

The total rotational field due to the PLD is trivially ($\Omega_{\mathrm{N}} = \sum_n^N \Omega_n$), as differentiation and summation commutes. Figure XXX depicts Ω_{N} for N=1, 3, and 7 with $A_n = A_1 e^{-\kappa n}$.

B.3. Geometric Upper Bound for PLD Amplitude ($\mathbf{A_1}$)

We are interested in the PLD field near a AB core that is dominated by the fundamental PLD harmonic (n=1). The local rotation there is:

$$\Omega_1(\mathbf{r}_{AB}) = -\frac{3qA_1}{4} \tag{B.11}$$

For torsional PLD in each layer to locally restore AB cores, torsional PLD needs to locally twist the AB cores by $\frac{\theta}{2}$:

$$\begin{aligned} -\frac{3qA_1}{4} &= \frac{\theta}{2} \\ \mathrm{A}_1 &= -\frac{4\theta}{6q}; \quad q = \frac{4\pi}{a\sqrt{3}}(2\sin(\frac{\theta}{2})) \approx \frac{4\pi\theta}{a\sqrt{3}} \\ \mathrm{A}_1 &= -\frac{a}{2\pi\sqrt{3}} \end{aligned} \tag{B.12}$$

This defines the upper bound for torsional PLD amplitude. Notably, the upper bound is twist angle independent. For graphene ($a = 2.46$Å), $\mathrm{A}_1 = 22.6$ pm is the upper bound.

B.4. Derivation: Stress, Strain and Elastic Energy of Torsional PLD

To calculate the strain tensor, ($\underline{\underline{\epsilon}}$), we first consider a strain tensor from the n^{th} harmonic of torsional PLD ($\underline{\underline{\epsilon_n}}$).

$$\underline{\underline{\epsilon_n}} = \begin{bmatrix} \epsilon_{n,xx} & \epsilon_{n,xy} \\ \epsilon_{nxy} & \epsilon_{n,yy} \end{bmatrix} = \begin{bmatrix} \frac{\partial \Delta_{n,x}}{\partial x} & \frac{1}{2}(\frac{\partial \Delta_{n,x}}{\partial y} + \frac{\partial \Delta_{n,y}}{\partial x}) \\ \frac{1}{2}(\frac{\partial \Delta_{n,x}}{\partial y} + \frac{\partial \Delta_{n,y}}{\partial x}) & \frac{\partial \Delta_{n,y}}{\partial y} \end{bmatrix} \tag{B.13}$$

.

$$\epsilon_{n,xx} = \frac{\partial \Delta_{n,x}}{\partial x} = -\frac{nqA_n\sqrt{3}}{4}(\cos(n\mathbf{q}_{100}\cdot\mathbf{r}) - \cos(n\mathbf{q}_{001}\cdot\mathbf{r})) \tag{B.14}$$

$$\epsilon_{n,yy} = \frac{\partial \Delta_{n,y}}{\partial y} = -\epsilon_{xx} \tag{B.15}$$

$$\begin{aligned} \epsilon_{n,xy} &= \frac{1}{2}(\frac{\partial \Delta_{n,x}}{\partial y} + \frac{\partial \Delta_{n,y}}{\partial x}) \\ &= -\frac{nqA_n}{4}(\cos(n\mathbf{q}_{100}\cdot\mathbf{r}) + \cos(n\mathbf{q}_{001}\cdot\mathbf{r}) - 2\cos(n\mathbf{q}_{010}\cdot\mathbf{r})) \end{aligned} \tag{B.16}$$

Total strain is

$$\underline{\underline{\epsilon}} = \sum_n^N \underline{\underline{\epsilon_n}}; \qquad \epsilon_{ij} = \sum_n^N \epsilon_{n,ij} \tag{B.17}$$

B.5. Stiffness Tensor, Stress and Elastic Energy

As the torsional PLD here deals with in-plane distortions, and graphene is an isotopic material, we assume plane stress deformation with the stress-strain relationship as follows:

$$\begin{aligned} \begin{pmatrix} \sigma_{xx} \\ \sigma_{yy} \\ \sigma_{xy} \end{pmatrix} &= \frac{E}{1-\nu^2}\begin{bmatrix} 1 & \nu & 0 \\ \nu & 1 & 0 \\ 0 & 0 & \frac{1-\nu}{2} \end{bmatrix}\begin{pmatrix} \epsilon_{xx} \\ \epsilon_{yy} \\ 2\epsilon_{xy} \end{pmatrix} \\ &= \frac{2G}{1-\nu}\begin{bmatrix} 1 & \nu & 0 \\ \nu & 1 & 0 \\ 0 & 0 & \frac{1-\nu}{2} \end{bmatrix}\begin{pmatrix} \epsilon_{xx} \\ \epsilon_{yy} \\ 2\epsilon_{xy} \end{pmatrix} \\ &= \begin{pmatrix} \frac{2G}{1-\nu}(\epsilon_{xx} + \nu\epsilon_{yy}) \\ \frac{2G}{1-\nu}(\nu\epsilon_{xx} + \epsilon_{yy}) \\ 2G\epsilon_{xy} \end{pmatrix} \end{aligned} \tag{B.18}$$

E, G, ν are Young's modulus, Shear modulus and Poisson ratio respectively. We used the usual $E = 2G(1+\nu)$ relationship. The local elastic energy (v_{El}), assuming Hookean elasticity, is defined as:

$$\begin{aligned} v_{El} &= \frac{1}{2}\sigma_{xx}\epsilon_{xx} + \frac{1}{2}\sigma_{yy}\epsilon_{yy} + \sigma_{xy}\epsilon_{xy} \\ &= \frac{G}{1-\nu}(\epsilon_{xx}^2 + \epsilon_{yy}^2 + 2\nu\epsilon_{xx}\epsilon_{yy}) + 2G\epsilon_{xy}^2 \\ &= \frac{G}{1-\nu}((\epsilon_{xx}+\epsilon_{yy})^2 - 2(1-\nu)\epsilon_{xx}\epsilon_{yy}) + 2G\epsilon_{xy}^2 \\ &= \frac{G}{1-\nu}(\epsilon_{xx}+\epsilon_{yy})^2 + 2G(\epsilon_{xy}^2 - \epsilon_{xx}\epsilon_{yy}) \\ &= 2G(\epsilon_{xx}^2 + \epsilon_{xy}^2) \qquad \because \epsilon_{xx} = -\epsilon_{yy} \text{ for Torsional PLD} \end{aligned} \tag{B.19}$$

B.6. Elastic Energy per Unit Cell

The elastic energy term (v_{El}) is related to the spatial derivatives of torsional PLD field ($\frac{\partial \Delta_{n,i}}{\partial i}$) and describes the infinitesimal elastic energy at particular lattice positions. To obtain the elastic energy per moiré unit cell (V_{El}), we integrate v_{El} over the spatial dimensions of a moiré unit cell, μ.

$$\begin{aligned} V_{El} &= \iint_\mu dydx\ v_{El} = 2G\iint_\mu dydx\ (\epsilon_{xx}^2 + \epsilon_{xy}^2) \\ &= 2G\iint_\mu dydx\ [(\sum_n^N \epsilon_{n,xx})^2 + (\sum_n^N \epsilon_{n,xy})^2] \\ &= 2G\sum_n^N \iint_\mu dydx\ \left[(\epsilon_{n,xx}^2 + \epsilon_{n,xy}^2)\right] + 2G\sum_n^N\sum_{m\neq n}^N \iint_\mu dydx\ \left[(\epsilon_{n,xx}\epsilon_{m,xx} + \epsilon_{n,xy}\epsilon_{m,xy})\right] \end{aligned} \tag{B.20}$$

Substituting values from equation (14) – (16):

$$\begin{aligned} &\iint_\mu dydx\ (\epsilon_{n,xx}^2 + \epsilon_{n,xy}^2) \\ &\qquad = \frac{3n^2q^2A_n^2}{4}\iint_\mu dydx\ \left[\cos^2(n\mathbf{q}_{010}\cdot\mathbf{r}) + \cos(n\mathbf{q}_{100}\cdot\mathbf{r})\cos(n\mathbf{q}_{001}\cdot\mathbf{r})\right] \\ &\qquad = \frac{3n^2q^2A_n^2}{4}\int_0^{a_m} dy \int_0^{\frac{a_m\sqrt{3}}{2}} dx\ \left[\cos^2(nqx) + \frac{1}{2}(\cos(nqx)\cos(nq\sqrt{3}y))\right] \\ &\qquad = \frac{3n^2q^2A_n^2}{4n^2q^2\sqrt{3}}(4\pi n)(\pi n) = \sqrt{3}n^2\pi^2A_n^2 \end{aligned} \tag{B.21}$$

$$(\epsilon_{n,xx}\epsilon_{m,xx} + \epsilon_{n,xy}\epsilon_{m,xy}) = \frac{3nmq^2A_n^2}{8}\ \big[2\cos(n\mathbf{q}_{010}\cdot\mathbf{r})\cos(m\mathbf{q}_{010}\cdot\mathbf{r}) - \cos(n\mathbf{q}_{010}\cdot\mathbf{r})(\cos(m\mathbf{q}_{100}\cdot\mathbf{r}) + \cos(m\mathbf{q}_{001}\cdot\mathbf{r}))\big] \tag{B.22}$$

$$\iint_{\mu} dydx\ \cos(n\mathbf{q}_{010}\cdot\mathbf{r})\cos(m\mathbf{q}_{010}\cdot\mathbf{r}) = 0 \because \text{Orthogonality} \tag{B.23}$$

$$\iint_{\mu} dydx\ \cos(n\mathbf{q}_{010}\cdot\mathbf{r})(\cos(m\mathbf{q}_{100}\cdot\mathbf{r}) + \cos(m\mathbf{q}_{001}\cdot\mathbf{r})) \tag{B.24}$$

$$= \int_0^{a_m} dy \int_0^{\frac{a_m\sqrt{3}}{2}} dx\ 2\cos(nqx)\cos(\frac{mq}{2}x)\cos(\frac{mq\sqrt{3}}{2}y))$$

$$v = \frac{mq\sqrt{3}y}{2}$$

$$= \int_0^{a_m} dy\ 2\cos(nqx)\cos(\frac{mq}{2}x)\int_0^{2\pi m} dv\cos(v)) = 0$$

Therefore, all cross-terms are zero:

$$\iint_{\mu} dydx\ \left[(\epsilon_{n,xx}\epsilon_{m,xx} + \epsilon_{n,xy}\epsilon_{m,xy})\right] = 0 \tag{B.25}$$

Finally, we calculate the total elastic energy per moirè unit cell in each layer by summing over contributions from a total of N harmonics:

$$V_{El} = 2\sqrt{3}\pi^2 G\sum_{n}^{N} n^2A_n^2 \tag{B.26}$$

As defined previously, $A_n = A_1e^{-\kappa n}$. Elastic energy cost of n^{th} harmonic torsional PLD is independent of other harmonics.

Appendix C. Appendix for Chapter IV

C.1. Modelling the CDW twinning across the C⇋IC transition

In general, a CDW is characterized by two intertwined ingredients: (1) the amplitude/phase of the CDW order parameter and (2) the length/orientation of the CDW wavevector. The significant role of the first ingredient has been extensively studied in literature [1–4]. For this study, we focus on the wavevector orientation (θ) and its fluctuation as a minimum model to characterize the competition between the two mirror twins observed in the experiments. This approximation correctly captures qualitative features away from the IC-C CDW transition. Near the phase transition, where additional fluctuations are no longer negligible, a more sophisticated model becomes needed.

We approximate the free energy landscape using Landau expansion:

$$f_i(T) = a_2(T - T_c)\theta_i^2 + \mathrm{a}_4\theta_i^4 + \sum_{nn}^{6} \cos(\theta_{nn} - \theta_i)^2 \tag{C.1}$$

with f, T, T_c, a, θ denotes local free energy, temperature, transition temperature, Landau energy coefficient, and local CDW orientation respectively. The last term is an XY nearest-neighbor interaction that enforces smoothness; in the continuum limit, it converges to $|\nabla\theta|^2$. We chose 6 nearest-neighbors to accommodate the crystal symmetry (Fig. IV.4c). The simulation was done on hexagonal grid with 65536 sites and periodic boundary condition.

The distribution of θ was calculated using Markov Chain Monte Carlo simulation with Metropolis-Hastings algorithm. Initially, a random distribution θ was generated. At each iteration, 40% of sites were randomly selected, then randomly generated θ were accepted or rejected based on Boltzmann statistics: $\exp[-\Delta f/k_BT]$. The effect of cooling was simulated in simulated annealing manner where initial T was set to $2\,T_c$ then reduced by $0.2\,T_c$ every 10^{10} iterations (See Supplemental Figure S9 for simulation parameters).

To simulate far-field diffraction from simulated θ, each lattice position ($\mathbf{r}_i$) was distorted with three longitudinal modulation waves with wave vector $\mathbf{q}_{i,1}, \mathbf{q}_{i,2}, \mathbf{q}_{i,3}$ along θ_i,

$\theta_i + 120°$, $\theta_i + 240°$: $\mathbf{r}'_i = \mathbf{r}_i + \sum_{n=1,2,3} \mathbf{A}_n \sin(\mathbf{q}_{i,n} \cdot \mathbf{r}_i)$. Far-field diffraction ($I(\mathbf{k})$) was calculated by taking modulus squared of plane waves from each lattice sites: $I(\mathbf{k}) = |\sum_i \exp[i\mathbf{k} \cdot \mathbf{r}'_i]|^2$.

Appendix D. On Infinite Series of Bessel functions of the First Kind: $\sum_\nu J_{N\nu+p}(x), \sum_\nu (-1)^\nu J_{N\nu+p}(x)$

D.1. Introduction

Infinite series of Bessel functions of the first kind in the form $\sum_{2\nu} J_{2\nu}(x)$ and $\sum_{3\nu} J_{3\nu}(x)$ arise in many natural systems. They are of particular interest in condensed matter physics when crystals spontaneously break symmetry [5] due to correlated electron effects such as superconductivity, charge density waves, colossal magnetoresistance, and quantum spin liquids. Mathematically, these series can appear when sinusoids exist inside complex exponentials—as described by the Jacobi-Anger relation [6, 7]. Early treatises on Bessel functions by Neumann and Watson [8–10] provide analytic solutions to the alternating series $\sum_\nu (-1)^\nu J_{2\nu}(x)$ and $\sum_\nu (-1)^\nu J_{2\nu+1}(x)$ which are commonly tabulated [11–13]. However analytic expressions for $\sum_\nu J_{3\nu}(x)$, $\sum_\nu J_{3\nu\pm1}(x)$ or more general series $\sum_\nu J_{N\nu+p}(x)$ and $\sum_\nu (-1)^\nu J_{N\nu+p}(x)$ are not readily available. We show closed form expressions to infinite series of Bessel functions of the first kind exist. The expression is evaluated by engineering a Dirac comb that selects specific sequences within the Bessel series.

To illustrate, we find a closed form expression to the series:

$$\sum_{\nu=-\infty}^{\infty} J_{3\nu+p}(x) = \frac{1}{3}\left[1 + 2\cos\left(\frac{x\sqrt{3}}{2} - \frac{2\pi p}{3}\right)\right]$$

$$\nu, p \in \mathbb{Z};\ x \in \mathbb{C}$$

More generally, we find an expression to all series in the class:

$$\sum_{\nu=-\infty}^{\infty} J_{N\nu+p}(x) = \frac{1}{N}\sum_{q=0}^{N-1} e^{ix\sin(2\pi q/N)} e^{-i2\pi pq/N}$$

$$\sum_{\nu=-\infty}^{\infty} (-1)^\nu J_{N\nu+p}(x) = \frac{1}{N}\sum_{q=0}^{N-1} e^{ix\sin((2q+1)\pi/N)} e^{-i(2q+1)\pi p/N}$$

$$\nu, p, q \in \mathbb{Z};\ N \in \mathbb{Z}^+;\ x \in \mathbb{C}$$

From these theorem's, we tabulate a family of closed analytic forms to infinite series of Bessel functions of the first kind.

D.2. Evaluation of Series: $\sum_{\nu=-\infty}^{\infty} J_{N\nu+p}(x)$

Theorem 1. *Infinite series of Bessel functions of the first kind of the form* $\sum_{\nu}^{\pm\infty} J_{N\nu+p}(x)$ *where* $\nu, p, q \in \mathbb{Z},\ N \in \mathbb{Z}^+$ *and* $x \in \mathbb{C}$ *have following closed expression:*

$$\sum_{\nu=-\infty}^{\infty} J_{N\nu+p}(x) = \frac{1}{N} \sum_{q=0}^{N-1} e^{-i2\pi pq/N} e^{ix\sin(2\pi q/N)} \tag{D.1}$$

Proof. Consider the following series of evenly spaced delta functions (i.e. a Dirac comb) on an infinite series of Bessel functions:

$$f(k) = \sum_{h=-\infty}^{\infty} \sum_{p=0}^{N-1} \delta(k - (h + \frac{p}{N})a) \sum_{\nu=-\infty}^{\infty} J_{N\nu+p}(kA) \tag{D.2}$$

where $\nu, h, p \in \mathbb{Z}$; $N \in \mathbb{Z}^+$; $k, a \in \mathbb{R}$; $A \in \mathbb{C}$.

Three summations are re-grouped into two:

$$f(k) = \sum_{h=-\infty}^{\infty} \sum_{\alpha=-\infty}^{\infty} \delta(k - (h + \frac{\alpha}{N})a) J_{\alpha}(kA) \tag{D.3}$$

The Dirac comb can be represented as a Fourier series:

$$\sum_{h=-\infty}^{\infty} \delta(k - ha) = \frac{1}{a} \sum_{m=-\infty}^{\infty} e^{-i2\pi km/a} \tag{D.4}$$

Note, this formal identity maybe truncated to a finite summation to guarantee convergence, wherein a finite series of sinusoidal harmonics is equal to finite width Dirichlet kernels that approaches a Dirac comb.

With (D.4), $f(k)$ becomes:

$$f(k) = \frac{1}{a} \sum_{m=-\infty}^{\infty} e^{-i2\pi km/a} \sum_{\alpha=-\infty}^{\infty} J_{\alpha}(kA) e^{i\alpha 2\pi m/N} \tag{D.5}$$

The summation over α appears in the Jacobi-Anger relation [6, 7, 10]:

$$e^{ix\sin(\theta)} = \sum_{\alpha=-\infty}^{\infty} J_\alpha(x) e^{i\alpha\theta} \tag{D.6}$$

Using the Jacobi-Anger relation:

$$f(k) = \frac{1}{a} \sum_{m=-\infty}^{\infty} e^{-i2\pi km/a} e^{ikA\sin(2\pi m/N)} \tag{D.7}$$

We split the summation over m into $m = ..., Nn, Nn+1, ..., Nn+(N-1), ...$:

$$\begin{aligned} f(k) = \frac{1}{a} \sum_{n=-\infty}^{\infty} \Big[&... + e^{-i2\pi knN/a} \\ &+ e^{-i2\pi knN/a} e^{-i2\pi k/a} e^{ikA\sin(2\pi/N)} + ... \\ &+ e^{-i2\pi knN/a} e^{-i2\pi k(N-1)/a} e^{ikA\sin(2\pi(N-1)/N)} + ... \Big] \\ = \frac{1}{a} \sum_{n=-\infty}^{\infty} e^{-i2\pi knN/a} &\sum_{q=1}^{N-1} e^{-i2\pi kq/a} e^{ikA\sin(2\pi q/N)} \end{aligned} \tag{D.8}$$

Using (D.4) again:

$$f(k) = \frac{1}{N} \sum_{l=-\infty}^{\infty} \delta(k - \frac{la}{N}) \sum_{q=0}^{1-N} e^{ikA\sin(2\pi q/N)} e^{-i2\pi kq/a} \tag{D.9}$$

Substitute $k = \frac{la}{N}; l \in \mathbb{Z}$, as f is non-zero only where a delta function exists.

$$f(k) = \frac{1}{N} \sum_{l=-\infty}^{\infty} \delta(k - \frac{la}{N}) \sum_{q=0}^{N-1} e^{ikA\sin(2\pi q/N)} e^{-i2\pi ql/N} \tag{D.10}$$

We split the summation into $l = ..., Nh, Nh+1, ..., (N+1)h-1...$ then regroup, similar with (D.8):

$$f(k) = \frac{1}{N} \sum_{h=-\infty}^{\infty} \sum_{p=0}^{N-1} \delta(k - (h + \frac{p}{N})a) \sum_{q=0}^{N-1} e^{ikA\sin(2\pi q/N)} e^{-i2\pi pq/N} \tag{D.11}$$

Initial expression (D.2) must equal (D.11):

$$\sum_{h=-\infty}^{\infty}\sum_{p=0}^{N-1}\delta(k-(h+\frac{p}{N})a)\sum_{\nu=-\infty}^{\infty}J_{N\nu+p}(kA)$$
$$=\frac{1}{N}\sum_{h=-\infty}^{\infty}\sum_{p=0}^{N-1}\delta(k-(h+\frac{p}{N})a)\sum_{q=0}^{N-1}e^{ikA\sin(2\pi q/N)}e^{-i2\pi pq/N} \tag{D.12}$$

This relation suggests only values on the Dirac comb are equivalent. However, the variable a can take on any real value thus the expression holds for all values of kA. The equivalent Dirac lattices on each side can be disregarded.

$$\therefore \quad \sum_{\nu=-\infty}^{\infty}J_{N\nu+p}(x)=\frac{1}{N}\sum_{q=0}^{N-1}e^{ix\sin(2\pi q/N)}e^{-i2\pi pq/N} \tag{D.13}$$

□

Corollary 1. *From Theorem 1 we comprise a table of closed form expressions:*

N	p	$\sum_{\nu=-\infty}^{\infty} J_{N\nu+p}(x)$	$\frac{1}{N}\sum_{q=0}^{N-1} e^{ix\sin(2\pi q/N)}e^{-i2\pi pq/N}$
1	0	$\sum_{\nu=-\infty}^{\infty} J_{\nu}(x)$	1 [*10, 11, 14*]
2	0	$\sum_{\nu=-\infty}^{\infty} J_{2\nu}(x)$	1 [*10, 11*]
	1	$\sum_{\nu=-\infty}^{\infty} J_{2\nu+1}(x)$	0 [*10, 11*]
3	0	$\sum_{\nu=-\infty}^{\infty} J_{3\nu}$	$\frac{1}{3}\left[1+2\cos(\frac{x\sqrt{3}}{2})\right]$
	1	$\sum_{\nu=-\infty}^{\infty} J_{3\nu+1}$	$\frac{1}{3}\left[1+2\cos(\frac{x\sqrt{3}}{2}-\frac{2\pi}{3})\right]$
	2	$\sum_{\nu=-\infty}^{\infty} J_{3\nu+2}$	$\frac{1}{3}\left[1+2\cos(\frac{x\sqrt{3}}{2}-\frac{4\pi}{3})\right]$
4	0	$\sum_{\nu=-\infty}^{\infty} J_{4\nu}$	$\cos^2(\frac{x}{2})$
	1	$\sum_{\nu=-\infty}^{\infty} J_{4\nu+1}$	$\frac{1}{2}\sin(x)$
	2	$\sum_{\nu=-\infty}^{\infty} J_{4\nu+2}$	$\sin^2(\frac{x}{2})$
	3	$\sum_{\nu=-\infty}^{\infty} J_{4\nu+3}$	$-\frac{1}{2}\sin(x)$
5	0	$\sum_{\nu=-\infty}^{\infty} J_{5\nu}$	$\frac{1}{5}\left[1+2\cos(x\sin(\frac{2\pi}{5}))+2\cos(x\sin(\frac{4\pi}{5}))\right]$
	1	$\sum_{\nu=-\infty}^{\infty} J_{5\nu+1}$	$\frac{1}{5}\left[1+2\cos(x\sin(\frac{2\pi}{5})-\frac{2\pi}{5})+2\cos(x\sin(\frac{4\pi}{5})-\frac{4\pi}{5})\right]$
	2	$\sum_{\nu=-\infty}^{\infty} J_{5\nu+2}$	$\frac{1}{5}\left[1+2\cos(x\sin(\frac{2\pi}{5})-\frac{4\pi}{5})+2\cos(x\sin(\frac{4\pi}{5})-\frac{8\pi}{5})\right]$
	3	$\sum_{\nu=-\infty}^{\infty} J_{5\nu+3}$	$\frac{1}{5}\left[1+2\cos(x\sin(\frac{2\pi}{5})-\frac{6\pi}{5})+2\cos(x\sin(\frac{4\pi}{5})-\frac{12\pi}{5})\right]$
	4	$\sum_{\nu=-\infty}^{\infty} J_{5\nu+4}$	$\frac{1}{5}\left[1+2\cos(x\sin(\frac{2\pi}{5})-\frac{8\pi}{5})+2\cos(x\sin(\frac{4\pi}{5})-\frac{16\pi}{5})\right]$
6	0	$\sum_{\nu=-\infty}^{\infty} J_{6\nu}$	$\frac{1}{3}\left[1+2\cos(\frac{x\sqrt{3}}{2})\right]$
	1	$\sum_{\nu=-\infty}^{\infty} J_{6\nu+1}$	$\frac{1}{\sqrt{3}}\sin(\frac{\sqrt{3}}{2})$
	2	$\sum_{\nu=-\infty}^{\infty} J_{6\nu+2}$	$\frac{1}{3}\left[1-\cos(\frac{x\sqrt{3}}{2})\right]$
	3	$\sum_{\nu=-\infty}^{\infty} J_{6\nu+3}$	0
	4	$\sum_{\nu=-\infty}^{\infty} J_{6\nu+4}$	$\frac{1}{3}\left[1-\cos(\frac{x\sqrt{3}}{2})\right]$
	5	$\sum_{\nu=-\infty}^{\infty} J_{6\nu+5}$	$-\frac{1}{\sqrt{3}}\sin(\frac{\sqrt{3}}{2})$

D.3. Evaluation of Alternating Series: $\sum_{\nu=-\infty}^{\infty}(-1)^{\nu}J_{N\nu+p}(x)$

Theorem 2. *Infinite series of Bessel functions of the first kind of the form* $\sum_{\nu}(-1)^{\nu}J_{N\nu+p}(x)$ *where* $\nu, p, q \in \mathbb{Z},\ N \in \mathbb{Z}^{+}$ *and* $x \in \mathbb{C}$ *have following closed expression:*

$$\sum_{\nu=-\infty}^{\infty}(-1)^{\nu}J_{N\nu+p}(x) = \frac{1}{N}\sum_{q=0}^{N-1}e^{ix\sin(\frac{(2q+1)\pi}{N})}e^{-i\frac{(2q+1)\pi p}{N}} \tag{D.14}$$

Proof. Consider the following Dirac comb on an infinite series of Bessel functions:

$$g(k) = \sum_{h=-\infty}^{\infty}\sum_{p=0}^{N-1}\delta(k-(h+\frac{p}{N})a)\sum_{\nu=-\infty}^{\infty}(-1)^{\nu}J_{N\nu+p}(kA) \tag{D.15}$$

where $\nu, h, p \in \mathbb{Z}$; $N \in \mathbb{Z}^{+}$; $k, a \in \mathbb{R}$; $A \in \mathbb{C}$.

Three summations are re-grouped into two:

$$\begin{aligned} g(k) &= \sum_{h=-\infty}^{\infty}\sum_{\alpha=-\infty}^{\infty}\delta(k-(h+\frac{\alpha}{N})a)(-1)^{h}J_{\alpha}(kA) \\ &= \sum_{h=-\infty}^{\infty}\sum_{\alpha=-\infty}^{\infty}\delta(k-(h+\frac{\alpha}{N})a)e^{-i(k-\frac{\alpha}{N}a)\frac{\pi}{a}}J_{\alpha}(kA) \\ &= \sum_{h=-\infty}^{\infty}\sum_{\alpha=-\infty}^{\infty}\delta(k-(h+\frac{\alpha}{N})a)e^{-i\pi k/a}e^{i\pi\alpha/N}J_{\alpha}(kA) \end{aligned} \tag{D.16}$$

The Dirac comb can be represented as a Fourier series (D.4):

$$\begin{aligned} g(k) &= \frac{1}{a}\sum_{m=-\infty}^{\infty}\sum_{\alpha=-\infty}^{\infty}e^{-i2\pi(k-\frac{\alpha}{N}a)m/a}e^{-i\pi k/a}e^{i\pi\alpha/N}J_{\alpha}(kA) \\ &= \frac{1}{a}\sum_{m=-\infty}^{\infty}e^{-i\pi k(2m+1)/a}\sum_{\alpha=-\infty}^{\infty}e^{i\alpha\pi(2m+1)/N}J_{\alpha}(kA) \end{aligned} \tag{D.17}$$

Using the Jacobi-Anger relation (D.6):

$$g(k) = \frac{1}{a}\sum_{m=-\infty}^{\infty}e^{-i\pi k(2m+1)/a}e^{ikA\sin(\pi(2m+1)/N)} \tag{D.18}$$

We split the summation over m into $m = ..., Nn, Nn+1, ..., Nn+(N-1), ...$:

$$\begin{aligned} g(k) = \frac{1}{N} \sum_{n=-\infty}^{\infty} \Big[&... + e^{-i2\pi knN/a} e^{-i\pi k/a} e^{ikA\sin(\frac{1\pi}{N})} \\ &+ e^{-i2\pi knN/a} e^{-i3\pi k/a} e^{ikA\sin(\frac{3\pi}{N})} + ... \\ &+ e^{-i2\pi knN/a} e^{-i(2N-1)\pi k/a} e^{ikA\sin(\frac{(2N-1)\pi}{N})} + ... \Big] \\ = \frac{1}{a} \sum_{n=-\infty}^{\infty} e^{-i2\pi knN/a} &\sum_{q=0}^{N-1} e^{-i(2q+1)\pi k/a} e^{ikA\sin(\frac{(2q+1)\pi}{N})} \end{aligned} \tag{D.19}$$

Using (D.4) again:

$$g(k) = \frac{1}{N} \sum_{l=-\infty}^{\infty} \delta(k - \frac{a}{N}l) \sum_{q=0}^{N-1} e^{ikA\sin(\frac{(2q+1)\pi}{N})} e^{-i(2q+1)\pi k/a} \tag{D.20}$$

Substitute $k = l\frac{a}{N}$, as f is non-zero where a delta function exists.

$$g(k) = \frac{1}{N} \sum_{l=-\infty}^{\infty} \delta(k - \frac{a}{N}l) \sum_{q=0}^{N-1} e^{ikA\sin(\frac{(2q+1)\pi}{N})} e^{-i\frac{(2q+1)\pi l}{N}} \tag{D.21}$$

We split the summation into $l = ..., Nh, Nh+1, ..., Nh+(N-1), ...$ then regroup:

$$g(k) = \frac{1}{N} \sum_{h=-\infty}^{\infty} \sum_{p=0}^{N-1} \delta(k - (h + \frac{p}{N})a)(-1)^h \sum_{q=0}^{N-1} e^{ikA\sin(\frac{(2q+1)\pi}{N})} e^{-i\frac{(2q+1)\pi p}{N}} \tag{D.22}$$

Initial expression (D.15) must equal (D.22):

$$\begin{aligned} &\sum_{h=-\infty}^{\infty} \sum_{p=0}^{N-1} \delta(k - (h + \frac{p}{N})a) \sum_{\nu=-\infty}^{\infty} (-1)^\nu J_{N\nu+p}(kA) = \\ &\qquad \frac{1}{N} \sum_{h=-\infty}^{\infty} \sum_{p=0}^{N-1} \delta(k - (h + \frac{p}{N})a)(-1)^h \sum_{q=0}^{N-1} e^{ikA\sin(\frac{(2q+1)\pi}{N})} e^{-i\frac{(2q+1)\pi p}{N}} \end{aligned} \tag{D.23}$$

The variable a can take on any real value thus the expression holds for all values of

kA. The equivalent Dirac lattices on each side can be disregarded.

$$\therefore \quad \sum_{\nu=-\infty}^{\infty} (-1)^{\nu} J_{N\nu+p}(x) = \frac{1}{N} \sum_{q=0}^{N-1} e^{ix \sin\left(\frac{(2q+1)\pi}{N}\right)} e^{-i\frac{(2q+1)\pi p}{N}} \tag{D.24}$$

□

Corollary 2. *From Theorem 2 we comprise a table of closed form expressions:*

N	p	$\sum_{\nu=-\infty}^{\infty}(-1)^{\nu}J_{N\nu+p}(x)$	$\frac{1}{N}\sum_{q=0}^{N-1}e^{ix\sin(\frac{(2q+1)\pi}{N})}e^{-i\frac{(2q+1)\pi p}{N}}$	
1	0	$\sum_{\nu=-\infty}^{\infty}(-1)^{\nu}J_{\nu}(x)$	1	[*10, 11*]
2	0	$\sum_{\nu=-\infty}^{\infty}(-1)^{\nu}J_{2\nu}(x)$	$\cos(x)$	[*10*]
	1	$\sum_{\nu=-\infty}^{\infty}(-1)^{\nu}J_{2\nu+1}(x)$	$\sin(x)$	[*10*]
3	0	$\sum_{\nu=-\infty}^{\infty}(-1)^{\nu}J_{3\nu}(x)$	$\frac{1}{3}\left[1+2\cos(\frac{x\sqrt{3}}{2})\right]$	
	1	$\sum_{\nu=-\infty}^{\infty}(-1)^{\nu}J_{3\nu+1}(x)$	$-\frac{1}{3}\left[1-2\cos(\frac{x\sqrt{3}}{2}-\frac{\pi}{3})\right]$	
	2	$\sum_{\nu=-\infty}^{\infty}(-1)^{\nu}J_{3\nu+2}(x)$	$\frac{1}{3}\left[1+2\cos(\frac{x\sqrt{3}}{2}-\frac{2\pi}{3})\right]$	
4	0	$\sum_{\nu=-\infty}^{\infty}(-1)^{\nu}J_{4\nu}(x)$	$\cos(\frac{x}{\sqrt{2}})$	
	1	$\sum_{\nu=-\infty}^{\infty}(-1)^{\nu}J_{4\nu+1}(x)$	$\frac{1}{\sqrt{2}}\sin(\frac{x}{\sqrt{2}})$	
	2	$\sum_{\nu=-\infty}^{\infty}(-1)^{\nu}J_{4\nu+2}(x)$	0	
	3	$\sum_{\nu=-\infty}^{\infty}(-1)^{\nu}J_{4\nu+3}(x)$	$\frac{1}{\sqrt{2}}\sin(\frac{x}{\sqrt{2}})$	
5	0	$\sum_{\nu=-\infty}^{\infty}(-1)^{\nu}J_{5\nu}(x)$	$\frac{1}{5}\left[1+2\cos(x\sin(\frac{\pi}{5}))+2\cos(x\sin(\frac{3\pi}{5}))\right]$	
	1	$\sum_{\nu=-\infty}^{\infty}(-1)^{\nu}J_{5\nu+1}(x)$	$-\frac{1}{5}\left[1+2\cos(x\sin(\frac{\pi}{5})+\frac{4\pi}{5})+2\cos(x\sin(\frac{3\pi}{5})+\frac{2\pi}{5})\right]$	
	2	$\sum_{\nu=-\infty}^{\infty}(-1)^{\nu}J_{5\nu+2}(x)$	$\frac{1}{5}\left[1+2\cos(x\sin(\frac{\pi}{5})+\frac{8\pi}{5})+2\cos(x\sin(\frac{3\pi}{5})+\frac{4\pi}{5})\right]$	
	3	$\sum_{\nu=-\infty}^{\infty}(-1)^{\nu}J_{5\nu+3}(x)$	$-\frac{1}{5}\left[1+2\cos(x\sin(\frac{\pi}{5})+\frac{12\pi}{5})+2\cos(x\sin(\frac{3\pi}{5})+\frac{6\pi}{5})\right]$	
	4	$\sum_{\nu=-\infty}^{\infty}(-1)^{\nu}J_{5\nu+4}(x)$	$\frac{1}{5}\left[1+2\cos(x\sin(\frac{\pi}{5})+\frac{16\pi}{5})+2\cos(x\sin(\frac{3\pi}{5})+\frac{8\pi}{5})\right]$	
6	0	$\sum_{\nu=-\infty}^{\infty}(-1)^{\nu}J_{6\nu}(x)$	$\frac{1}{3}\left[\cos(x)+2\cos(\frac{x}{2})\right]$	
	1	$\sum_{\nu=-\infty}^{\infty}(-1)^{\nu}J_{6\nu+1}(x)$	$\frac{1}{3}\left[\sin(x)+\sin(\frac{x}{2})\right]$	
	2	$\sum_{\nu=-\infty}^{\infty}(-1)^{\nu}J_{6\nu+2}(x)$	$-\frac{1}{3}\left[\cos(x)-\cos(\frac{x}{2})\right]$	
	3	$\sum_{\nu=-\infty}^{\infty}(-1)^{\nu}J_{6\nu+3}(x)$	$-\frac{1}{3}\left[\sin(x)-2\sin(\frac{x}{2})\right]$	
	4	$\sum_{\nu=-\infty}^{\infty}(-1)^{\nu}J_{6\nu+4}(x)$	$\frac{1}{3}\left[\cos(x)-\cos(\frac{x}{2})\right]$	
	5	$\sum_{\nu=-\infty}^{\infty}(-1)^{\nu}J_{6\nu+5}(x)$	$\frac{1}{3}\left[\sin(x)+\sin(\frac{x}{2})\right]$	

In Corollary 1 and 2, we have noted references to previous reported expressions for $N = 1, 2$ that are closely related. For $N = 1$ the expression is given using the generating function $e^{1/2(t-1/t)x} = \sum_{\nu=-\infty}^{\infty} J_\nu(x)t^\nu$ when $t = 1$. For $N = 2$, the expressions can be re-written such that $\sum_{\nu=-\infty}^{\infty}(-1)^\nu J_{2\nu}(x) = J_0(x) + 2\sum_{\nu=1}^{\infty}(-1)^\nu J_{2\nu}(x) = \cos x$ and $\sum_{\nu=-\infty}^{\infty}(-1)^\nu J_{2\nu+1}(x) = \sum_{\nu=0}^{\infty}(-1)^\nu J_{2\nu+1}(x) = \sin x$ using the identity $J_{-\nu}(x) = (-1)^\nu J_\nu(x)$.

References

[1] W. L. McMillan, "Landau theory of charge-density waves in transition-metal dichalcogenides", Phys. Rev. B **12**, 1187–1196 (1975) 10.1103/physrevb.12.1187.

[2] K. Nakanishi and H. Shiba, "Domain-like incommensurate charge-density-wave states and the first-order incommensurate-commensurate transitions in layered tantalum dichalcogenides. i. 1T-polytypes", J. Phys. Soc. Jpn. **43**, 1839–1847 (1977) 10.1143/JPSJ.43.1839.

[3] K. Nakanishi and H. Shiba, "Domain-like incommensurate charge-density-wave states and the first-order incommensurate-commensurate transitions in layered tantalum dichalcogenides. ii. 2h-polytype", J. Phys. Soc. Japan **44**, 1465–1473 (1978) 10.1143/JPSJ.44.1465.

[4] K. Nakatsugawa, S. Tanda, and T. N. Ikeda, "Multivalley free energy landscape and the origin of stripe and quasi-stripe cdw structures in monolayer MX_2 compounds", Sci. Rep. **10**, 1239 (2020) 10.1038/s41598-020-58013-7.

[5] R. E. Peierls, *Surprises in theoretical physics*, Vol. 107 (Princeton University Press, 1979).

[6] C. G. J. Jacobi, "Formula transformationis integralium definitorum", J. fur Reine Angew. Math. **15**, 1–26 (1836) 10.1515/crll.1836.15.1.

[7] C. T. Anger, "Untersuchungen über die function I_k^h mit anwendungen auf das kepler'sche problem", Neueste Schriften Der Naturforschenden Gesellschaft in Danzig **5**, 1–29 (1855).

[8] C. Neumann, *Theorie der bessel'schen functionen : ein analogon zur theorie der kugelfunctionen* (Leipzig Teubner, 1867).

[9] E. T. Whittaker and G. N. Watson, *A course of modern analysis* (Cambridge University Press, 1996).

[10] G. N. Watson, *A treatise on the theory of bessel functions* (Cambridge University Press, 1922).

[11] A. Jeffrey and D. Zwillinger, *Table of integrals, series, and products* (Academic Press, 2007).

[12] M. Abramowitz and I. A. Stegun, *Handbook of mathematical functions with formulas, graphs, and mathematical tables* (National Bureau of Standards, 1964).

[13] A. P. Prudnikov, Y. Brychkov, and O. I. Marichev, *Integrals and series. vol 2. special functions* (Gorden & Breach Science Publishers, 1986).

[14] R. Kuzmin, *Бесселевы функции* (Государственное технико-теоретическое издательство, 1933).